# Final Delivery of Data from the c2d Legacy Project: IRAC and MIPS

Neal J. Evans II, Paul M. Harvey, Michael M. Dunham

*The University of Texas at Austin, Department of Astronomy, 1 University Station C1400, Austin, Texas 78712–0259*

Tracy L. Huard

*Smithsonian Astrophysical Observatory, 60 Garden St. MS42, Cambridge, MA 02138*

Lee G. Mundy, Shih-ping Lai, Nicholas Chapman

*Astronomy Department, University of Maryland, College Park, MD 20742*

T.Y. Brooke, Melissa L. Enoch

*Division of Physics, Mathematics, & Astronomy 105-24, California Institute of Technology, Pasadena CA 91125*

Karl R. Stapelfeldt

*Jet Propulsion Laboratory, MS 183-900, California Institute of Technology, Pasadena, CA 91109*

## ABSTRACT

This report documents the fourth and final delivery of IRAC and MIPS data by the c2d team. We are delivering mosaics and catalogs for 5 large clouds, 82 small cores, and 189 regions around weak-line T Tauri Stars. We include discussions of our data processing, the products themselves, and tests of completeness and reliability, as well as a brief section on how to use the catalogs. We also discuss the various artifacts that have been corrected and those that may remain in the data. A table lists all the column headers in our source catalogs and refers the readers to sections or tables with more information. We include several new products, including our full archive and catalogs of candidate young stellar objects. We also deliver catalogs from the SWIRE survey that have been processed by us and modified to simulate how the c2d observations would detect the extragalactic background. Changes from previous deliveries include location-dependent corrections for IRAC, 70 $\mu$m photometry, improved estimation of the uncertainties, "band-filling" of fluxes for sources seen at other wavelengths, and an improved classification system. While still imperfect, the new classification system should provide a much more secure set of young stellar (or substellar) objects.

## Contents

## 1. Introduction

This document describes the fourth and final delivery of IRAC and MIPS data from the "From Molecular Cores to Planet Forming Disks" (c2d) Legacy team. IRS data were delivered separately with their own documentation (Lahuis & Kessler-Silacci 2006). Data for this delivery include all targets in the c2d program. We use data products from the S13 pipeline, as that was the most recent version available when we started our reprocessing.

There are important differences between this delivery and previous products. The products we delivered in late 2005 have been used by a number of people, so we ask the SSC to retain the document describing those products, along with the products themselves. However, we consider the new products to be substantially superior, and we encourage anyone that is not too far along in analyzing the 2005 delivery to switch to these, hereafter referred to as the 2007 products or Delivery 4 Products.

As we describe in more detail later, the 2007 products include the following changes from the 2005 products.

1. All the c2d data are now available and are delivered.
2. We include location-position-dependent photometric corrections to IRAC data (§2.1).
3. We have extracted sources to a deeper level in the MIPS1 observations of cores and stars (§2.3.2).
4. The photometry has changed because of the previous items and from small changes in parameters used for source extraction (§2.3).
5. We have adjusted the uncertainties based on comparison with deeper observations of some fields (§3.5).
6. We supply 70 $\mu$m data from a uniform (though done by hand) procedure for source extraction (§2.3.5).
7. We have "band-filled" the catalogs by giving a best estimate of the flux in bands without clear detections at the position of sources clearly detected in some other bands (§2.3.4).
8. We classify sources using improved criteria for separating YSOs from background galaxies (§2.5).
9. We supply several kinds of catalogs, useful for different projects (§3.2).
10. For three clouds with Bolocam data, we supply catalogs of cores at 1.1 mm (§3.2.3).
11. For Perseus, we supply a catalog of transient sources, likely to be asteroids (§3.2.4).
12. We supply extinction maps of the five large clouds (§3.7).

13. We supply catalogs of a selected region of the SWIRE survey (Lonsdale et al. 2003), useful for comparison to our clouds, but **not** for extragalactic research (§3.8).

The observational strategy was described in detail in Evans et al. (2003). An important aspect to bear in mind is that the IRAC and MIPS maps covered very different areas in many cases. Typically, the MIPS coverage on the five large clouds, taken in fast scan mode, covered a much larger area than did IRAC. Thus the full catalogs may contain many sources with MIPS photometry but no IRAC photometry. In contrast, the observations at 70 $\mu$m (MIPS2) on the small cores were taken in photometry mode and missed substantial area covered by IRAC. The edges of maps will also have only 2 of the 4 IRAC channels because of the offset inherent in the IRAC instrument. These differences have consequences for the various catalogs described in §3.2.

In addition to this document, users of the c2d data can find information in the following papers describing the IRAC results (Harvey et al. 2006; Jørgensen et al. 2006, Porras et al. 2006), the MIPS results (Young et al. 2006, Rebull et al. 2007, Harvey et al. 2007c, Padgett et al. 2007, Chapman et al. 2007), or the combined results (Harvey et al. 2007b, Alcalá et al. 2007).

The organization of this document is as follows: a brief summary of the delivery (this section); an account of the analysis of the IRAC and MIPS data (§2); a more detailed description of the data products (§3); and a summary (§4).

### 1.1. Overview of the Products

The data products are summarized in Table 1 and described more fully in §3. The data products include mosaics and source catalogs for 82 small cores, 178 weak-line T Tauri Stars (wTTS) regions, and five large clouds and associated off-cloud regions. We also deliver information on where to find an additional 11 wTTS regions for which no separate mosaics or catalogs are delivered since they were covered in our cloud maps by both the IRAC and MIPS instruments. Tables 2 and 3 give the full lists of cores and wTTS regions, respectively. For each of the 82 cores, Table 2 lists the core name, the status of the IRAC and MIPS data, the number of epochs observed, whether or not the IRAC data included high-dynamic range (HDR) observations, and the file code for the IRAC data. Table 3 gives similar information for each of the 189 wTTS regions, except that it does not list the number of epochs observed since all wTTS regions were observed in one epoch. A more detailed explanation of the columns giving the status of the IRAC and MIPS data for the wTTS regions can be found in §3.3.

#### *1.1.1. Images*

For IRAC data with HDR observations, we deliver mosaics both with (labeled COMB) and without (labeled A) the HDR data (see §2.3.1). We deliver mosaics of the MIPS2 (70 $\mu$m) data

based on the plain BCD product from the SSC, but with corrections (described in §2.2.2) that show the extended dust emission better. These mosaics should not be used for point-source extraction. We also deliver mosaics of the filtered data, which we used for point source extraction for faint sources (§2.3.5). We deliver mosaics of the MIPS3 (160 $\mu$m) data made directly from the plain BCD product. We do not have 160 $\mu$m data for the cores; we have 160 $\mu$m data for 4 stars, so we deliver these 4 mosaics.

For the five large clouds, the areas of the IRAC mosaics are identified in Table 4 and the MIPS mosaics in Table 5, with the rough center position of each area. We also list in these tables the positions of off-cloud areas near the clouds, which can be used to assess background counts, and we note whether each off-cloud region was observed by IRAC, MIPS, or both. For some clouds (Ophiuchus and Lupus) there is more than one separate cloud region (see Evans et al. 2003), and these images are delivered as separate files (e.g., OPH_NORTH). For the two largest clouds, Perseus and the main part of Ophiuchus, we deliver the cloud images in several separate sections (e.g., OPH_L1689_ALL and OPH_L1688_ALL), with maps of coverage and uncertainty. We also deliver full mosaics of those two clouds (e.g., OPH_ALL), but uncertainty and coverage maps are not available for those full mosaics for technical reasons. We deliver mosaics at all wavelengths for the clouds, but the mosaics at 160 $\mu$m are based on the BCD products. When GTO data have become available to us, those data are included in the mosaics. In some cases, this has meant that the aggregate integration times are longer in some parts of the mosaics.

We also include maps of the extinction toward the five large clouds, based on averaging the extinction toward background stars (§3.7).

### *1.1.2. Catalogs*

The Full Catalogs of band-merged, band-filled sources are supplied for each cloud, cloud area, core, or wTTS area. Band-merging means that data from the Spitzer bands through MIPS2 (70 $\mu$m), along with 2MASS data, have been merged into a single catalog, primarily using position matching to decide which source gets associated with extractions at longer wavelengths (see §2.4.2 and §2.4.3). Band-filling is a process by which we assign a best-effort flux and uncertainty to a position which was detected at other wavelengths; many of these may be non-detections, so the quality flags (§2.4.5) and the extraction image type (assigned to $-2$ for band-filled fluxes, see Table 11) must be used to avoid over-interpretation. Source extraction for MIPS2 (70 $\mu$m) is largely a hands-on process, and it involves considerable judgment, especially in crowded regions. Source extraction for MIPS3 (160 $\mu$m) is even more primitive, and the low resolution and copious diffuse emission make it too dangerous to merge with other wavelengths. The Full Catalogs provide the most complete, but least reliable, list of sources and their properties that we have produced.

The High Reliability Catalogs and the YSOc Catalogs are derived from the Full Catalogs. By requiring certain values of the Quality flags (§2.4.5), we constructed the High Reliability Catalog, in

which the sources have a higher probability of being real. The criteria (§3.2.1) essentially require a good signal-to-noise detection in some bands; however fluxes in other bands may still be low signal-to-noise detections or band-filled fluxes. The YSOc Catalogs include only sources that satisfied the criteria to be **candidate** YSOs (Young Stellar or Substellar Objects), as described in §2.5.4 and more fully by Harvey et al. (2007b). High Reliability Catalogs are delivered for each cloud, core, and wTTS area; YSOc Catalogs are delivered only if they are not empty. We also deliver a YSOc Catalog for the ensemble of the clouds and one for the ensemble of the cores.

We also include Full Catalogs, High Reliability Catalogs, and YSOc Catalogs of sources from a **degraded** version of the ELAIS N1 field of the SWIRE data that we have modified to simulate our data and processed through our pipeline. These catalogs are suitable for studies of background extragalactic contamination, but **not** for studies of galaxies (§3.8). We also include two specialty catalogs. The first is a catalog of millimeter emission sources from our ancillary Bolocam data toward 3 large clouds, which has been correlated with our Spitzer data (§3.2.3). The second is a catalog of transient sources in Perseus, useful for statistical studies of asteroids (§3.2.4). All catalogs present sources in order of increasing right ascension.

Finally, we include a quality file for each large cloud, core, or wTTS area (§3.3).

## 2. Processing of IRAC and MIPS Data

The Basic Calibrated Data (BCD) from the Spitzer Science Center were processed by the c2d team to improve the quality of the BCD images and the final mosaics produced for each cloud, core, and star-field observed. These improved images were used to create catalogs of source identifications and photometry.

The details of our procedure are given in the following sub-sections. The overview is as follows. The BCD images were examined and corrections were applied for artifacts (e.g., muxbleed, column pulldown, banding, jailbar features) and known calibration problems (e.g., location-dependent photometric corrections). The resulting improved BCD's were mosaicked using the SSC Mopex tool with outlier rejection. Source extraction was done on these images utilizing a specialized version of "Dophot" which we developed. The source lists for each band were compared with the images to remove false sources caused by diffraction spikes, saturation, and other imperfections. The source lists for each band were merged and missing fluxes were band-filled to create the full catalogs. Finally, various refined catalogs were derived from the full catalogs.

The above procedure was implemented within the c2d team as a series of steps with internal products at each step. We now describe each of those steps.

## 2.1. Characterization and Calibration of IRAC Data

The raw IRAC images were reduced by the Spitzer Science Center (SSC) using Version S13 of their standard IRAC pipeline to produce BCD images. These BCD images were created by subtracting the dark and bias levels from the raw data, followed by flat fielding and sky subtraction. In addition, the SSC pipeline corrects for some artifacts present in the images and provides masks. For more details concerning the SSC processing of IRAC data, we refer the reader to the IRAC Data Handbook and the IRAC Pipeline Description Document available on the SSC webpage[1]. Instrumental signatures, pixels saturated by very bright sources, and bad pixels (those with atypical sensitivities) in the BCD images have been identified within SSC mask files.

### *2.1.1. Corrections for Jailbar Effects*

Version S13 of the SSC pipeline implemented many improvements in their processing of IRAC data, including better pointing refinement, linearity corrections, flat field determinations, and updated flux conversions. In addition, the darkdrift module, which corrected for vertical "jailbar" effects due to bias level drifts, was turned off for IRAC Bands 1, 2, and 4 in this version of the pipeline as a result of some on-orbit tests suggesting that such corrections were negligible except in IRAC Band 3. Subsequently, it was found that the jailbar effect indeed can be triggered occasionally in IRAC Bands 1, 2, and 4 and therefore the module was turned on in later versions of the pipeline. Since we are processing S13 BCDs for this final delivery, we obtained the jailbar corrector from the SSC and applied these corrections to all IRAC Bands 1, 2, and 4 BCDs prior to any processing by our pipeline.

### *2.1.2. Creation of c2dmasks*

With each AOR, the SSC releases two mask files (pmask and dmask) that identify most pixels affected by various peculiarities. The purpose of the pmask is to identify pixels that are permanently damaged or those that have exhibited dark currents or sensitivities consistently too variable or atypical to be reliable. The purpose of the dmask, on the other hand, is to identify pixels that are affected by various peculiarities, some of which do not render a pixel non-usable or "bad". One pmask is sufficient for each band in an AOR, while a dmask is released for each IRAC BCD image.

To help simplify our characterization of IRAC BCD images, we create our own pixel mask, known as a c2dmask, for each image. The c2dmask indicates which pixels in the image were considered by the *c2d* team to be good, represented by a pixel value of "0" in the c2dmask, and

[1] http://ssc.spitzer.caltech.edu/irac/dh/

which pixels were considered bad, represented by a pixel value of "1". We further identify pixels affected by muxbleed (see §2.1.3) with pixel values of "2" and consider these to be good pixels for the purpose of this data delivery.

Bad pixels identified by a c2dmask are determined by: (1) examining the pmask to include "permanently" damaged pixels, (2) examining the dmask to include pixels uniquely bad for that image, and (3) searching the BCD image for any bad pixels not included within the pmask or dmask. Specifically, all pixels with any bits set in the pmask are considered bad and indicated as such in the c2dmask. In addition, pixels with either of Bits #5, 8–14 set in the dmask are also considered bad by the c2dmask. Finally, we examine each BCD image to identify pixels exhibiting values "substantially different" from those non-masked pixels immediately surrounding it in order to identify bad pixels not identified by the pmask or dmask. We consider a pixel value that is $20\sigma_s$ greater than or less than the mean of the surrounding pixel values as "substantially different," where $\sigma_s$ is the dispersion of the surrounding pixel values. This criterion is effective for identifying isolated, grossly bad pixels not identified by the dmasks or pmasks, while not falsely identifying pixels near the peaks of stellar point spread functions (PSFs) as bad pixels. This method is not effective for automatically identifying streaks of bad pixels, which are due to inclined cosmic ray hits. But, such streaks are well detected and mitigated later in the pipeline by *mopex* (see §2.3.1). The typical numbers of bad pixels, derived solely from the pmasks and dmasks delivered by the SSC for a sample of the data in this delivery, are listed in Table 6. Table 6 also lists the typical total numbers of bad pixels as identified in the c2dmask, which includes SSC bad pixels and those found by our search. Comparison of these numbers demonstrate that >95% of the bad pixels are identified in the pmasks and dmasks.

### *2.1.3. Removal of Bright Source Artifacts*

In addition to masking bad pixels, we identify pixels in BCD images afflicted by known artifacts and apply corrections to minimize the effects of these artifacts. The corrected images were written as ICD (Improved Calibrated Data) images. Muxbleed, pulldown, and banding features are artifacts known to occur near moderately bright sources. Muxbleed occurs in the rows on which these sources are centered in Band 1 and Band 2 images; banding occurs in the rows in Band 3 and Band 4 images. Pulldown, primarily seen in Band 1 and Band 2 images, occurs in the columns containing moderately bright sources and is corrected in all IRAC bands.

We use an IDL procedure provided by D. Stern (JPL and GOODS Legacy Team), to detect and correct pixels affected by muxbleed. This procedure searches for pixel values greater than 10,000 DN, which arise from either moderately bright sources or cosmic ray hits. Such pixels are known to be the source of muxbleed. Muxbleed pixels caused by a pixel with value between 10,000 DN and 30,000 DN are corrected by interpolation of a table of predetermined corrections as a function of distance from the muxbleed source. Muxbleed arising from pixels with values greater than 30,000 DN is corrected by fitting an empirically derived function to the muxbleed pixel values.

The muxbleed corrector was written specifically for IRAC Band-1 images, but we also apply these corrections to Band-2 images. Visual inspection of these images suggests these corrections improve the Band-2 images as well. Figure 1 displays a Band-1 BCD image affected by muxbleed alongside the ICD image resulting from applying the muxbleed corrections. While the procedure is very reliable in detecting pixels affected by muxbleed, the corrections are not always sufficient to remove the muxbleed artifacts, particularly when the corrections are relatively large. Nevertheless, the corrections improve the image quality and therefore are applied.

To correct for column pulldown and banding effects, we use two IDL procedures provided by R. Gutermuth (Smithsonian Astrophysical Observatory). The procedure for column pulldown is a somewhat revised version of a post-pipeline procedure previously provided by the SSC. Comparison of results of running the pulldown-correcting procedure in our pipeline with those from the current post-pipeline SSC pulldown-correcting procedure demonstrates that the resulting corrections do not differ significantly between the two procedures.

The corrections for pulldown are additive constants applied to the affected columns of an image. After masking bad pixels, the median pixel value of each column is computed. The ensemble of these median values form a projected median-valued row, which is compared with a smoothed version of this projected row to identify columns with discrepant median pixel values, presumably due to the column pulldown effect. The pixel values in the deviant columns are then shifted to match the median of the smoothed projected median-valued row. This algorithm searches for deviant columns rather than the moderately bright sources that cause column pulldown; thus, it is possible that the algorithm could automatically apply inappropriate pulldown corrections to columns on which no moderately bright sources are positioned. However, the parameter values involved in the algorithm have been optimized and tested such that very rarely, if ever, are columns corrected that are not affected by pulldown. These procedures are very reliable in both detecting and correcting columns affected by pulldown. Figure 1 demonstrates the typical result of applying the column pulldown corrections to BCD images. A similar algorithm is employed to detect and correct rows affected by banding in Bands 3 and 4, though the derived banding corrections are sometimes not sufficient to remove these artifacts. Even so, the banding corrections are never over-corrections and represent improvements in image quality; therefore, these corrections are applied.

In order to provide an idea of the extent to which muxbleed, column pulldown, and banding are observed in the BCD images, the percentages of short-exposure BCD images (i.e., those with 0.6-second frametimes) and long-exposure BCD images (i.e., those with 12-second frametimes) corrected for these artifacts are compiled in Tables 7 and 8, respectively. Since the number of images affected by these artifacts is dependent on the observed region, and may vary considerably, the percentages in the table are simply quoted to the nearest 10% and represent a median derived from a sample of our observations. Most of our long-exposure Band-1 and Band-2 images are affected by muxbleed and column pulldown, while about 20–50% of our Band-3 and Band-4 images are corrected for banding or pulldown.

### *2.1.4. Corrections for the First-Frame Effect*

Another artifact present within the BCD images is known as the first-frame effect. The bias level of a raw image depends on the elapsed time between obtaining the image and the previous observation. These bias levels have been properly removed during the SSC pipeline to reduce raw images to BCD images, with the exception of the first long-exposure image (i.e., 12-second or 30-second image, in our case) of Band 3. An example of the improper bias-subtraction can be seen in Figure 2. To mitigate the first-frame effect in the first long-exposure, Band-3 image in our observations, the first Band-3 image obtained in each AOR is a short-exposure (i.e., 0.6-second) image. In this way, the elapsed time between the first long-exposure, Band-3 image and the previous image is the same in all our AORs. Thus, these BCD images themselves can be used to correctly subtract the residual bias remaining in these images after the SSC pipeline.

Our procedure for correcting the first-frame effect in IRAC Band-3 observations of a particular molecular cloud involves constructing a *bias-correction image*. We begin constructing this bias-correction image by collecting all the first long-exposure Band-3 images from the set of AORs for that cloud. For each of these images, the median pixel value in the image is subtracted from all the pixels. Then, a median-filter stack of these images, followed by a subtraction of the median pixel value, results in the bias-correction image. After correcting for any banding or column pulldown artifacts in the original Band-3 BCD images, the bias-correction image is subtracted from the first of these long-exposure images in each AOR. For the purposes of constructing the bias-correction image for the cores, we make use of the entire set of AORs for cores. Similarly, the bias-correction image for the star fields was constructed from the entire set of AORs for these star fields.

### *2.1.5. Location-Dependent Photometric Corrections*

The last corrections that we applied to the BCD images were the location-dependent photometric corrections. These photometric correction images are available from the SSC. Prior to applying these corrections, the photometric correction images need to be divided by images of the relative pixel area, also provided by the SSC. Then, after multiplying the BCD images by these normalized photometric correction images, *c2dphot* or *mopex* may be used to construct a mosaic and properly transform the pixel values (representing surface brightnesses, given in MJy/ster) to fluxes (e.g., mJy).

Figures 3 and 4 illustrate the effect on the photometry of making these location-dependent corrections. Figure 3 shows distributions of the corrected pixel values in the images relative to the non-corrected values. Assuming that sources are uniformly distributed on the detector, in general, this distribution should then indicate the effect of these location-dependent corrections on the fluxes of these sources. We see that corrected IRAC1 and IRAC2 fluxes are typically very similar to the non-corrected fluxes, usually differing by $<1\%$. The corrected IRAC3 and IRAC4 fluxes are typically (meaning the mode) $\sim$1–2% greater than the non-corrected fluxes, but the location-

dependent corrections yield a much broader distribution of flux adjustments. Similarly, the effects on some commonly used IRAC colors are shown in Figure 4. In general, the distributions of color adjustments are broader than the distribution of flux adjustments due to the differing structure of the location-dependent corrections (e.g., location-dependent corrections for IRAC3 images generally increase from the left side of an image to the right side, whereas the corrections for IRAC4 tend to be in the opposite sense). Tables 9 and 10 summarize the effect on the location-dependent corrections on the photometry, though we caution that the distributions are not normal.

As described in SSC documentation these corrections are strictly applicable only for point-like sources exhibiting a Rayleigh-Jeans spectrum, consistent with a majority of sources listed in our catalogs — at least those detected in at least three bands such that their SEDs could be characterized. For redder sources such as YSOs, these corrections may have introduced small systematic offsets in their photometry. According to Table 9, the fluxes in our catalog for the modal source will be overestimated by ∼0.5% at IRAC1 and IRAC2 and ∼2% at IRAC3 and IRAC4. However. the distribution is skewed in such a way that **underestimates** can be larger in a small number of sources. The flux uncertainties of red sources will be larger; adding in quadrature the dispersions listed in Table 9 to the flux uncertainties quoted in our catalogs will at least approximate the increased uncertainties.

#### *2.1.6. Pests that Escape the c2d IRAC Pipeline*

We do not mask stray light that appears in some of the IRAC images. This stray light originates from bright sources just outside the field of view that scatters onto the detector. This stray light can sometimes closely resemble nebulosity or emission from outflows associated with young stellar objects. For this reason, particular care must be taken to ensure that identifications of nebulae and outflow emission are not artifacts resulting from stray light.

### 2.2. Characterization and Calibration of MIPS Data

MIPS images were processed by the Spitzer Science Center (SSC) using the standard pipeline to produce Basic Calibrated Data (BCD) images and related mask and uncertainty files. The SSC pipeline version was S13. For further information, see the MIPS Data Handbook, available at `http://ssc.spitzer.caltech.edu/mips/dh/`. The BCD images were corrected by us for some, but not all, instrumental signatures. This delivery was done with version 4 of our software.

Our data reduction consisted of automated inspection of all images for elevated noise levels, visual inspection of a subset of images, the creation of masks for questionable pixels, and, for the 24 $\mu$m data, corrections for some of the known imaging defects. The masks were a merging of SSC pipeline pmask and dmask masks with bits deemed fatal into a simpler mask with 0 = good and 1 = bad. For 160 $\mu$m data, some pixels could stay anomalously high or low during an AOR, but

not be consistently given a bad mask by the pipeline. These were identified and masked within that AOR. No new uncertainty files were created.

No attempt was made to explicitly remove cosmic rays or bright latent images from the BCD images. We used either the redundancy and outlier rejection in mosaicking, or inspection, to avoid mis-identifying these as point sources.

### *2.2.1. 24 μm Data*

With the 24 $\mu$m array, a "jailbar" response pattern, repeating every fourth column sharing the same readout, is caused by bright sources and some cosmic ray hits. We applied an additive correction to each BCD data frame for any detectable fixed-amplitude jailbar pattern across the array, bringing lower columns up to the level of the highest columns. For some data, we corrected the jailbarring in sections: rows above and rows below a bright object. Figure 5 shows a BCD image before and after a two-section correction.

"First frame" corrections were also applied. Scale factors were applied to the first four frames in a photometry map or scan leg to bring them up to the median of subsequent frames.

Finally, 24 $\mu$m frames were median-combined with outlier rejection to create "self-flats". These were needed to correct for residual low-level jailbarring, incompletely-corrected illumination patterns, a 1-2% gradient along the column direction, and occasional dark latent images. If bright stars or extended emission were present in a photometry map, then a flat obtained from another photometry observation near in time was used. In photometry mode, the flatting was done separately for on- and off-source data. In scan maps, the flatting was by AOR. By "self-flatting", any true sky brightness gradient that is constant across the field covered by the median-combined images was also removed. For photometry mode, fields are of order 100 arcmin$^2$; for the scan map AORs, of order 1 degree$^2$. To study emission on these scales, one must return to the original BCD data. In addition, spot patterns from dust on the pickoff mirror were present in the "0" frames of scan maps. These were divided out with separate spot-pattern flats created from the data.

No corrections were applied for improper "droop" corrections. This causes an overall offset in frames containing saturating objects. A background matching routine in the Mopex toolset, overlap.pl, was used to correct for offsets when creating the 24 $\mu$m mosaics.

Other instrumental signatures, e.g., short-term dark latents, column and row pulldown effects, and streaks extending from bright objects, have not in general been corrected, though some preliminary additive corrections for column and row pulldown were done in a few cases.

Uncertainties resulting from these corrections to the pixel values are estimated to be typically $\lesssim 0.2$ %, and the resulting uncertainties in point-source fluxes typically $\lesssim 0.03$ mJy. This is usually small compared to other sources of uncertainties.

#### *2.2.2. 70 and 160 μm Data*

The Ge data (70 and 160 $\mu$m) contain several instrumental signatures, including pixel response variations, latent signals from the stimulator, and poor stimulator corrections. The SSC provided 2 types of BCD images: normally processed (unfiltered) and those with time-median and column-median filters applied that removed most of the background signal (filtered).

Following the current recommendation of the SSC, we used the 70 $\mu$m filtered data to identify and do photometry on faint sources, and the 70 $\mu$m unfiltered data for photometry of bright sources. For 160 $\mu$m sources, we used the unfiltered BCD data. Because we are still working on verifying the reliability of 160 $\mu$m point source extractions in light of the instrumental signatures, we are not including point source fluxes for 160 $\mu$m in this delivery.

We are ultimately interested in estimating fluxes for both point sources and extended emission within the clouds. However, the fluxes of extended emission regions in Spitzer 70 and 160 $\mu$m BCD data are uncertain at the present time due to the instrumental signatures.

For this delivery, we made 70 and 160 $\mu$m mosaics using filtered and unfiltered data, using the bad pixel masks created in our processing.

### 2.3. Mosaicking and Source Extraction for IRAC and MIPS

#### *2.3.1. Image Mosaicking*

Our primary tool for mosaicking is the Spitzer Science Center's "Mopex" code as described on the Spitzer web pages. This code includes a continuously evolving set of modules that correct for some problems in the BCD-level images and attempt to piece many BCD's together into large mosaics. Optional modules exist to, for example, filter out radiation hits (outlier rejection), correct for zero-point differences between BCD frames (overlap correction), and to correct for small positional errors in the FITS headers (position refinement). For the data in this delivery, we have used Mopex (version 030106) with the outlier rejection and overlap correction modules turned on, but with position refinement turned off. We have experimented with a range of parameters for outlier rejection and tried to pick the best compromise between rejecting radiation hits and asteroids versus eliminating so many "good" images that source fluxes/profiles are affected. A fairly detailed check of a range of images suggests that: 1) rad hits are probably eliminated at well above the 99% level in the combined-epoch mosaics, and perhaps at the 98% level in the single-epoch mosaics; 2) asteroids are eliminated at about the 98% level in the IRAC combined-epoch mosaics, and at about the 90% level in the MIPS combined-epoch mosaics. Note however that not all observations have data from 2 epochs. We obtained only single-epoch observations toward the wTTS and 38 cores at high ecliptic latitudes, where asteroids should be rare.

As part of its standard processing, Mopex makes use of mask files to avoid including BCD-level

pixels in the final mosaic that have been identified as having some problem. For our mosaics we have used a combination of the masks provided by the initial c2d processing together with the outlier masks constructed during the outlier-rejection processing by Mopex. As described earlier (§2.1 and §2.2), the c2dmask combines the bad pixel masks ("pmask") and the bad detection masks ("dmask") from the SSC and adds bad pixels found in our data inspection process.

For regions where we have IRAC high-dynamic-range data, we have made use of these frames to produce mosaics in which stars that are saturated in the longer exposure frames, but not in the short exposure ones, are reasonably accurately represented in the final mosaics. This was accomplished by: 1) producing a source extraction list from a mosaic of the short exposure images; and then 2) masking the pixels in the long exposure c2dmasks in both epochs where we determined empirically that the flux was likely to be saturated. The very small number of sources that are saturated in the short exposure images are not corrected, of course, by this procedure. The list of mosaics and extraction tables for "standard" IRAC data with HDR frames includes: 1) the short exposure data (typically from the first epoch); 2) long exposure data from each epoch individually combined with the short exposure frames to deal with saturated sources; 3) the combined-epoch long exposure data alone; and finally, the combination of all data from both epochs. For MIPS24 we process each epoch independently as well as the combined-epoch data, for a total of three separate data sets. For all of the above, we produce both an extraction list from the mosaic "...c2d.tbl" and one from a multi-frame fit to the BCD data, "...c2dmtot.tbl".

For the 2007 delivery, we have included both the mosaic without the HDR data (labeled "A") and the mosaic with the HDR data added in (labeled "COMB") when HDR data were available. Tests indicated that adding the HDR data slightly increased the noise level, so the "A" mosaic may show lower noise, but the "COMB" mosaic will represent the overall dynamic range better. For IRAC mosaics without HDR data and for MIPS, we deliver only the "A" version mosaics that combine both epochs of data with optimally tuned outlier detection. See Tables 2, 3, and 4 for information on what is available.

The geometry of the mosaics constructed with Mopex for this delivery was such that we kept a 1:1 pixel size ratio between the basic instrument pixel size and mosaic pixel size, and we assembled the BCD images in a coordinate system essentially fixed with respect to the average instrument rotation projected on the sky. The former obviously minimizes file sizes and processing time for this processing. The latter simplifies the process of point source extraction from the mosaics since the instrumental PSF will have the same rotational orientation for any mosaic.

Some parts of Mopex, especially the source extraction, require estimates of the noise in the individual images and/or the mosaic image. Mopex produces noise (uncertainty) mosaics and coverage mosaics that display respectively the uncertainty level in the image mosaic and the effective number of overlapping BCD frames at each pixel. For the noise estimates Mopex can use either user input estimates of the read noise and system gain (to estimate photon statistics), or the BCD level uncertainty images supplied by the SSC. We have used the SSC's BCD uncertainty (bunc)

images for noise estimation. (See, however, §3.5.)

### *2.3.2. Source Extraction*

The process of source extraction involves finding likely compact objects in the data and characterizing them by flux, position, and possibly some estimate of the way in which they might differ from a "perfect" point-like object. The details of our point source extractor will be described by Harvey et al. (2007a), but we summarize here the main points.

The source extraction tool, c2dphot, is based on the venerable "Dophot" code described by Schechter, Mateo, and Saha (1993). Our version includes the following important modifications to Dophot: (1) utilizes a digitized point source profile rather than an analytic one to best match the real Spitzer data; (2) accepts floating point input FITS images and computes output fluxes based on the Spitzer surface brightness units in the BCD-level images; (3) accepts input masks to avoid using pixels that have been declared bad for whatever reason; (4) includes a multiframe mode, which fits fluxes and positions from the entire stack of BCD frames relevant to any input source position, using the un-smoothed instrumental PSF rather than that produced by the mosaicking process. The most significant unchanged aspect of c2dphot/Dophot is the basic source extraction process. In particular, c2dphot starts at an upper flux level, finds and characterizes sources above that level, and subtracts them from the image. It then works its way down in flux, typically by a factor of 2 step each time, doing the same thing until it reaches the lower flux limit that is input by the user. If c2dphot finds an object that is better fitted by a two-axis ellipsoid than the numerical point source profile, it will classify the object as extended and produce estimates of the source size and tilt of the ellipse, just as Dophot does.

Like any source extractor, there are many tunable parameters in c2dphot to enable it to deal with a variety of problems or characteristics in the data. The most sensitive parameters for both accurate source extraction and photometry are the sizes of the search box, fitting box, and aperture photometry boxes. For these data we used a search box size of 5 pixels for IRAC bands 1 to 3, and 7 pixels for IRAC band 4 and MIPS band 1. We used aperture boxes of 7 pixels side-to-side for all bands and a fitting box of 9 pixels for IRAC bands 1 to 3 and 11 pixels for IRAC band 4 and MIPS band 1. These sizes were chosen based on a number of tests on simulated data sets as well as a variety of real data from Spitzer. These sizes are slightly smaller for some bands than for previous deliveries, resulting in a larger number of sources being detected at faint levels since less background contributes to the search test. Other tunable parameters include thresholds for deciding whether a source is extended, whether an initial detection is better fitted by a tilted plane, and whether a source is so small that it is more likely to be a previously undetected radiation hit. These have all been tuned to levels that appear appropriate from careful visual inspections of subsets of the data. The criterion for categorization of a source as extended has also been changed slightly from previous deliveries, resulting in a somewhat smaller number of sources classified as extended.

Since several of these extraction parameters have been adjusted slightly since our previous delivery, even if the input BCD frames had been unchanged, i.e., S11 not the current S13, the resulting photometry would have changed, and indeed it has changed by typically several percent in most cases. Furthermore, we made a change in the way the flux is calculated for sources that were found to be more extended than pointlike objects. In particular, for consistency of comparison with the fluxes at other bands where many of such objects were not found to be extended, we opted to use the flux that results from fitting a point source PSF to the object, but record in the source extraction type that it was found to be extended. For objects that are not very different from pointlike in one or two bands, this allows more accurate colors to be derived for the objects.

An additional tunable parameter is the depth to which the source search is pursued in the image. This is basically just the flux level above the local background to which the search algorithm goes in looking for objects above a minimum S/N. For some subsets of our data we have set this parameter a factor of 3 – 5 deeper because of either longer integration times or generally better S/N than the typical data sets. The 24 $\mu$m sources in the cores and star fields were extracted to a 3 times deeper level than in our standard processing, and SWIRE sources were extracted to a 5 times deeper level in all bands.

The details of the c2dphot source extraction processing for all IRAC bands and for MIPS 24 data involve running the source extractor first on the mosaic image produced by Mopex. Then the multi-frame option is run with the output list from the previous processing given as an input list for flux, position, and shape refinement, but no new source searching. As mentioned above, this insures that the source characteristics are derived from the least-processed form of the data, the BCD-level products. Also, the mosaics made from Mopex do not conserve flux and should not be used for source extraction.

The calibration of source fluxes is done in the following way. All objects for which a reliable aperture flux could be determined and which were well fitted by the nominal point source profile were used to calculate an averaged ratio of aperture flux to model flux. This ratio is not unity since the model fluxes are essentially the product of the fitted peak value multiplied by the PSF area. Small errors and uncertainties in the PSF area lead to errors in the total model flux. We then assume that this average ratio of aperture flux to model flux applies for all point sources and multiply by an additional correction factor for the aperture used in c2dphot relative to that for the absolute calibration used by the SSC (essentially a traditional "aperture correction").

### *2.3.3. Uncertainties*

Flux and position uncertainties in c2dphot are calculated in a standard way from a numerical estimate of the Hessian matrix (Press et al. 1997; Sivia 1996). In particular, the matrix of partial gradients of chi-squared is calculated numerically for variations in the four model parameters (for point sources). This is done by fixing each parameter at levels slightly offset above and below

the best fit parameter and calculating the change in chi-squared for all combinations of offset parameters. The diagonal elements of the square root of the inverse of this matrix then give an error estimate, at least in the case where the errors are reasonably behaved. A random check of the off-diagonal elements has shown that the only significant correlation between error estimates is that expected between the derived sky level of the fit and the peak star amplitude. For extended extractions a similar procedure is part of Dophot and c2dphot using analytic, rather than numerical, estimates of the derivatives. The image type is also returned and supplied in our final catalog of sources (§3.2). The values have the meanings given in Table 11.

This procedure for estimating uncertainties, although statistically correct, appears to underestimate the uncertainty as measured by the repeatability of flux measurements that we describe in §3.5. For objects with low S/N, we find that the nominal statistical uncertainty needs to be increased by a multiplicative factor of 2.3. For bright sources, there appears to be a floor to the best uncertainty possible with our observing techniques of 0.047 magnitude for the IRAC bands and 0.095 mag for MIPS band 1. Therefore, the uncertainties in the delivered catalog have been adjusted to reflect these increases.

### *2.3.4. The Band-Filling Process*

A new feature in this data delivery, as mentioned earlier, is the inclusion of band-filled fluxes. If a source is believed to be real at one or more wavelengths (see §2.4.4 for the criteria), but it was not found in the original extraction process at some other wavelength, c2dphot can be set to fit a PSF profile at the fixed position of the known source. This is a very simple process since it is a linear fit with two parameters, source amplitude and background. This processing step happens after all the sources found by the standard extraction step have been subtracted from the image. Typically this is most useful for sources that are clearly visible in the shorter IRAC bands but undetected at some or all longer wavelengths. In crowded regions, this process can produce incorrect results at 24$\mu$m because the 24$\mu$m PSF is so much broader than the IRAC ones that a faint source near a bright one can be detected with reasonable S/N in the bandfilling process simply because the wings of the bright source are not completely subtracted from the image, because of imperfect knowledge of the PSF.

In using these data, it is important to know that the flux has been band-filled. This can be determined from the image type (see §3.2).

### *2.3.5. Photometry at 70 $\mu$m*

Photometry for the S13 70 $\mu$m (MIPS2) data on the clouds and cores was done with the SSC's MOPEX point-source fitting package on mosaics at the PBCD pixel scale. These mosaics combined data from both epochs, when two epochs were available. Generally, filtered BCD data

was used. If a bright source is present, the SSC's filtering overcorrects in the wings (Note: this occurs around F(70) $\sim$ 2 Jy), so results for the plain BCDs were inserted instead. Plain BCD pipeline uncertainties were used. The listed flux values are for point sources, and just those point sources considered reliable. But sometimes a source is included even if it is extended. These have imtype = 2.

When a 70 $\mu$m point source was saturated, we were sometimes able to determine the flux by fitting the wings with a point source. (Note: point-source saturation in low backgrounds occurs around F(70) $\sim$ 23 Jy.) This wing-fitting procedure has an uncertainty of 20% which was included in the listed uncertainty. However sometimes the saturation on source plus background was so severe that, even though the source may have been detected, no valid flux could be assigned.

Color corrections can be found in the MIPS Data Handbook. An overall absolute flux calibration uncertainty of 20% for the MIPS 70 $\mu$m photometry should be added to the uncertainties that we provide.

## 2.4. Band-Merging and Source Characterization

To create the delivery catalogs, the output lists from the source extraction for each band and object were inspected and combined into an integrated source catalog. Bandfilled fluxes (§2.3.4) were included in the catalog. This section outlines the procedure used to compile the Full Catalog and characterize the quality of the fluxes and sources therein. The description of the other catalogs constructed from this primary catalog are given in §3.2.

### *2.4.1. Producing Epoch-Merged Source Lists*

The majority of our regions were observed at two epochs separated by 4-8 hours. For each band, the three source extraction lists (epoch1, epoch2, and combined epochs) were created based on images from the respective epochs (§2.3.1). These lists were checked for "self-matches" within an epoch; two sources extracted within one epoch, but with positional matches of $\leq 2\farcs0$ were considered to be the same source. The fluxes of the detections were summed; the position of the source was calculated as the weighted mean; and the quality of detection flag in the catalog was set to 'K', or complex (see §2.4.5 for a description of these flags). The three lists were then merged to cross-identify sources with positional matches of $2\farcs0$ or less.

The epoch-merged source lists for each band were visually inspected to remove diffraction spikes, column pull-down, latent images, and other image artifacts which were misidentified as sources. This inspection typically yielded hundreds to thousands of false sources in IRAC Bands 1 and 2 which are generally associated with image artifacts, fewer in the other bands. They represent a small percentage of the total number of sources.

### *2.4.2. Producing IRAC-MIPS1 Band-Merged Source Lists*

For wavelengths shortward of 70 $\mu$m, the data were band-merged in an automated fashion in three main steps. First, the IRAC wavelengths were merged, then the IRAC-merged source list was combined with MIPS1, and finally the IRAC+MIPS1 merged list was combined with the 2MASS catalog.

The four IRAC bands were merged one-at-a-time, i.e. IRAC1 and IRAC2 were combined, then the IRAC1+IRAC2 data were merged with IRAC3, and finally IRAC1+IRAC2+IRAC3 was combined with IRAC4. A 2.″0 matching radius was used for each step. If there was more than one possible match in any step, the closer source was used. For example, if a source in IRAC1 is within 2.″0 of two or more IRAC2 sources, then the IRAC1 source will be matched with the closer of the IRAC2 detections, becoming a single IRAC1+IRAC2 source. The IRAC2 source that is further away will remain in the source list, but will not be matched with a source in IRAC1.

After all the IRAC bands were merged together into a single IRAC-merged source table, this list was combined with the MIPS1 data. For this comparison, a 4.″0 limit was used because of the larger PSF in the MIPS1 band compared to the IRAC bands. If there were multiple IRAC-merged sources within 4.″0 of a single MIPS1 detection, the MIPS1 detection was merged with the nearest IRAC-merged source; the remaining IRAC-merged sources were not merged with a MIPS1 detection.

Finally, the 2MASS catalog was combined with the IRAC+MIPS1 merged source list using a position matching criterion of 2.″0. The 2MASS source was always matched with the closest IRAC+MIPS1 source.

### *2.4.3. Producing IRAC-MIPS2 Band-Merged Source Lists*

For our clouds and cores, we also merged the source lists described above with the MIPS2 (70 $\mu$m) data. This is a new feature of this delivery.

At 70 $\mu$m, our observations were planned in such a way that the second epoch of data was offset with respect to the first. This offset was designed to fill in the holes in the map resulting from the bad side of the 70 $\mu$m array. Our final 70 $\mu$m mosaics and source extractions have only the combined epochs data, since only these data cover the full observed region (§2.2).

The MIPS2 source list was matched with the 2MASS+IRAC+MIPS1 merged source list from § 2.4.2 using an 8.″0 radius. Each MIPS2 detection was allowed to be matched with any number of shorter wavelength 2MASS+IRAC+MIPS1 sources within the 8.″0 radius. However, each 2MASS+IRAC+MIPS1 source could only be associated with one MIPS2 detection.

After merging, we visually examined each merged MIPS2 detection to determine the 'best' source match between shorter wavelengths (1.25 – 24 $\mu$m) and MIPS2 (70 $\mu$m). This 'best' source

match was the one with the most consistent Spectral Energy Distribution (SED) across all detected wavelengths. By consistent, we mean that we tried to choose sources such that the SED would consistently rise or fall at longer wavelengths. If multiple 2MASS+IRAC+MIPS1 sources would fit this definition, we tended to select the 'best' match as the one with a MIPS1 flux closest to the MIPS2 value. In a few cases where it was not clear which SED was 'better', we chose the closer positional match.

Shorter wavelength sources that were within 8.″0 of a MIPS2 detection but NOT matched with the MIPS2 detection, were assigned a special flag, 'Y', to denote their status (see § 2.4.5). Thus, in our final catalog, a 70 $\mu$m detection is listed ONCE; we did not try to split up the flux to different shorter wavelength sources. Furthermore, given the position uncertainties in 70 $\mu$m detections, we did not include this wavelength when computing the final weighted average position for the 2MASS+IRAC+MIPS1+MIPS2 source.

Some MIPS2 sources were either outside of the observed area at IRAC+MIPS1 wavelengths or had no counterpart at shorter wavelengths. If these sources appeared to be genuine instead of image artifacts we included them in the catalog.

### *2.4.4. Bandfilling*

IRAC1 and IRAC2 are the most sensitive wavelengths. As a result, there are a great number of sources in our catalogs only detected at one or both of these wavelengths. To remedy this situation, we decided to bandfill our catalogs (see §2.3.4). We considered only sources with a combined epochs detection of quality 'A', 'B', 'C', 'D', or 'E' (see §2.4.5) in at least one of the IRAC1-4 or MIPS1 wavelengths for bandfilling. This means that 2MASS-only sources, MIPS2-only sources, and sources with only a quality grade 'K' were not bandfilled. We created five bandfill source lists, one each for IRAC1-4 and MIPS1. Each list contains the positions of sources without a detection at the given wavelength, provided the position is within the combined epochs mosaic at the given wavelength, and not within 2 pixels of the edge of the mosaic.

We re-ran these bandfill positions through the source extractor to obtain fluxes at each postion, as described in § 2.3.4. We then re-integrated these bandfilled fluxes into the band-merged source list to obtain the final catalog. We used the same merging procedure as before, with the same matching radius, 2.″0. Since these bandfilled detections are not allowed to shift position from the initial list, it is easy to ensure that each bandfill detection ends up with the correct source.

Some bandfilled detections do not appear to correspond to an actual source in the mosaics. We judged that sources with a $S/N < 5$ to be upper limits and their quality of detection flag was set to 'U' (§ 2.4.5). After the re-scaling of the uncertainties (§3.5), this means bandfill sources with $S/N \lesssim 2.17$ are listed as upper limits in the catalog. All bandfill fluxes in the catalog have imtype= $-2$. Some sources have not been bandfilled because the source extractor has trouble fitting a flux for positions near the edge of a mosaic. These sources still appear in our catalogs.

**A band-filled flux may not be statistically significant and may even be negative.** Thus it is essential to use these with care. Together with the uncertainties, they provide the opportunity to give an upper limit to a flux at a particular wavelength for a source that is well detected at other wavelengths.

### *2.4.5. Data Quality Flags in the Catalog*

Four types of quality flags were assigned to each source based on a set of criteria. The first two are supplied for each band; the second two apply to a source after band-merging.

**Flag 1:** Quality of detection

This is the flag denoted in the catalog by XX_Q_det_Y, where XX is the band name and can be one of 'IR1', 'IR2', 'IR3', 'IR4' for IRAC bands 1-4, 'MP1' or 'MP2' for MIPS bands 1-2, or 'J','H', 'Ks' for the 2MASS bands. The epoch of observation is denoted by Y, which will be either '1','2', or 'c', for epoch 1, epoch2, or combined epochs. The quality flags in the 2MASS bands are identical to the ph_qual flag obtained from the 2MASS catalog. For all other wavelengths, each detection has a quality grade assigned to it based primarily upon its signal-to-noise (S/N).

| S/N | Grade |
|---|---|
| $\geq 7$ | A |
| $\geq 5$ | B |
| $\geq 3$ | C |
| $\geq 2$ | D |
| $< 2$ | E |

Several other grades are possible, which override the above ones. If the source is complex, (two or more detections within $2\farcs0$ in the same band in the same epoch) the grade is 'K', overriding the above grade. The detection itself may be of high quality. Non-detections that are outside of the coverage in a band or within 2 pixels of the edge of the mosaic are given a grade of 'N'. Bandfill sources will have the regular 'A-E' quality of detection except for faint ones, which will have quality 'U', denoting an upper limit (see § 2.4.4). Thus, only the imtype tells you that the flux is bandfilled.

For MIPS2 detections, we have employed some additional grades to specify how well the MIPS2 data are matched with shorter wavelength detections. In the table below, the term "catalog source" means a source in the catalog **before** inclusion of the MIPS2 data.

| Grade | Description |
|---|---|
| A-E | MIPS2 detection was only matched with one catalog source within 8 arcseconds. These are the same as the S/N grades above. |
| P | There were multiple catalog detections near this MIPS2 source. The MIPS2 was matched with the catalog source that gave the most "consistent" SED, and that catalog source was the one closest to the MIPS2 detection. |
| S | There were multiple catalog detections near this MIPS2 source. The MIPS2 source was matched with the catalog source that gave the most "consistent" SED, and that catalog source was NOT the one closest to the MIPS2 detection. |
| W | There were multiple catalog detections near this MIPS2 source. It was not clear which catalog source gave the "best" SED, so the MIPS2 source was matched with the nearest catalog source. |
| Y | There was a nearby MIPS2 detection for this catalog source. However, it "lost out" because that MIPS2 detection was better matched with a different catalog source. This grade is used to allow one to find other nearby catalog sources that may be contributing flux at 70 microns. |

**Flag 2:** Quality of the Flux

This is listed in the catalog as XX_Q_flux_m, where XX is the band name and can be one of 'IR1', 'IR2', 'IR3', 'IR4' for IRAC bands 1-4, 'MP1' or 'MP2' for MIPS bands 1-2, or 'J','H', 'Ks' for the 2MASS bands.

This flag is a measure of how similar the fluxes are between two epochs of observation. It is computed by the following:

$$\frac{|Flux(epoch1) - Flux(epoch2)|}{(\delta_{flux}(epoch1)^2 + \delta_{flux}(epoch2)^2)^{0.5}}, \quad (1)$$

where $\delta_{flux}$ is the uncertainty in the flux value. A letter grade is assigned based upon how far the quotient is away from zero, as follows:

| Quotient | Grade |
|---|---|
| $\leq 2$ | A |
| $\leq 4$ | B |
| $\leq 6$ | C |
| $\leq 8$ | D |
| $> 8$ | E |

If no ratio is computed because there is only one epoch of observations (or because a source was only detected in one epoch), the grade is 'Q'.

**Flag 3:** Quality of the Position

This flag is listed in the catalog as Q_pos, with one value for each bandmerged source.

After bandmerging, there will be a number of sources with detections in more than one band or epoch. The weighted average RA and DEC is used as the reference position and a distance between that position and all detections with quality of 'A' or 'B' is computed. This distance is scaled relative to the beam width for each band. The grade is assigned based upon the number of beam widths the furthest detection is away from the weighted average position or 0.6 arcseconds, whichever is larger.

| Beam Width or distance | Grade |
|---|---|
| $\leq 1/4$ or $0.6''$ | A |
| $\leq 1/2$ or $0.6''$ | B |
| $\leq 3/4$ or $0.6''$ | C |
| otherwise | D |

If a source is only detected in one band, or only one band has detections of 'A' or 'B' quality, the quality of position grade is 'Q'.

**Flag 4:** Overall Quality of the Source

This flag is listed in the catalog as Q_merge, with one value for each bandmerged source.

Using the other grades, an overall quality for each source is assigned. The listed criteria for a given grade must all be met to assign that grade.

| Grade | Criteria |
|---|---|
| A | Quality of Position = A |
| | Quality of detection is A or B in at least 2 bands |
| | Quality of flux is A or B in at least 2 bands |
| B | Quality of Position A or B |
| | Quality of detection is A or B in at least 1 band |
| | Quality of detection is A, B, or C in at least 1 other band |
| | Quality of flux is A or B in at least 1 band |
| | Quality of flux is A, B, or C in at least 1 other band |
| C | Quality of Position A, B, C, or Q |
| | Quality of detection is A or B in at least 1 band |
| | OR |
| | Quality of detection is A, B, or C in at least 2 bands |
| D | All others |

### *2.4.6. Source Spectral Index*

For sources with adequate information, a spectral index ($\alpha$) was fit to bands from K-band to MIPS1 (2 to 24 microns), as available. The resulting values are listed in the catalog file (§3.2). The definition of $\alpha$ is:

$$\alpha = \frac{dlog(\lambda F(\lambda))}{dlog(\lambda)} \tag{2}$$

where $\lambda$ is the wavelength and F($\lambda$) is the flux at that wavelength.

We obtain $\alpha$ from a linear fit to the logarithms. The uncertainty of $\alpha$, the reduced $\chi^2$, and the number of bands used for the linear fit are listed in the table. The uncertainty is calculated by propagating the uncertainties in the fluxes of the bands. Thus, an uncertainty is available even for 2-band detections, while a $\chi^2$ value is available only for sources with detections in at least 3 bands. The mean value of $\alpha$ for objects that are background stars with $A_V < 5$ is $-2.8$, in agreement with that expected for an average over stellar spectral types. The uncertainty in $\alpha$ is much less if all bands are available for the fit. If there is inadequate information to compute $\alpha$, a value of $-999$ is assigned.

## 2.5. Source Classifications

The source classification is done with the Full Catalog and is propagated to the more restrictive catalogs (see Table 1).

The main goal of the source classifications is to begin the process of separating candidates for young stellar or substellar objects of any class (which we denote collectively as YSOs) from background galaxies and other objects. In pursuing this goal, we have generally taken a conservative approach, putting objects in other categories first, based on their spectral energy distribution (SED). However, we do allow sources with certain SED types assigned earlier to become YSO candidates (YSOc) if they meet other criteria. We use only the SED information from J band to MIPS1. The near-infrared data (J, H, and $K_s$) come from 2MASS, which is not deep enough to see many of the sources detected by IRAC. We do not use the MIPS2 data in the main source SED classification, but they are used in a minor way for further classification of the type of YSOc.

While calibration uncertainties (§3.5.2; Table 21) are not included in the uncertainties in the catalog, they are added in quadrature for the purposes of classification.

The main types of objects in the catalog are main sequence stars, galaxies, and YSOs. The majority of asteroids have been removed in the mosaicing process by the outlier rejection module of MOPEX based on two epoch observation, but some will remain, especially weaker ones. Note that 38 of the 84 cores, and all of the stars, were observed in only one epoch, so asteroids will not

be removed in those data (see Table 2). However, the cores observed in only one epoch were those at high ecliptic latitude, so asteroid contamination is not a concern for these cores.

We assign an "object type" for each source in the catalogs based on the properties of the SEDs. Data used for source classifications are: 2MASS J, H, and $K_s$ fluxes, Spitzer IRAC1-4 fluxes, and MIPS1 flux. The MIPS2 flux is used only during YSO classification. Table 13 lists the object types and gives a brief description of their properties. Each source is assigned one and only one object type based on a sequential sorting and fitting. Figure 6 shows the flow sequence used in classifying sources into each object type. Figure 7 shows typical SEDs for each object type. The major steps of our procedure are:

1. identify and set aside sources with detections at two or fewer wavelengths and also 2MASS-only sources
2. identify likely background and foreground stars
3. select sources that fit three specific templates
4. select YSO and galaxy candidates based on color-magnitude criteria
5. for the remaining sources, assign object types according to SED morphology (this category probably contains many galaxies)

The details for each step and the exact criteria for selecting each object type are described in the following sections. In all cases, SED fitting only considers the combined epochs data for any band. If the detection in the combined epochs has quality 'U' (upper limit) or 'N' (not observed), the band will not used for SED fitting.

### *2.5.1. Find Sources with Limited Information*

We first identify sources without enough information for classification. Three types of sources are identified according to the following rules:

- Zero: Sources that do not have a detection in the combined epochs data for any of the J-MIPS2 wavelengths. They have been detected only in one (or possibly both) of the two epochs acquired by c2d, but not in the combined epochs data.
- 2mass: Source detected in only 2MASS bands (J, H, and Ks) and not detected in any Spitzer bands. In general, nearly all 2MASS sources are detected in the IRAC1 band when IRAC1 is present. Sources selected as "2mass" are mostly located in the regions only observed with MIPS. The majority of these sources should be stars.

- one: Source detected in only one band from IRAC1 to IRAC3 band with no 2MASS detection and no detection beyond IRAC3 band. The majority of these sources are weak IRAC1 detections. MIPS2-only detections also fall into this category.
- two: Source detected in only two bands from the J to MIPS1 bands with at least one of the detections in a Spitzer band, excluding sources with detections only in IRAC4 and MIPS1.
- red1: Source detected in only the IRAC4 or MIPS1 band. They are separated from the other one band detection ("one"), because they could be interesting sources with rising SEDs which are too faint to be detected in the IRAC1-3 bands.
- red2: Source detected in both IRAC4 and MIPS1 and no other Spitzer bands or 2MASS bands. These sources are potentially interesting due to their rising SED's.

All objects with detections in at least 3 bands are subjected to the selection procedure in the following sub-sections. 2MASS-only sources have a best-fit $A_V$ determined from the procedure in § 2.5.2 but are still classified as '2mass' in the catalog.

### *2.5.2. Identify Stars and Estimate Line-of-Sight Extinctions*

We identify main sequence or giant stars (classified as "star") if their SEDs can be well-fitted by a reddened stellar photosphere. It is important to include the effect of the dust extinction for identifying stars. The observed flux of a reddened star at a particular wavelength $\lambda$, $F_{obs}(\lambda)$, can be described with the following equation:

$$\log(F_{obs}(\lambda)/F_{model}(\lambda)) = \log(K) - 0.4 \times C_{ext}(\lambda) \times A_V \quad (3)$$

where $F_{model}(\lambda)$ is the stellar photosphere model, $K$ is the scaling factor of the model for a particular star, and $C_{ext}(\lambda) = A_\lambda/A_V$ is the ratio of $\lambda$ to visual extinction from the dust extinction law. The values of $K$ and $A_V$ are derived from the linear fit of this equation to the measurements given assumed stellar photosphere and dust extinction models. The fit also generates a $\chi^2$ measure of the residual to the fit which can be used to judge the goodness of fit to the stellar model. The best-fit, unextincted IRAC1 flux is simply $K \times F_{model}$.

We adopt the dust extinction model from Weingartner & Draine (2001) with $R_V = 5.5$, which gives a good description of the extinction in the typical region of our maps. The stellar photosphere model used for selecting stars was compiled from two references. For K to MIPS1 bands, we adopt the models from SSC's "Star-Pet" tool, which is based on the Kurucz-Lejeune models (http://ssc.spitzer.caltech.edu/tools/starpet). For the 2MASS bands, we translated the observed J–H and H–K colors of stars (Koornneef 1983) to fluxes relative to K band. We did not correct for the difference between K and Ks bands.

Sources were *not* assigned to the "star" category if there was a 10% or smaller probability that the fitted $\chi^2$ was consistent with an extincted stellar template. All sources with good fits were labeled "star". In order to allow identification of some types of evolved stars (which may have strong atmospheric absorption features) as stars, fits were done ignoring one band from the fit; the fits were done with each band dropped one at a time. The same 10% $\chi^2$ probability criterion was applied to these fits with again the rejected sources moving on to be considered for classification in the non-star categories. However, if the observed flux of the last detected band of a source is greater than 3 $\sigma$ plus the expected stellar flux, this source will not be categorized as "star"; it will be categorized as "star+dust" (see the next section).

The fitted line-of-sight extinctions toward stars are listed in the catalogs. These extinctions may include slight offsets, $A_V$ = 1–2, introduced by the fitting process and systematic uncertainty in the intrinsic colors of stars (see §3.7.1). Alternatively, these offsets may be at least partially attributed to extinction from the diffuse interstellar medium rather than the molecular cloud itself.

### *2.5.3. Fit specific templates*

We have utilized three non-stellar SED templates to create categories within the sources that are not identified as stars. The goal of these classifications is to create categories that are strongly enriched in certain types of objects, recognizing that there are overlapping characteristics which preclude any of the categories from being uniquely linked to a simple object type.

First, sources with [3.6]−[4.5]<0.6 and 1.5<[5.8]−[8.0] are identified with the type "PAH-em" which stands for PAH emission feature. The above color criteria select for extra-galactic objects which have stellar and dust emission and prominent PAH emission in the IRAC4 band. The first color criteria represents a stellar component; the second color criteria ensures a sharp increase of flux from IRAC3 to IRAC4 band, as expected if PAHs emission is strong. These features can also be present in Class II YSOs but no current YSO models occupy this region in [3.6]−[4.5] vs. [5.8]−[8.0] color-color diagram (see Allen et al. 2004). However, it is not clear that YSOs would not produce similar PAH emission features, since most of the models do not include PAHs.

The second SED template is the combination of a stellar and a dust component, which we label as "star+dust(BAND)" where BAND is IR1, IR2, IR3, IR4, or MP1, representing the Spitzer band at which the dust component is greater than a 3 $\sigma$ excess over the fitted stellar flux. This SED type is commonly seen in both Class II YSO and background galaxies. We use the method described in the "star" section to select sources whose SED's are well-fitted by a reddened stellar photosphere for at least 3 bands starting at the shortest wavelengths. If, starting at the specified longer wavelength band, the difference between observed flux and the expected reddened stellar flux satisfies both $F(\lambda)_{obs} - F(\lambda, A_V)_{star} > 3\ \sigma$ for $\lambda = \lambda(BAND)$ and $F(\lambda) - F(\lambda, A_V)_{star} > 2\ \sigma$ for $\lambda > \lambda(BAND)$ , the source is labeled as "star+dust(BAND)".

The third SED template selects for a large MIPS1 to IRAC flux ratio, which we labeled as

"red". This feature suggest a dominant dust component in the SEDs, a preferred feature for Class 0/I objects; however, this feature can also be seen in some galaxies. The criteria for "red" is that the MIPS1 flux is greater than 3 times the flux from the nearest IRAC band.

Note that these 3 SED templates are not exclusive from each other; some sources may satisfy 2 or 3 templates. However, we only label a source with one type. The selection sequence is PAH-em, star+dust, then red.

### *2.5.4. Select YSO candidates*

YSO candidates are traditionally selected as sources with flux excess at near-infrared to far-infrared wavelengths compared to the stellar photosphere. Unfortunately, many background galaxies fit the same description. Because our observation is deep enough to have significant galaxy contamination, we have chosen to make a relatively pure YSO candidate sample by discriminating against galaxies using color-magnitude criteria derived from the SWIRE data, which presumably contain only stars and galaxies (Lonsdale et al. 2003). We reprocessed SWIRE data with our data reduction pipeline to provide a control sample that was processed in the same way as our source samples (§3.8).

The procedure we use to select YSO's and de-select extra-galactic background sources is based on the color-magnitude diagrams shown in figure 10. We construct "probability" functions for each of the three color-magnitude diagrams based on where a source falls relative to the black dashed lines in each diagram. These three "probabilities" are multiplied and then additional adjustments to the probability are made based on several additional properties of the source fluxes and whether or not they were found to be larger than point-like in the source extraction process. The final probability is unnormalized but is related to the probability that the object is a galaxy. Thus a YSOc must have a **low** value for the probability.

As a first cut to the data, before applying any of the following criteria, we required sources to be detected in all four IRAC bands and in the MIPS1 band with quality of detection A,B,C, or K. As with SED fitting, we only considered detections in the combined epochs of observation. Sources that do not meet this pre-selection criterion are not classified as either YSO or extra-galactic candidates.

In the [4.5] vs. [4.5]-[8.0] color magnitude diagram, the probability function is given by the following, where "i2" refers to IRAC band 2, etc.:

$$P_{i2i4} = 0.7 \times [1 - exp(-[1.2 + 0.5(M_{4.5} - D)]^3)]$$

where:

$D$ = 13.05 for $M_{4.5} - M_{8.0} > 1.4$

= 14.5 for $0.5 \leq M_{4.5} - M_{8.0} < 1.4$ and object was found to be pointlike at 3.6 and 4.5 $\mu$m

= 12.5 for $0.5 \leq M_{4.5} - M_{8.0} < 1.4$ and object was found to be extended at 3.6 or 4.5 $\mu$m

= 14.5 for $M_{4.5} - M_{8.0} < 0.5$

By 'extended', we mean the imtype for that wavelength equals 2 (§11). By 'pointlike', we mean that the source does *not* have imtype=2.

The minimum value for $P_{i2i4}$ is zero, except for cases where $M_{8.0} > 10.5$ and $P_{i2i4} < 0.1$, when the minimum is set to 0.1.

In the [24] vs. [8.0]-[24] color magnitude diagram, the probability function is:

$$P_{i4m1} = exp(-\{[(M_8 - M_{24} - 3.5)/1.7]^2 + [(M_{24} - 9)/2]^2\})$$

and $P_{i4-m1}$ is set to a minimum of 0.1.

In the [24] vs. [4.5]-[8.0] color magnitude diagram, the probability function is:

$$P_{i24m1} = 0.7 \times \{1 - exp[-(M_{4.5} - M_8 + 0.8) - (10 - M_{24})/1.8]\}$$

and $P_{i24m1}$ is set to a minimum of 0.

The combined "probability" is then: $P_{tot} = P_{i2i4} \times P_{i4m1} \times P_{i24m1}$. Additionally, the following factors influence the value of $P_{tot}$ and are applied in the order given:

$P_{tot}$ = 0.1 for sources with $M_{24} > 10$

= $2 \times P_{tot}$ for sources that are extended at 3.6 or 4.5$\mu$m

= $P_{tot}/(K_s - M_{4.5})$ for sources with 2MASS $K_s$ quality of A, B, or C.
If $K_s - M_{4.5} < 0.2$, then divide $P_{tot}$ by 0.2

= $0.1 \times P_{tot}$ when $F_{70} > 400$ mJy and the source is detected at 5.8, 8, and 24 $\mu$m

= $2.0 \times P_{tot}$ if $M_{3.6} - M_{4.5} < 0.2$ and $M_{5.8} - M_{8.0} < 0.2$

Finally, a minimum value of $10^{-5}$ is assigned to $P_{tot}$ for convenience in plotting on logarithmic plots. Based on the distribution of $P_{tot}$ shown in figure 11, we chose the dividing line between YSO's and extra-galactic sources to be $\log_{10}(P_{tot}) = -1.47$ or $P_{tot} \approx 0.0339$. The final $P_{tot}$ values are also listed in the catalogs in the column 'Log(Prob_Galc)' and identified as "non-normalized probabilities" in the data dictionary. Those sources with $\log_{10}(P_{tot}) \geq -1.47$ are designated galaxy candidates 'Galc', while those less than the limit are 'YSOc' for YSO candidates. These names are prepended to the objects classified in § 2.5.3. Objects not already classified as a particular type of object are given the simple classification 'YSOc' or 'Galc'.

### *2.5.5. Assign SED morphologies*

The remaining sources, which are not categorized by the above selection criteria, are mostly faint and detected in a limited number of bands. We assign an object type to these sources according to their SED morphologies by approximating the SEDs by second order curves. Hence, each source must have one of the 5 possible morphology types: rising, falling, flat, cup-up (concave), and cup-down (convex).

The SED morphology of each source is determined according to the following operations. We first divide the SED of each source into 3 sections – left, center, and right, from short to long wavelengths, then compare the average flux of each section. The bands included in each section depend on the total number of bands with detections. If the source is detected in 3–5 bands, the left and right section each contains one band at either end of its SED and the central section contains the remainder bands. If the source is detected in 6 or 7 bands, the left and right section each contains two bands and the central section contains 2 or 3 bands. If the source is detected in all 8 bands from J to MIPS1, the left section contains 3 2MASS bands, the central section contains IRAC1 and IRAC2 bands, and the right section contains IRAC4 and MIPS1 bands. We calculate the average flux of 3 sections, F(left), F(center), and F(right), and the object type is assigned according to the following rules:

- rising: F(left)−F(center) $< -2\sigma$ and F(right)− F(center) $> 2\sigma$
- falling: F(left)−F(center) $> 2\sigma$ and F(right)− F(center) $< -2\sigma$
- flat: $-2\sigma <$ ( ( F(left)+ F(right) )/2 − F(center) ) $< 2\sigma$
- cup-up: ( F(left)+F(right) ) / 2 − F(center) $> 2\sigma$
- cup-down: ( F(left)+F(right) ) / 2 − F(center) $< -2\sigma$

## 3. Description of Data Products

The products in this delivery are summarized in Table 1 and described briefly below, with the sections of this document containing more information indicated:

1. Mosaic images of the intensity, the uncertainty, and the coverage in IRAC and MIPS for each core, wTTS, or cloud area (§3.1). In addition, for the two largest clouds, Perseus and Ophiuchus, we are also delivering mosaics (intensity only) of the entire cloud area in addition to the sub-regions used for practical computer processing during the source extraction phases (see Tables 4 and 5).

2. For each delivered cloud, core, or wTTS region, we deliver the following catalogs (§3.2)

- The Full Catalog of all sources extracted and bandfilled, including 70 $\mu$m fluxes and merged with 2MASS catalogs. These can contain sources seen only with 2MASS. Sources will be classified as described in §2.5. These catalogs may contain over 1 million entries. Be well armed before entering this territory.
- The High Reliability Catalog. These are more similar to our previous catalogs in that sources must meet certain quality criteria, explained in §3.2. These catalogs may contain up to 200,000 sources.
- The YSOc catalog. These catalogs include all sources from the Full Catalog that are classified as YSO candidates, using the criteria described in §2.5. If no sources meet these criteria, this catalog will not exist.

3. A quality file for each cloud, core, or wTTS region (§3.3). The quality files tell the user where the data can be found for wTTS that used cloud data for either IRAC or MIPS.

4. For each of the large clouds, we provide images showing the extinction derived from background stars, smoothed to a variety of different beams (§3.7).

5. For each cloud, we deliver the same catalogs described in item 2 from the extincted, resampled ELAIS-N1 field of the SWIRE survey (§3.8). These are **degraded** versions of the SWIRE data and should not be used for any extra-galactic project. They are intended for use in further exploration of methods for separating YSOs from galaxies. There are six of these, with different random resamplings, after being extincted to match the extinction distribution, for each of our clouds.

6. For the ensemble of clouds and for the ensemble of cores, we provide a catalog of all the YSOc objects.

7. For Perseus, Ophiuchus, and Serpens, there is a catalog of cores found at 1 mm in Bolocam maps, with identifications in the c2d catalogs (§3.2.3).

8. For Perseus, there is a catalog of transient sources (§3.2.4).

### 3.1. Description of Images

We are delivering mosaic images for IRAC and MIPS data. As described earlier, we have included in this delivery both uncertainty and coverage mosaics in addition to the basic image mosaics. The uncertainty mosaics show the estimated uncertainty for each image pixel based on the combined uncertainties of the BCD pixels contributing to that mosaic pixel. Likewise the coverage maps show the effective number of BCD pixels that actually contributed to that final image mosaic pixel. Furthermore, for the two largest clouds, Perseus and Ophiuchus, we have constructed full-cloud image mosaics that combine the several sub-regions used for practical computer processing. Note that there are no corresponding coverage/uncertainty mosaics for these full-cloud images.

The geometry of the mosaics constructed with Mopex for this paper was such that we kept a 1:1 pixel size ratio between the basic instrument pixel size and mosaic pixel size, and we assembled the BCD images in a coordinate system essentially fixed with respect to the average instrument rotation projected on the sky. The area included in the mosaics for IRAC was just the area covered by all four bands; for MIPS we included only "on-source" pointings, i.e., not pointings where the band in question was not the prime observer. IRAC and MIPS images will have different sizes (and, in some cases, orientations) because of the detailed data taking methods. The IRAC images will overlap with one another except near edges where the dither patterns produce slightly different coverage. For IRAC images where HDR data were available, we deliver both the mosaics without ("A") and with ("COMB") the HDR data added in.

The most significant problems that can be found in the mosaics are: (1) not fully corrected muxbleed and sometimes column pulldown in IRAC images; (2) incorrect fluxes for saturated stars; (3) latent images, particularly for bright stars in MIPS 24 images; (4) some residual "jail-barring" in MIPS 24 images that we were not able to remove completely, as well as diffraction patterns that include features resembling compact sources; (5) a few examples of straylight/reflections due to bright stars; and (6) probably a very small number of some low level cosmic ray hits that were not detected by Mopex's outlier detection because they were too close to the noise level.

The previous discussion pertains to the IRAC and MIPS 24 $\mu$m images. For MIPS 70 $\mu$m data, we deliver mosaics made with the unfiltered data and the filtered data. For MIPS 160 $\mu$m data, we deliver only mosaics made with unfiltered data. Data from both epochs were combined if there were two. They have square pixel sizes of 4 arcsec and 16 arcsec, for 70 and 160 $\mu$m, respectively. These are roughly 0.5 and 1.0 times the BCD pixel sizes. Mopex was allowed to choose the optimum orientation.

The most significant problem with the 70 and 160 $\mu$m BCD mosaics is response variations in the detectors leading to striped patterns along the scan direction, most noticeable on the 70 $\mu$m BCD mosaics, where they are at the few times 10% level. According to the MIPS Data Handbook, point-source (and moderately extended-source) fluxes from the mosaics should be reliable as the response variations affect the background, which can be subtracted out in photometry or by filtering. The SSC's time-filtered and spatial-filtered products remove background. The accuracy of plain BCD mosaic intensities for broad extended dust emission has not been characterized at this time.

Occasionally, broad, weak, bright stripes in the cross-scan direction can be seen on the 70 $\mu$m BCD cloud mosaics. These are due to stimulator-flash latent emission. This is additive and will not affect photometry. Bright sources can distort the response calibration for a pixel. This is most easily seen on the 160 $\mu$m mosaics as a trail of bright or dark spots in the scan direction. Regions where the 70 and 160 $\mu$m detectors saturated on either cloud dust emission or bright sources are also present and identifiable by eye.

### *3.1.1. Using DS9 to Display the Images*

Many astronomers use SAOImage DS9 to display images[2]. When using DS9 to display composite images using our delivered mosaics, often there *appears* to be an astrometric offset of sources at different wavebands. This problem is typically not apparent in composites of only IRAC mosaics, but appears when constructing composites using both IRAC and MIPS mosaics as shown in Figure 12. We stress that this problem is not with the registration of our mosaics; the astrometry information in the mosaic headers and the coordinates of sources listed in our catalogs is correct. For DS9 to properly display the mosaics in a composite image, the mosaics should be processed with the *remap* utility in the WCSTools package (e.g., Mink 1999) [3]. As an example, to display a composite image of the IRAC1, IRAC2, and MIPS1 mosaics of Serpens, we would "remap" the IRAC2 and MIPS1 mosaics using the IRAC1 mosaic as a reference in the following way:

```
remap -f SER_COMB_IRAC1_mosaic.fits -o
  remapped_SER_COMB_IRAC2_mosaic.fits SER_COMB_IRAC2_mosaic.fits
remap -f SER_COMB_IRAC1_mosaic.fits -o
  remapped_SER_A_MIPS1_mosaic.fits SER_A_MIPS1_mosaic.fits
```

Then, the delivered IRAC1 mosaic, along with the remapped IRAC2 and MIPS1 mosaics, may be used within DS9 to properly construct the composite image shown in Figure 12. **We do not recommend using remapped mosaics to obtain any quantitative scientific results; rather, we suggest that they be used only for display purposes, if necessary.**

## 3.2. Catalogs of Sources

We are delivering the Full Catalog, which contains every extracted source. Other catalogs, such as the High Reliability catalog and the YSOc catalog, are derived from the Full Catalog. The High Reliability catalog includes only sources meeting certain criteria. The YSOc catalog attempts to select against most background galaxies. Specialty catalogs (Table 1) are described in later sections.

For the Full and High Reliability Catalogs, sources outside of the mapped area of one or more bands, or only observed in one epoch, are included. As noted earlier, the sensitivity of IRAC observations is not uniform across the clouds (and some cores that required that observations be done with mosaic mode) because the overlap regions are observed with double observing time. In

[2]Information about DS9 and downloading this application is available at http://hea-www.harvard.edu/RD/ ds9/

[3]Information about WCSTools and downloading this package is available at http://tdc-www.harvard.edu/software/wcstools/

addition, regions with GTO data may have deeper integrations in some cases. However, the sensitivity of MIPS observations is relatively uniform across the large clouds because the observations were done in scan mode. Source extractions for the cores and stars were $\sim 3$ times deeper than our standard extraction depth. The catalogs are in IPAC table format. For ease of use, all catalogs have the same number of columns. These columns are discussed below and listed in Table 16.

Catalog positions and uncertainties make use of data from all bands and, where appropriate, from more than one epoch of observations, as described in §2.4. Quality flags indicate an assessment of agreement in the merging of positions and fluxes. Simple derivative classifications are also compiled, including the index of a power law fit to available bands from 2 to 24 $\mu$m and the object type defined in §2.5.

For some purposes, it is important to know if a flux was extracted in the first round of source extractions or whether it results from bandfilling. If the flux comes from bandfilling, that flux value will have an imtype of $-2$ (see Table 11).

It is also important to check the imtype flags for any 70 $\mu$m fluxes as many of these are problematic because of saturation or extended source structure (See Table 12).

**Source-Dependent Parameters**

There is one set of these parameters for each source, even if detected in multiple bands. Source-dependent columns in the table include source name, coordinates, quality flags, power-law indices fit to IRAC fluxes (§2.4), and object type (§2.5). These are specified in Table 14.

**Band-Dependent Parameters**

Columns that follow the source-dependent listings within the catalog table contain parameter values associated with individual Spitzer bands. These include fluxes, uncertainties, dates of observation, quality flags, and an image type (Table 11) from the source extraction (see Section 2.3). The list of column names and data types for a single band is compiled in Table 15.

**Index of Column Headers**

In Table 16, we give the complete list of column headers for the delivery catalogs, with references to the sections or tables where they are discussed. For consistency across the Spitzer wavelengths, we have left in columns of data that are empty in the catalog. These are identified in Table 16 as 'Not used'. The unused columns occur only in the MIPS2 waveband.

### *3.2.1. High Reliability Catalog*

The High Reliability catalog is derived from the Full catalog. It includes those sources within fields covered by at least two IRAC bands and MIPS1 that were detected with at least one detection quality of A and a second detection quality of A or B in Spitzer IRAC and MIPS1 bands. Also, sources within fields covered by MIPS1 but not covered by any IRAC band that have MIPS1

detection qualities of A are included in the High Reliability catalog.

### *3.2.2. YSOc Catalog*

The catalog of candidates for YSO (Young Stellar or Substellar Object) status is derived from the Full Catalog, using the criteria described in §2.5. The YSOc catalog requires SNR $\geq 3$ in IRAC1-4 and MIPS1 (see §2.5 for more precise statements). This catalog also includes YSOc that attain that status only after bandfilling, as well as those that were classified as YSOc even without bandfilling. While the bandfilling process has captured some legitimate YSOs, it has also added some specious sources. These are often caused by bandfilling a flux that is actually the wing or a diffraction spike from a nearby, brighter source. YSOc's with bandfilled fluxes (an imtype of $-2$) should be viewed with some skepticism. The user is encouraged to examine all of these by eye.

One should also note that these criteria were developed for the case of Serpens, which has very crowded fields of YSOs, has a high density of background stars, and is more distant (260 pc) than most of the other clouds. It is quite likely that these criteria could be tuned for better results in other clouds.

We have made comparisons to more detailed analyses done with less restricted samples and using eye examination and/or data from other wavelengths for the cases of Serpens (Harvey et al. 2007b) and Cha II (Alcalá et al. 2007). We will discuss Serpens first and then Cha II.

For Serpens, the YSOc catalog contains 262 YSOc, of which 231 are in the eye-checked list of 235 by Harvey et al. (2007b) and 31 are missing from that list. The four sources included by Harvey et al. (2007b) but missing from our catalog include one source that lacked sufficient information for the automated system, but appears to driving an outflow and three sources that are too saturated at 24 $\mu$m to have good fluxes in the catalog. Thus our catalogs will miss some of the strong, obvious sources, most of which will be known from previous work.

We will refer to the 31 sources in the catalog that are not in Harvey et al. as "fake" YSOc, though we don't know that for all of them. Four of these are very strong sources and are identified as AGB stars in Figure 3 of Harvey et al. (2007b). Many of the rest look like stars except for excess emission only at 24 $\mu$m; 14 are classified as "YSOc_star+dust(MP1)". These were rejected by Harvey et al. because the MIPS1 flux was contaminated by emission from a stronger, nearby source. Almost all of these were bandfilled at 24 $\mu$m.

The second largest group of "fake" sources were YSOc_red; these were distinguished by very sudden increases of flux, with ratios of flux at 24 $\mu$m to flux at 8 $\mu$m ranging from 7 to over 400. All of these were bandfilled at 24 $\mu$m.

One might hope that these "fake" sources would have $\log_{10}$Prob_Galc near the cutoff value for YSOc at $-1.47$. Indeed, 11 lie near this cutoff with $\log_{10}$Prob_Galc$> -2.3$, but 20 have the minimum value of $-5$. Their distribution over the classes defined by $\alpha$ was similar to that of the

verified sources.

The best method for finding suspect sources is to check if they become YSOc on the basis of bandfilled fluxes at long wavelengths. These should then receive particular scrutiny on the images because the bandfilling may well have picked up emission from a nearby, stronger source. Recall that one can learn if a flux has been bandfilled by examining the *imtype* flag for that band (see Table 11).

We can also compare the results, using the same criteria developed for Serpens, in the case of Cha II, which is closer (178 pc) and has much lower surface densities of both YSOc and background stars. For Cha II, where we have complementary optical data, 29 YSOc appear in the catalog. All of the 24 previously known YSOs are found in our YSOc catalog. Of the 5 new candidates, 2 are clearly galaxies based on optical images, 1 can be rejected based on 24 $\mu$m confusion, and 2 are possible new YSOs. Details will be given by Alcalá et al. (2007). These results are far more satisfactory than those based on the previous (2005) delivery, as disussed by Porras et al. (2007).

### *3.2.3. Catalog of Millimeter Sources*

The MM Source Catalog tabulates sources detected in Bolocam 1.1 mm surveys of Perseus (Enoch et al. 2006), Serpens (Enoch et al. 2007), and Ophiuchus (Young et al. 2006). The millimeter maps cover 7.5, 1.5, and 10.8 square degrees, respectively. The catalogs are in IPAC format, and the explanation of all the columns is given in Table 17. They contain all sources detected above 5 times the rms noise in Perseus and Serpens, and 4 times the rms noise in Ophiuchus. Coverage is fairly uniform in the maps, and the uncertainty in the peak flux density is equivalent to the local rms noise value.

The peak flux density per beam ($I_\nu$) is given in mJy beam$^{-1}$ (1 mJy beam$^{-1}$ = 0.04 MJy sr$^{-1}$). The uncertainty in the peak flux density is the local rms beam$^{-1}$ and does not include an additional 15% systematic uncertainty from calibration uncertainties and residual errors after iterative mapping. Integrated flux densities in apertures of FWHM 40″, 80″, and 120″ are given, as well as the total flux density. No integrated flux density is given if the distance to the nearest neighboring source is smaller than the aperture diameter. The total flux density is integrated in the largest aperture (30″ – 120″ diameters in steps of 10″) that is smaller than the distance to the nearest neighboring source. Uncertainties in the flux are $\sigma_{ap} = \sigma_{mb}\sqrt{\theta_{ap}/\theta_{mb}}$, where $\sigma_{mb}$ is the local rms beam$^{-1}$ and ($\theta_{ap}$, $\theta_{mb}$) are the aperture and beam FWHM respectively, and do not include an additional 15% systematic uncertainty.

FWHM and PAs are from an elliptical gaussian fit; the PA of the major axis is measured in degrees east of north. Uncertainties for the FWHM and PA are formal fitting errors from the elliptical gaussian fit; additional uncertainties of 10 – 15% apply to the FWHM, and $\sim 5°$ to the PA (determined from simulations). The morphology keywords indicate whether the source is multiple (within 3′ of another source), extended (major axis FW at $2\sigma > 1'$), elongated (axis ratio

at $4\sigma > 1.2$), round (axis ratio at $4\sigma < 1.2$), or weak (peak flux density less than 5 times the RMS pixel$^{-1}$ in the unfiltered map).

Masses are calculated according to Eq. 3 of Enoch et al. (2006) using the total flux density assuming a single dust temperature of $T_D = 10K$ and a dust opacity at 1.1mm of $\kappa_{1.1mm} = 0.0114\,\mathrm{cm^2 g^{-1}}$. Uncertainties for masses are from photometry only, and do not include uncertainties arising from uncertainties in the dust opacity, dust temperature, or distance, each of which can contribute up to a factor of a few or more. Peak $A_V$ is calculated from the peak flux density as described in Enoch et al. (2007). The mean particle density is calculated from the total mass and the deconvolved average FWHM size, assuming spherical sources.

A 1.1 mm source is considered coincident with a Spitzer YSO source if the 1.1 mm position is within 50″ of a YSO candidate from the c2d catalog (e.g., Harvey et al., 2006). The SSTc2d positions/IDs of associated Spitzer YSO candidates are given. If more than one YSO candidate lies within 50″ of the 1.1 mm position, the "Spitzer_YSO" category is designated "multiple", and the SSTc2d ID of the closest YSO candidate is listed.

### *3.2.4. Catalog of Transient Sources*

Mapping of large clouds and cores at low ecliptic latitude was done in two separate observation epochs separated by 3-6 hours. Transient sources are those with robust detections at one epoch but not at the other epoch. Instrumental artifacts, such as latent images, will also produce transient sources in the c2d catalogs. However, the bulk of the transient sources are expected to be main-belt asteroids, whose expected motions will lead to position shifts of 0.5-5 arcmin between epochs. Given the color temperatures of main-belt asteroids (160-220 K), the relative sensitivities of the IRAC and MIPS channels, and the fact that c2d is a shallow survey, significant numbers of asteroid detections are expected only in IRAC channel 4 and MIPS channel 1 (wavelengths of 8.0 and 24.0 $\mu$m, respectively). In practice the vast majority of asteroids are detected in only a single band, due to the fact that the IRAC and MIPS observations of a particular target were taken in different instrument campaigns separated by days or weeks.

A transient catalog has been developed for the Perseus molecular cloud region mapped by MIPS (ecliptic latitude 12°; map area 10 square degrees). Improved calibrated data, as described in section 2.2.1, was input to the SSC MOPEX software to create separate mosaics of the Perseus field at each of the two epochs. Single mosaics of the entire field were too large for the memory of the available workstation, so the Perseus field was broken up into three subregions. A crucial step in the mosaicing process was to build the second epoch mosaic such that its world coordinate system was *identical* to that of the first epoch. This was done using the to the Fiducial Image Frame (FIF) table in MOPEX. The results were image mosaics where a fixed pixel X,Y corresponded to the exact same position and sky area at both epochs. Taking the difference of the two mosaic images causes all the fixed objects in the field to subtract out, leaving only positive and negative transient

sources which can then be extracted.

Two transient catalogs were extracted from the Perseus 24 $\mu$m mosaics, one for each observation epoch. These were produced using the IDL Xstarfinder procedures. The initial versions of these catalogs contained approximately 6000 sources each, down to a flux density 0.8 mJy. Visual inspections found that sources fainter than 1.6 mJy were primarily noise fluctuations in the maps. As a result, the delivered catalogs are restricted to sources brighter than this flux density level, leaving approximately 650 sources at each epoch. It should be noted that at least a few non-asteroidal bright transients remain. A report on the statistics of these catalogs is given by Stapelfeldt et al. (2006).

Each catalog file consists of four columns: RA, DEC, 24-micron flux density, and the flux density uncertainty. Epoch 1 corresponds to the AORs labeled with basename MIPSC-PerX; Epoch 2 corresponds to the AORs labeled with basename MIPSC-PerX-2 (where X is a subfield index number).

### 3.3. Quality Files

For each target observed we have created a quality file tracking the history and describing the general state of the data. These quality files are labeled as "sourcename_quality.txt" (e.g., "L1014_quality.txt"), and they are included for each target. The files include the source name, AOR identification numbers, dates of observation, and a description of the observing strategy. They also include the software version numbers used to process the data as it proceeded through the c2d pipeline. Finally, comments are included about the general state of the data (artifacts, cautions, etc.) for all of the isolated cores as well as any other targets which showed anything noteworthy as they were being processed.

The c2d observations of the wTTS are more complicated than the observations of the small isolated cores or the maps of the large clouds. Often the "cluster mode" option was used in order to observe more than one wTTS in a single AOR. Thus, there are many cases where the MIPS observations of a wTTS can be found under the AOR of one primary target, while the IRAC observations of the same wTTS can be found under the AOR of a different primary target. Furthermore, some wTTS were not observed as separate AORs because they were included in the maps of the five large clouds. Finally, still other wTTS were only observed with one of the two instruments (IRAC or MIPS) because observations with the other instrument were included in a GTO program. For all wTTS in this last category, we have downloaded the GTO data from the *Spitzer* archive, processed it through the c2d pipeline, and included it in this data delivery.

The quality files are particularly useful for the wTTS observations. For each wTTS the quality file documents exactly what was and was not observed in c2d and GTO programs, whether the wTTS was observed as part of a cluster, and whether or not it is in one of the cloud maps. While it may appear that the observations of a certain wTTS are missing, it is important to check the

quality file because it may simply be a case of the data being found elsewhere. Table 3 summarizes this information, but the quality files should be consulted for detailed information concerning the observations of each wTTS.

## 3.4. Completeness and Reliability

We have chosen in this delivery to emphasize completeness while not sacrificing the ability to construct a reliable catalog. Since these goals obviously compete with each other, it is inevitable that a more complete catalog will have a higher fraction of artifacts. Consequently, we deliver both the Full Catalog (more complete and less reliable) and the High Reliability Catalog (less complete and more reliable).

We describe in this section two aspects of these topics: first, we describe tests of the completeness and reliability in the point source extraction process (§2.3.2); second, we describe the completeness limits based on the luminosity functions (§3.4.2).

### *3.4.1. Extraction of Artificial Stars*

We have estimated the completeness level and reliability of the extraction process by a commonly used technique, inserting artificial "stars" into the images and then reprocessing those images and measuring what fraction of the artificial sources were found, and how accurately their fluxes were determined. In detail, we chose two large cloud regions for these tests in order to have sufficient statistics for a reasonable estimate, Chamaeleon II and Serpens. These two clouds collectively have star densities that span the range of those observed in half of the regions (e.g., the most crowded regions where confusion is most likely) of isolated cores and stars covered by the c2d program. In the other half, the star densities in these core and star fields are significantly less than in Chamaeleon II and Serpens, and confusion is less likely. Furthermore, using these large clouds means that we can insert a reasonable number of sources for statistical purposes without affecting strongly the source confusion in the image. The Chamaeleon II region that was mapped had an area of about 2.2 $\deg^2$ and the Serpens region an area of about 1.0 $\deg^2$. For each cloud in each band we inserted 2500 sources, 100 in each of 25 magnitude bins, separated in bins of 0.25 mag. Table 18 lists the range of magnitudes and corresponding fluxes for each band. The artificial source profiles were generated using the point spread function that we use for the source extractions, which is close to, but obviously not identical to the actual point spread function. The sources were inserted at random positions over the area of each mosaic that was farther than 2 pixels from any edge of the valid mosaic. Then the single-frame version of c2dphot was used to extract all sources in the mosaic. In addition to this extraction on the "real+artificial" mosaic, we also perform an extraction on an "artificial-only" mosaic — a mosaic with exactly the same artificial stars (positions and fluxes) and noise characteristics as close as possible to that in the original mosaic. By comparing

the extraction statistics from the real+artificial and artificial-only mosaics, we can estimate the fraction of incompleteness due to source confusion rather than a simple lack of S/N.

Figures 13 - 20 show the results of the comparison of the extraction list and the truth list for both the real+artificial mosaic and the artificial-only mosaic. First, except at the faintest fluxes, an insignificant number of false extractions are found. In most cases, the completeness ratio in the artificial-only case, and therefore indicative of S/N effects, is nearly unity for many examples, especially compared to the completeness ratio in the real+artificial case, which is indicative of both S/N and confusion effects. Thus, most of the incompleteness in the real+artificial case, and indeed in extractions on our c2d mosaics, is due to confusion. In fact, we have examined several tens of artificial stars, missed by the extraction, in the real+artificial mosaic to determine the type of problems that led to them not being extracted. In *every* case we checked, the missing artificial star was invisible to our hands-on check due to being obscured by a real star bright enough to mask the undetected artificial star. In regions of substantial source confusion, e.g. the Galactic Plane observed with IRAC, it is clear that the precise definition of "Completeness Limit" depends on what astrophysical question is being considered.

### *3.4.2. Luminosity Functions*

Another approach to estimating the 90% completeness limits is to determine the peaks of the observed luminosity functions (e.g., Lada, Alves, & Lada 1999), provided the population of young stellar objects relative to the field is not significant enough to obscure or shift this peak brightward (e.g., Muench et al. 2002). We construct these luminosity functions for the IRAC and MIPS1 bands for the clouds and show them in Figures 21 and 22. The luminosity functions of MIPS2 have also been included, but we caution that the numbers of MIPS2 sources are sometimes relatively small. For Lupus and Ophiuchus, we have combined the respective subregions in each case in order to better sample the 70-$\mu$m source distributions. The peaks of these distributions, which we assume to be estimates of the 90% completeness limits, are listed in Table 19. For convenience, these limits are listed in magnitudes and fluxes. The luminosity functions were constructed with bins of width 0.2 mag in all bands except MIPS2, which was constructed with 0.5 mag bins. Thus, neglecting systematic errors in assuming the peak corresponds to the completeness limits, we set the uncertainties in these limits to be half these bin widths, or $\sim$10% (IRAC, MIPS1) and $\sim$30% (MIPS2) in flux.

## 3.5. Photometric and Calibration Uncertainties

### *3.5.1. Repeatability and the Revision of Uncertainties*

In this section, we estimate statistical and systematic uncertainties in the photometry by measuring photometric repeatability between our observations and those of other programs with deeper observations of the same targets. Following the c2d observations, some c2d targets have been re-observed to greater depths by other programs. Lee Mundy (PID 3656; "DeepCores") and Phil Myers (PID 20386; "Cores2Deeper") obtained observations of select cores to increase the exposure times by at least a factor of 10 in most cases. Some of these cores are listed in Table 20 and have been used in the analysis presented here to assess the reliability of IRAC and MIPS photometric uncertainties automatically generated by c2dphot, which are the photometric uncertainties cited in our previous deliveries of c2d data.

Only sources detected by both the c2d and deep observations, in a given band, were included in this analysis. Furthermore, only those sources located in the regions covered by all four IRAC bands and MIPS1 in both the c2d and deep observations were considered. Finally, all "complex" sources (those with at least one of IRAC or MIPS detection qualities assigned a value "K") were not considered. Adopting the zero points listed in Table 21, fluxes and flux uncertainties were converted to magnitudes and magnitude uncertainties, $[\lambda]$ and $\delta[\lambda]$, respectively. The IRAC photometric uncertainties as a function of magnitude are plotted in Figure 23 for all the sources meeting the selection criteria in the 17 cores listed in Table 20. As expected, for a given magnitude, the c2d observations have a greater photometric uncertainty than the deeper observations.

The task is to compare the photometry of sources detected in the c2d observations with the photometry of the same sources detected in the deep observations. Figure 24 shows a direct comparison of the photometry as a function of magnitude in each of the IRAC bands. We refer to the difference between the deep and c2d photometry as the repeatability:

$$\Delta[\lambda] = [\lambda]_{\rm deep} - [\lambda]_{\rm c2d}, \tag{4}$$

where $[\lambda]_{\rm deep}$ is the magnitude of a source from the deeper data and $[\lambda]_{\rm c2d}$ is the magnitude of a source from the c2d data.

For each band, there appears to be no systematic offset between the deep and c2d photometry (i.e., the repeatability is typically near zero) and, in general, the repeatability is marked by an ever broader dispersion with increasing magnitude, as expected.

We refer to the RMS of the repeatability, the *observed repeatability dispersion* denoted by

$$\sigma(\Delta[\lambda])_{\rm observed} = \sigma([\lambda]_{\rm deep} - [\lambda]_{\rm c2d}). \tag{5}$$

With this definition, the repeatability dispersion of photometry naturally grows with increasing

magnitude.

By comparing the *observed repeatability dispersion* to the **theoretical repeatability dispersion** calculated from our uncertainties in the photometry, we can assess the accuracy of our uncertainties. The theoretical repeatability dispersion is calculated from

$$\sigma(\Delta[\lambda])_{\rm theory} = \sqrt{(\delta[\lambda]_{\rm deep})^2 + (\delta[\lambda]_{\rm c2d})^2}. \quad (6)$$

In order to reliably compute the observed repeatability dispersion, a range of magnitudes for each IRAC band has been defined, by inspection, as indicated in Figure 24. Sources brighter than this range are excluded due to uncharacteristically large dispersions in photometry, presumably due to the sources being saturated in the deep observations. The deep observations were obtained from images having 30-second integration times, while the c2d observations were obtained with 12-second integration times. Thus, brighter sources will saturate in the deep observations and may explain the greater differences in photometry for the brightest sources seen in Figure 24. On the other hand, very faint sources, especially those near and fainter than the limiting magnitude of the c2d observations, are likely to represent an incomplete distribution due to an observational bias skewing the distribution toward brighter detections. The completeness limits of c2d observations of these cores are typically fainter than those of the cloud observations given in Table 19. At each band, by inspection, we chose the faint end of our range in order to avoid faint sources that would skew our computation of $\sigma(\Delta[\lambda])_{\rm observed}$. The faint ends of our ranges are near to or brighter than the completeness limits of the c2d core observations. For each IRAC band, the observed repeatbility dispersions within the considered range were determined by computing the standard deviation of the difference in photometry within bins of width 0.5 mag. These observed repeatability dispersions are plotted for IRAC in Figure 25 and for MIPS1 in Figure 26.

The theoretical repeatability dispersions are also plotted in Figures 25 and 26 for comparison with the observed dispersions. The observed values are always greater than the theoretical ones. Consequently, we increased the photometric uncertainties generated by c2dphot and list these revised flux uncertainties in the catalogs. The discussion that follows describes how we modified the c2dphot photometric uncertainties.

The discrepancy between the observed and theoretical dispersions is not consistent with a single additive offset or multiplicative correction factor. Instead, we assume that this discrepancy may be characterized by two parameters: (1) a "floor" to the observed repeatability dispersion, likely resulting from systematic uncertainties in data and photometry; and (2) a multiplicative factor, likely the result of underestimating the statistical uncertainties, by which to scale the theoretical dispersions to be consistent with those observed. With this parameterization, the revised photometric uncertainties are given by

$$\delta[\lambda]_{\rm revised} = \sqrt{\Gamma_\lambda^2 + (\gamma_\lambda \delta[\lambda]_{\rm c2d})^2}, \quad (7)$$

where $\Gamma_\lambda$ is the floor and $\gamma_\lambda$ is the multiplicative factor. After modifying the photometric uncertainties in this manner, the revised theoretical repeatability dispersions are then

$$\sigma(\Delta[\lambda])_{\rm revised} = \sqrt{2\ \Gamma_\lambda^2 + \gamma_\lambda^2\ [(\delta[\lambda]_{\rm deep})^2 + (\delta[\lambda]_{\rm c2d})^2]}. \tag{8}$$

By imposing

$$\sigma(\Delta[\lambda])_{\rm revised} = \sigma(\Delta[\lambda])_{\rm observed}, \tag{9}$$

we may fit for the best values for $\Gamma_\lambda$ and $\gamma_\lambda$ to yield revised theoretical repeatability dispersions consistent with the observed values.

For the IRAC bands, we find that the floors of $\Gamma_\lambda = 0.05$ and factors of $\gamma_\lambda = 2.3$ provide reasonably good fits. For the MIPS1 band, we find that a floor of $\Gamma_{24} = 0.10$ and factor of $\gamma_{24} = 2.3$ is sufficient. With these results, we may express the revised flux uncertainties, which are cited in the catalogs, in terms of the fluxes $F_\nu$ and original flux uncertainties $\delta F_{\nu,{\rm orig}}$ as

$$\delta F_{\nu,{\rm revised}} = \begin{cases} \sqrt{0.0460^2\ F_\nu^2 + 2.3^2\ (\delta F_{\nu,{\rm orig}})^2} & \text{for IRAC bands} \\ \sqrt{0.0921^2\ F_\nu^2 + 2.3^2\ (\delta F_{\nu,{\rm orig}})^2} & \text{for MIPS1 band} \\ \sqrt{0.0921^2\ F_\nu^2 + (\delta F_{\nu,{\rm orig}})^2} & \text{for MIPS2 band} \end{cases} \tag{10}$$

As given above, for the MIPS2 flux uncertainties, we simply adopted the MIPS1 floor with no scale factor. The revised IRAC and MIPS flux uncertainties, which include our best estimates of the statistical and systematic uncertainties in our photometry, are the ones we give in our final catalogs, and they are used to assign the quality of detection flags (§2.4.5).

### *3.5.2. Photometry of Standard Stars*

We tested the reliability of photometry resulting from our pipeline by processing AORs that included standard star observations obtained for other programs. The standard magnitudes of the 14 stars included in our sample are listed in Table 22. These standard stars were chosen to span a large range in flux in order to validate our photometry for as many sources in our catalogs as possible and test for systematic photometric offsets as a function of flux.

The AORs used in this analysis are those listed in Table 5. Many of these AORs included more than 4 dithers, but we considered only 4 dithers in each case since our c2d observations included 4 dithers. In some cases, the standard star AORs included only 2 dithers and we therefore combined 2 AORs to form a set of 4 dithers at each band. The observed magnitudes for the standard stars

are listed in Table 5. In Figure 27, we plot the relative offset between our observed photometry and standard photometry, given by

$$\mathcal{F}_\lambda = 100\% \times \left[\frac{F_\lambda(\mathrm{observed})}{F_\lambda(\mathrm{standard})} - 1\right], \tag{11}$$

as a function of the standard flux, $F_\lambda$(standard). No trend in photometric offset as a function of flux is evident in these plots. We fit for constant photometric offsets, and these results are listed in Table 24. We find that photometry derived from our pipeline is consistent with expected photometry to within 5%.

Because of the uncertainties in the offsets listed in Table 24, and the relatively large dispersion in these offsets even for independent observations of the same standard star, we do not "correct" the photometry in our catalogs. We believe that the 5% systematic uncertainties in IRAC photometry derived in §3.5.1 are more secure than the small offsets derived here and are the dominant systematic uncertainties in our photometry.

#### *3.5.3. Absolute Calibration Uncertainties*

The photometric uncertainties listed in our catalogs represent both statistical and systematic uncertainties. There is one more form of uncertainty, which is the uncertainty in the absolute calibration of flux. We give our adopted fluxes for zero magnitude and their uncertainties in Table 21. These calibration uncertainties are not included in the uncertainties listed in the catalogs, but they have been added in quadrature to the catalogued uncertainties for the purposes of source classification. The values of the fluxes for zero magnitude and the uncertainties of 1.5% for the IRAC bands are based on Table 5.1 in the Infrared Array Camera Data Handbook, Version 3.0. The values for MIPS come from Table 3.8 of the Multiband Imaging Photometer for Spitzer (MIPS) Data Handbook, Version 3.3.0, with the following exception. That table gives calibration uncertainties of 7% for 70 $\mu$m and 12% for 160 $\mu$m. Based on our own experience with photometry at these wavelengths, we instead use 20% uncertainties for both. These are not, strictly speaking, absolute flux calibration uncertainties, but we think they reflect more realistic uncertainties for analysis of SEDs. Similarly, we assign 10% uncertainties to 2MASS absolute calibration in an attempt to capture uncertainties inherent in combining data from very different instruments and photometric methods.

### 3.6. Known Artifacts: Effects on Results

The most significant effects on our extraction lists/catalogs of the known artifacts are the detection of fictitious sources for two reasons. Despite our correction for muxbleed, the residual pattern can produce a line of higher and lower pixels in IRAC images; in some cases, these can be

detected as a short string of faint objects. There are some ways to tune the source extraction to minimize this, but because there are undesirable side effects to finding real sources, we do not do this. In the MIPS 24 data especially, the presence of latent images on either side of some bright objects, spaced by the exposure spacing in MIPS Small Field Photometry mode ($\pm 2'$) has probably also led to a very small number of fictitious sources in those object lists. These are typically offset along the "Y" axis in the mosaics. In a couple of cases in the MIPS 24 images, there are stars that are so bright that some point-like features in the diffraction pattern are identified as relatively high S/N sources.

The checks performed during band-merging removed many of these artifacts. In Serpens we removed approximately 3,000, or $\sim 1\%$, of the IRAC1 detections because we believed them to be artifacts. We removed a similar fraction of the IRAC2 and IRAC3 detections, and $\sim 3\%$ of the IRAC4 detections. For MIPS 24, we removed $\sim 4\%$ of the detections that appeared to be artifacts. Because of this visual inspection, we believe the number of artifacts in the final catalogs is very small.

### 3.7. Extinction Maps

One of the products of the c2d pipeline is an estimate of the visual extinction toward each source classified as a star (§2.5.2), based on the SED from 1.25 $\mu$m to 24 $\mu$m, providing measures of the visual extinction through many lines of sight through the molecular clouds imaged by our team. We use the Weingartner & Draine (2001) extinction law with $R_V = 5.5$ (§2.5.2). For each molecular cloud, we have convolved these line-of-sight measures of extinctions with uniformly spaced Gaussian beams to construct an extinction map of that cloud.

For each cloud, maps of different resolutions were constructed using Gaussian beams with different FWHM. The lowest resolution maps were constructed with $300''$ beams, while the highest resolution maps that we could reliably construct depended on the peak extinction through the cloud and the density of background stars. Table 25 specifies the resolutions of the maps that we deliver. For example, extinction maps constructed with $90''$, $120''$, $150''$, ..., $300''$ beams are available for Serpens, while the lower background star density toward Perseus allows us to reliably construct and deliver only lower resolution maps constructed with $180''$, $210''$, ..., $300''$ beams. The minimum resolution of $270''$ available for the main part of Ophiuchus is limited not by the background star density but by the relatively large extended region of high extinction where very few stars are observed.

For studies based on cloud-to-cloud comparisons that make use of these extinction maps, it may be important to use maps constructed with beams of the same size. In such cases, the highest resolution maps these studies may reliably use depends on the clouds being compared. For example, a study that involves Chamaeleon, Perseus, and Serpens should be limited to using maps constructed with the 180–$300''$ beams.

For each extinction map, there is a corresponding map of an estimated uncertainty in the beam-averaged extinction, computed by beam-averaging the uncertainties in the individual line-of-sight extinctions. Thus, these uncertainty maps account for statistical photometric uncertainties, but do not include uncertainties associated with undersampled beams or systematic uncertainties associated with calibration.

Finally, for diagnostic purposes, we have provided for each extinction map a corresponding map of the number of stars within half the beam FWHM of the pixel center. While the beam extends well beyond such a radius and more stars contribute to each beam-averaged extinction value, this map of the number of stars is a good indication of how well sampled the beams are within the extinction map. Our choice of resolutions yield extinction maps where nearly all the beams are well sampled, but there may be some isolated regions within each map with beam-averaged extinction values derived from undersampled beams. Our delivered maps of the numbers of stars may be used to identify such problematic regions.

The file naming convention for the maps of extinction, extinction uncertainty, and number of stars is straightforward. As an example, the maps for Serpens constructed with a $90''$ beam have filenames of 'SER_90asec_Av.fits', 'SER_90asec_sigAv.fits', and 'SER_90asec_NstarsPEAK.fits', respectively. The headers of these fits files contain standard astrometry information, which conform to the World Coordinate Standard system, providing proper registration when read into DS9, *IDL*, *IRAF*, and most astronomical software.

### *3.7.1. Line-of-Sight Extinction Offsets*

The fitted values for line-of-sight extinction were checked for systematic offsets by examining the distribution of $A_V$ values for stars in the off-cloud fields that were observed in all IRAC bands and the MIPS1 band. We observed six such off-cloud fields for each of Chamaeleon, Perseus, and Ophiuchus. In each case, the six off-cloud fields yield similar distributions of $A_V$ values; thus, we combine the six off-cloud fields to improve our characterization of these distributions for each cloud. For Serpens, we observed only one off-cloud field with both IRAC and MIPS, while two such off-cloud fields were obtained for Lupus. The distribution of $A_V$ values in these off-cloud fields are plotted in Figure 28. The dominant portions of these distributions were fitted with Gaussian profiles to estimate the mode $A_V$ values, listed in Table 26.

The mode $A_V$ values in these off-cloud fields are seen to range from 1.07 for Chamaeleon to 3.51 for Serpens. We may confirm that the off-cloud fields are sufficiently off the molecular cloud by characterizing the distribution of observed H−K colors of stars in these fields. Typical intrinsic H−K color of stellar populations behind molecular clouds are usually found to be ∼0.13–0.18 mag (e.g., Harvey et al. 2001; Lada et al. 1999; Alves et al. 1998), corresponding to spectral types of late K to early M. If the H−K colors of stars in any of the off-cloud fields are greater than this, then we may assume those fields were not sufficiently off the cloud. The distribution of H−K colors

are shown in Figure 29, and the mode values are listed in Table 26.

The H−K colors of stars in the Chamaeleon and Perseus off-cloud fields are consistent with typical intrinsic colors of stellar populations; thus, we assume these fields are sufficiently off the clouds and the stars in those fields are representative of the background stellar populations toward those clouds. Similarly, the H−K colors for stars in the Lupus OC1 field and the Ophiuchus off-cloud fields suggest that stars in those fields represent the background stellar populations toward those clouds. The distributions of H−K colors for stars in the Serpens off-cloud field and Lupus OC2 are offset from typical intrinsic colors, consistent with the presence of extinction from the molecular clouds, and likely explain the greater fitted line-of-sight extinctions toward those stars. We can ignore Lupus OC2 since stars background to Lupus are fairly represented by the Lupus OC1 stars. Since Serpens OC1 is the only off-cloud field we observed for Serpens, we do not have an accurate representation of the Serpens background stars.

The adopted offsets in the fitted line-of-sight extinctions for stars toward each of the molecular clouds are listed in Table 27. The adopted offset (and uncertainty) for Serpens stars was determined by the average (and dispersion) of the offsets for the other clouds. It is unclear whether these offsets are typical line-of-sight extinctions attributed to the diffuse interstellar medium or systematic errors introduced by our simultaneous fitting of both spectral type and extinction. In either case, it is clear that these offsets are not associated with extinction from the molecular clouds. Our catalogs list the fitted line-of-sight extinction values toward stars, which include this offset. In constructing extinction maps, we subtract the offsets listed in Table 27 from the line-of-sight extinctions listed in the catalogs; thus, the maps represent extinction from **only** the molecular clouds and **not** the diffuse interstellar medium.

### *3.7.2. Stars Considered in Extinction Map Construction*

In Figure 30, we plot the uncertainties in the line-of-sight extinction for Serpens, as listed in the catalog (which do not include uncertainties in the extinction offsets listed in Table 27), as a function of the line-of-sight extinction for sources classified as stars. From this plot, it is clear that there are stars with SEDs that well constrain the line-of-sight extinction (e.g., $\sigma_{A_V} \leq 2$) and stars with SEDs that only weakly constrain the extinction (e.g., $\sigma_{A_V} > 2$). Referring to Figure 30, we see that the former are primarily those stars with at least one 2MASS near-infrared detection, while the latter are primarily sources detected only by Spitzer. For this reason, here, we refer to stars with well constrained line-of-sight extinctions, $\sigma_{A_V} \leq 2$, as "near-infrared stars" and those with less constrained extinctions, $\sigma_{A_V} > 2$, as "Spitzer-only stars".

Our approach in constructing extinction maps was first to use only the near-infrared stars to construct preliminary maps of beam-averaged extinction, $A_{V,\mathrm{map}}$. These near-infrared stars will provide well-constrained extinctions, but they sparsely sample high extinction regions where we will need to rely more on the weakly constrained extinctions provided by the Spitzer-only stars.

We examined the distribution of Spitzer-only sources, chosen with five different quality criteria, on the preliminary maps. These five different quality criteria are given by

$$\sigma_{A_V}/A_V \leq [0.1, 0.2, 0.3, 0.4, 0.5] \quad \text{and} \quad \sigma_{A_V} > 2. \tag{12}$$

Figure 31 illustrates the positions of Spitzer-only sources for two of these criteria overlayed on the preliminary extinction maps of Serpens. For the criteria associated with higher quality ($\sigma_{A_V}/A_V \leq 0.2$) extinction measures, the distribution tends to follow the regions of higher extinction, as expected. For the criteria associated with lesser quality ($\sigma_{A_V}/A_V \leq 0.4$) extinction measures, the Spitzer-only sources are distributed over all regions with only a weak tendency toward high extinction regions. From Figure 30, we see that most of these Spitzer-only sources have line-of-sight extinctions of $A_V \gtrsim 20 - 30$ and large uncertainties (e.g., $\sigma_{A_V} \gtrsim 6 - 8$). These isolated Spitzer-only sources exhibiting such large extinctions present within the extended low extinction region, where the preliminary extinction map should contain sufficiently large number of near-infrared stars from which to reliably determine the extinction, are presumably yielding discrepant line-of-sight extinction measures. Alternatively, these Spitzer-only sources may be tracing extremely small clumps ($<60''$) with very sharply rising column density profiles. We assume the former, and consider such Spitzer-only sources as "contamination", which would result in artificial isolated clumps distributed throughout the low extinction region in an extinction map, such as seen in Figure 32.

In order to make a judicious choice for the criteria for inclusion of Spitzer-only sources in constructing extinction maps, we quantify this contamination by plotting the number density of Spitzer-only sources added for increasingly less restrictive criteria as a function of beam-averaged extinction in the preliminary maps constructed with $300''$ beams. For example, in Figure 33, we show these histograms for the Serpens and Perseus clouds. If we assume that the Spitzer-only sources at lower beam-averaged extinctions do not provide reliable measures of line-of-sight extinction, then we find that the number of these sources with $0.2 \leq \sigma_{A_V}/A_V < 0.3$ is substantially greater than at $0.1 \leq \sigma_{A_V}/A_V < 0.2$. For this reason, we consider only those Spitzer-only stars with $\sigma_{A_V}/A_V \leq 0.2$. Furthermore, by imposing the additional criteria that the Spitzer-only stars be associated with a region of high extinction, specificially $A_{V,\mathrm{beam}} > 7$ on the preliminary maps constructed with the $300''$ beam, we optimize the number of Spitzer-only stars contributing useful line-of-sight extinction measures while minimizing the number of these stars causing artificial clumps.

The preliminary extinction maps were replaced by maps that made use of both near-infrared stars and qualifying Spitzer-only stars. Maps for each cloud were constructed with Gaussian beams of different FWHM: $60''$, $90''$, $120''$, ..., $300''$. Some of the maps constructed with the smallest beams (i.e., those maps with the highest resolution) contain many undersampled beams and therefore unreliable extinctions over a significant portion of the map. To quantify this undersampling, we examined the number of stars within half the FWHM of the beam center (or, the primary part of the beam) for each position in an extinction map. Sorting the pixels by $A_V$, and grouping in bins of width $\Delta A_V = 5$, we find for each map the fraction of pixels with no stars under the primary part of the beam relative to the those with at least one star, $f_{nb}(A_V, FWHM)$. Regions

of higher extinction are more likely to contain undersampled beams than low extinction regions; thus, we expect $f_{nb}(A_V, FWHM)$ to increase with $A_V$, in general. For example, Figure 34 shows the results for the Serpens map constructed with the 60″ beam, illustrating this trend. Repeating this procedure for the other Serpens maps constructed with other beams, we assess the reliability of each maps by considering the maximum fraction of pixels with undersampled beams for each map,

$$F_{nb}(FWHM) = \max [\ f_{nb}(A_V, FWHM)\ ]\,. \tag{13}$$

As the beam size increases, the maximum number of pixels with undersampled beams will decrease, as is shown in Figure 35 for Serpens and the other clouds. For the map constructed with the 60″ beam, as many as ∼16% of the pixels in a particular $A_V$ range (with $\Delta A_V = 5$) represent undersampled beams. The fractional number of undersampled beams decreases with greater beam sizes until FWHM = 120″, which contains no undersampled beams ($F_{nb} = 0$). Thus, all pixels in the Serpens maps constructed with beams of FWHM of 120″ or greater should represent reasonably reliable beam-averaged extinctions. Similar trends are found for maps of other clouds, except that the increase of $F_{nb}$ toward greater resolutions occurs at different beam sizes. In particular, for $F_{nb} \gtrsim 10\%$, the increase with greater resolution is substantial. Therefore, we have chosen to deliver only those maps with $F_{nb} \leq 10\%$.

#### *3.7.3. Resampling of Extinction Maps*

Finally, the extinction maps were constructed by convolving the line-of-sight extinctions with beams separated by a constant offset in RA and Dec. Specifically, the offset is three times less than that for Nyquist spacing. For example, an extinction map constructed with a 90″ beam has a grid of pixels with columns and rows separated by 15″ in RA and Dec, respectively. The astrometry of such a map, with pixels separated by constant offsets, cannot be described in a conventional format in the FITS header, which typically assumes the pixels represent a tangential projection. To include precise astrometry in the FITS headers of our extinction maps, these maps were resampled onto such a grid. For this reason, the maps of the numbers of stars do not contain integer values.

### 3.8. Resampled SWIRE Catalogs: Use as Control Catalogs

We use the IRAC and MIPS images of the ELAIS N1 field obtained by the SWIRE team as a control field for understanding the extragalactic population with colors that mimic those of YSOs in our fields. This SWIRE field, expected to contain no extinction from a molecular cloud and no YSOs, has coverage by both IRAC and MIPS of 5.31 deg$^2$ and is significantly deeper than our observations. For each molecular cloud that we have observed, we use this SWIRE field to approximate our products (e.g., source extractions, photometry, and classification) if (1) that molecular cloud had been in the foreground of the SWIRE field and (2) the SWIRE observations

had been obtained with sensitivities similar to those of our observations. In this section, the process of simulating these effects is discussed in detail for the Serpens cloud, but this process is identical for the other clouds.

To avoid effects that may result from differences in data processing, the BCD files for this SWIRE field were processed by our pipeline in exactly the same way as our own observations, except that we do not perform bandfilling on the SWIRE catalogs. Since the SWIRE data were already considerably deeper than c2d data, we instead extracted sources from the SWIRE observations as faint as 5 times fainter than those extracted from our c2d observations. Similar luminosity functions for the catalogued SWIRE sources, shown in Figure 36, demonstrate that the peak for each Spitzer band occurs at fainter sources than for the c2d Serpens observations.

After constructing our bandmerged catalogs of SWIRE sources, we first simulated the extinction of sources that would occur if Serpens had been in the foreground of this field. This extinction was accomplished by determining the profile of reliable line-of-sight extinctions in Serpens, shown in Figure 37, and then applying these extinctions randomly to the SWIRE sources. For example, $\sim$8.3% of SWIRE sources were randomly selected and visual extinctions in the range $4.75 \leq A_V < 5.25$ were applied, $\sim$9.0% of sources were extincted by amounts in the range $5.25 \leq A_V < 5.75$, and so forth. Table 28 specifies the extinctions applied to each band, relative to $A_V$, using the $R_V$=5.5 law of Weingartner & Draine (2001), the same extinction law used to derive the line-of-sight extinctions in our catalogs (see §2.5.2).

Second, we degraded the sensitivity of the extincted SWIRE photometry to match that of our Serpens observations. This was accomplished by: (1) re-assigning the photometric uncertainties of extincted SWIRE sources to values similar to those of Serpens sources with similar magnitudes, and (2) "matching" the shape of the extincted SWIRE luminosity function in each band to the corresponding Serpens luminosity function plotted in Figure 21 and previously discussed in §3.4.2 By "matching" the shape of a luminosity function for a given band, we specifically mean that we assume that the 90% completeness limit of our c2d observations is given by the peak of the luminosity function and that we force the luminosity function of a *resampled* catalog of extincted SWIRE sources to exhibit the same shape as that of the c2d luminosity function faintward of this peak for that band. For a given band, all extincted SWIRE sources in magnitude bins brighter than the Serpens completeness limit would be detectable by c2d-like observations and are identified as such in the resampled SWIRE catalog (e.g., the qualities of detections are not set to 'U', but instead are recomputed based on the extincted fluxes and revised photometric uncertainties). Next, 90% of the extincted SWIRE sources in the magnitude bin corresponding to the peak of the c2d luminosity function are identified as detections in the resampled SWIRE catalogs; 10% are identified as non-detections (e.g., the qualities of detections are set to 'U'). Likewise, for sources fainter than the Serpens completeness limit in that band, we randomly select which sources to identify as detections in that band in such a way as to reproduce the shape of that Serpens luminosity function (from its maximum to fainter sources). This *resampling* process is performed for each band, resulting in those sources fainter than the completeness limits in some bands being detected or not detected

with the same probabilities as those for similar sources in Serpens. We plot in the lower panel of Figure 36 the luminosity functions of a resampled SWIRE catalog, for comparison with those of the original SWIRE catalog (upper panel of Figure 36) and the Serpens catalog (Figure 21). Clearly, the sensitivities of the resampled SWIRE catalog are diminished compared to those of the original SWIRE catalog, and they are very similar to those characterizing our c2d observations of Serpens.

Finally, after performing the resampling process for all bands, each source in the resampled SWIRE catalog for Serpens is re-classified, based on its degraded photometry. The fluxes, colors, classifications, etc. of sources in this resampled SWIRE catalog are then directly comparable to those in the Serpens catalog and may be used to estimate the population of extragalactic sources satisfying various color and magnitude criteria. Because the resampling process is inherently statistical, we supply six statistically independent realizations (identified as "resampled-SWIRE-SER_v1-FULL.tbl", "resampled-SWIRE-SER_v2-FULL.tbl",..., "resampled-SWIRE-SER_v6-FULL.tbl" of resampled SWIRE catalogs for Serpens in order to provide a guide for the degree to which analyses may change solely due to this resampling process. Additionally, since the 70 $\mu$m luminosity function and its peak (and therefore the 90% completeness limit at 70 $\mu$m are particularly uncertain due to small numbers of 70 $\mu$m sources detected, we have provided a way to account for the effects of these larger uncertainties on studies making use of the resampling of 70 $\mu$m sources in these catalogs. The third and fourth realizations ("resampled-SWIRE-SER_v3-FULL.tbl" and "resampled-SWIRE-SER_v4-FULL.tbl") were made by shifting the 90% completeness limit at 70 $\mu$m by 0.5 mag *faintward* from its nominal position of [70] = 1.0 mag, as indicated in Figure 21 and Table 19. The fifth and sixth realizations ("resampled-SWIRE-SER_v5-FULL.tbl" and "resampled-SWIRE-SER_v6-FULL.tbl") were made by shifting the 90% completeness limit at 70 $\mu$m by 0.5 mag *brightward* from its nominal position. All six realizations use the nominal luminosity functions and completeness limits for the IRAC and MIPS-1 bands for the resampling process; those luminosity functions are more reliable and therefore no shifting of the completeness limits was done.

In Figure 38, we show the profiles of the line-of-sight extinctions for sources in the original SWIRE catalog and the profiles after the resampling process. Here, we emphasize a point made in §3.7 concerning the reliability of the line-of-sight extinctions in our catalogs. While this SWIRE field is expected to be free of significant extinction, there is a significant extension of the profile toward high extinctions in the original SWIRE catalog. Almost exclusively, this extension represents discrepant extinction measures resulting from fitting of SEDs with only Spitzer detections. After one removes the Spitzer-only stars and considers only the near-infrared stars, then the extinction profile is more reasonable for this SWIRE field.

In addition to the six realizations of the Full resampled SWIRE catalog for Serpens, we have provided a High Reliability and YSOc Catalog derived from each realization, for comparison with the High Reliability and YSOc Catalogs we deliver for Serpens. Of course, we do not expect there to be any real YSOs present in the SWIRE field; therefore, sources present in the YSOc resampled SWIRE catalogs may indicate the frequency (after accounting for the relative sizes of the Serpens and SWIRE regions) with which extragalactic sources mimic YSO SEDs in our Serpens

field. Finally, the resampling procedure was duplicated for all the large molecular cloud regions observed by c2d, and six Full, High Reliability, and YSOc resampled SWIRE catalogs are delivered for each region.

## 4. Summary

This is the fourth and final delivery of improved IRAC and MIPS products from the c2d legacy project.

We have documented our procedures and products (see Table 1), especially changes from those used in previous deliveries. We provide several kinds of catalogs. Choosing the right one for a particular project is important. One product is very complete, but is less reliable. Since completeness and reliability trade off, it is important to read carefully the section on completeness and reliability (§3.4). Catalogs tuned to the user's needs can be constructed from the information in the catalogs.

## REFERENCES

Alcalá, J. M., et al. 2007, submitted to ApJ.

Allen, L. E., et al. 2004, ApJS, 154, 363

Alves, J., Lada, C. J., Lada, E. A., Kenyon, S. J., & Phelps, R. 1998, ApJ, 506, 292

Chapman, N. et al. 2007, ApJ, in press (ArXiv e-prints, 706, arXiv:0706.1809)

Cutri, Skrutskie, van Dyk, Beichman, et al.(25 authors) 2003, "2MASS All-Sky Catalog of Point Sources", VizieR On-Line Data Catalog:II/246. Originally Published in: University of Massachusetts and Infrared Processing and Analysis Center, (IPAC/California Institute of Technology) (2003)

Enoch, M. L., et al. 2006a, ApJ, 638, 293

Enoch, M. L., et al. 2007, ApJ, in press ArXiv e-prints, 705, arXiv:0705.3984

Evans, N. J., II, et al. 2003, PASP, 115, 965

Harvey, P. M., et al. 2006, ApJ, 644, 307

Harvey, P. M. et al. 2007a, in prep.

Harvey, P.M., et al. 2007b, ApJ, 663, 1149

Harvey, P.M., et al. 2007c, ApJ, 663, 1139

Harvey, D.W.A., Wilner, D.J., Lada, C.J., Myers, P.C., Alves, J.F., & Chen, H. 2001, ApJ, 563, 903

Jørgensen, J. K., et al. 2006, ApJ, 645, 1246

Koornneef, J. 1983, A&A, 128, 84

Lada, C.J., Alves, J., Lada, E.A. 1999, in The Physics and Chemistry of the Interstellar Medium, eds. V. Ossenkopf, J. Stutzki, G. Winnewisser, 161

Lahuis, F., & Kessler-Silacci, J. E. 2006, "c2d Spectroscopy Explanatory Supplement," (Pasadena: *Spitzer* Science Center)

Lonsdale, C., et al. 2003, PASP, 115, 897

Mink, D.J. 1999, "WCSTools: Putting Image World Coordinate Systems to Use," in Astronomical Data Analysis Software and Systems VIII, A.S.P. Conference Series, eds. D. Mehringer, R. Plante, & D. Roberts, 498

Muench, A. A., Lada, E. A., Lada, C. J., & Alves, J. 2002, ApJ, 573, 366

Ochsenbein, F. 1980, "The SAO Catalogue with Astrophysical Data" Bulletin D'In. Cent. Donnees Stellaires V. 19, P. 74

Padgett, D., et al. 2007, ApJ, in press (ArXiv e-prints, 709, arXiv:0709.3492)

Porras, A., et al. 2007, ApJ, 656, 493

Press, W.H., Teukolsky, S.A., Vetterling, W.T., and Flannery, B.P. 1997, "Numerical Recipes in C", Cambridge U. Press.

Rebull, L. et al. 2007, ApJS, 171, 447

Rieke, G. H., & Lebofsky, M. J. 1985, ApJ, 288, 618

Schechter, P.L., Mateo, M., and Saha, A. 1993, PASP, 105, 1342.

Sivia, D.S. 1996, "Data Analysis: A Bayesian Tutorial", Clarendon Press, Oxford.

Stapelfeldt et al. 2006, DPS abstract, 38, 58.06

Weingartner, J. C., & Draine, B. T. 2001, ApJ, 548, 296

Young, K. E., et al. 2006, ApJ, 644, 326

## 5. Tables

Table 1: Summary of Products

| | | For Each of These | | | For Ensemble of These | |
|---|---|---|---|---|---|---|
| Product | Category | Cloud[a] | Core | Star | Cloud | Core |
| Images | Intensity | Y | Y | Y | N | N |
| Images | Intensity Uncertainty | Y | Y | Y | N | N |
| Images | Coverage | Y | Y | Y | N | N |
| Images | Extinction | Y[b] | N | N | N | N |
| Images | Extinction Uncertainty | Y[b] | N | N | N | N |
| Images | Background Star Density | Y[b] | N | N | N | N |
| Catalogs | Full | Y | Y | Y | N | N |
| Catalogs | High Reliability | Y | Y | Y | N | N |
| Catalogs | YSOc | Y | M[c] | M[c] | Y | Y |
| Catalogs | Resampled SWIRE Full | 6[d] | N | N | N | N |
| Catalogs | Resampled SWIRE HR | 6[d] | N | N | N | N |
| Catalogs | Resampled SWIRE YSOc | 6[d] | N | N | N | N |
| Specialty | MM Sources | 3[e] | N | N | N | N |
| Specialty | Transients | 2[f] | N | N | N | N |
| Quality File | ... | Y | Y | Y | N | N |

[a]For IRAC images with HDR, we deliver images both without ("A") and with ("COMB") the HDR frame added. Some clouds will have more than one image, particularly large clouds that are broken into subareas (Ophiuchus, Perseus), or clouds with separated pieces (Lupus). Also all clouds have separate images for off-cloud regions. See Tables 4 and 5.

[b]There are up to nine maps for each cloud with angular resolutions from 60″ to 300″, depending on the cloud (see §3.7).

[c]Maybe: a catalog is supplied only if there is at least one entry.

[d]There are six realizations for each cloud (see §3.8).

[e]There are catalogs for Perseus, Ophiuchus, and Serpens.

[f]There are two catalogs for Perseus, one for each epoch.

Table 2. Data Delivery 4: Cores

| Core Name | IRAC[a] | MIPS[a] | Epochs[b] | HDR[c] | IRAC File Code[d] |
|---|---|---|---|---|---|
| B18-1 | Delivery 4 | Delivery 4 | 2 | No | A |
| B18-2 | Delivery 4 | Delivery 4 | 2 | No | A |
| B18-5 | Delivery 4 | Delivery 4 | 2 | No | A |
| B35A | Delivery 4 | Delivery 4 | 2 | Yes | A, COMB |
| B59 | Delivery 4 | Delivery 4 | 2 | Yes | A, COMB |
| B72 | Delivery 4 | Delivery 4 | 2 | No | A |
| Bern48 | Delivery 4 | Delivery 4 | 1 | Yes | A, COMB |
| BHR14 | Delivery 4 | Delivery 4 | 1 | No | A |
| BHR16 | Delivery 4 | Delivery 4 | 1 | No | A |
| BHR22 | Delivery 4 | Delivery 4 | 1 | No | A |
| BHR47 | Delivery 4 | Delivery 4 | 1 | Yes | A, COMB |
| BHR59 | Delivery 4 | Delivery 4 | 1 | No | A |
| BHR76 | Delivery 4 | Delivery 4 | 1 | No | A |
| BHR78 | Delivery 4 | Delivery 4 | 1 | No | A |
| CB130-3 | Delivery 4 | Delivery 4 | 2 | No | A |
| CB188 | Delivery 4 | Delivery 4 | 2 | Yes | A, COMB |
| CB68 | Delivery 4 | Delivery 4 | 2 | Yes | A, COMB |
| CG30-31 | Delivery 4 | Delivery 4 | 1 | Yes | A, COMB |
| DC2573-25 | Delivery 4 | Delivery 4 | 1 | No | A |
| DC2660-75-1 | Delivery 4 | Delivery 4 | 1 | No | A |
| DC267.4-7.5[e] | Delivery 4 | Delivery 4 | 1 | Yes | A, COMB |
| DC2675-74 | Delivery 4 | Delivery 4 | 1 | No | A |
| DC2694+30 | Delivery 4 | Delivery 4 | 1 | No | A |
| DC2742-04 | Delivery 4 | Delivery 4 | 1 | No | A |
| DC275.9+1.9 | Delivery 4 | Delivery 4 | 1 | Yes | A, COMB |
| DC2910-35 | Delivery 4 | Delivery 4 | 1 | No | A |
| DC297.7-2.8 | Delivery 4 | Delivery 4 | 1 | Yes | A, COMB |
| DC2971-161-1 | Delivery 4 | Delivery 4 | 1 | No | A |
| DC3002-35 | Delivery 4 | Delivery 4 | 1 | No | A |
| DC3007-10 | Delivery 4 | Delivery 4 | 1 | No | A |
| DC302.1+7.4 | Delivery 4 | Delivery 4 | 1 | Yes | A, COMB |
| DC3023-177 | Delivery 4 | Delivery 4 | 1 | No | A |
| DC3026-159 | Delivery 4 | Delivery 4 | 1 | No | A |

Table 2—Continued

| Core Name | IRAC[a] | MIPS[a] | Epochs[b] | HDR[c] | IRAC File Code[d] |
|---|---|---|---|---|---|
| DC303.8-14.2 | Delivery 4 | Delivery 4 | 1 | Yes | A, COMB |
| DC3272+18 | Delivery 4 | Delivery 4 | 2 | No | A |
| DC3369+83 | Delivery 4 | Delivery 4 | 2 | Yes | A, COMB |
| DC3386+95 | Delivery 4 | Delivery 4 | 2 | No | A |
| DC3391+117-2 | Delivery 4 | Delivery 4 | 2 | No | A |
| DC3460+78 | Delivery 4 | Delivery 4 | 2 | No | A |
| DC3463+78 | Delivery 4 | Delivery 4 | 2 | No | A |
| DC3464+79 | Delivery 4 | Delivery 4 | 2 | No | A |
| IRAM04191+1522 | Delivery 4 | Delivery 4 | 2 | Yes | A, COMB |
| L100 | Delivery 4 | Delivery 4 | 2 | Yes | A, COMB |
| L1014 | Delivery 4 | Delivery 4 | 1 | No | A |
| L1021 | Delivery 4 | Delivery 4 | 1 | No | A |
| L1148 | Delivery 4 | Delivery 4 | 1 | No | A |
| L1152 | Delivery 4 | Delivery 4 | 1 | Yes | A, COMB |
| L1155C-2 | Delivery 4 | Delivery 4 | 1 | No | A |
| L1155E | Delivery 4 | Delivery 4 | 1 | No | A |
| L1165 | Delivery 4 | Delivery 4 | 1 | Yes | A, COMB |
| L1197 | Delivery 4 | Delivery 4 | 1 | No | A |
| L1221 | Delivery 4 | Delivery 4 | 1 | No | A |
| L1228 | Delivery 4 | Delivery 4 | 1 | Yes | A, COMB |
| L1251[f] | Delivery 4 | Delivery 4 | 1 | No | A |
| L134A | Delivery 4 | Delivery 4 | 2 | No | A |
| L1355 | Delivery 4 | Delivery 4 | 1 | No | A |
| L1507A | Delivery 4 | Delivery 4 | 2 | No | A |
| L1521-2 | Delivery 4 | Delivery 4 | 2 | No | A |
| L1521B-2 | Delivery 4 | Delivery 4 | 2 | No | A |
| L1521F | Delivery 4 | Delivery 4 | 2 | No | A |
| L1524-4 | Delivery 4 | Delivery 4 | 2 | No | A |
| L158 | Delivery 4 | Delivery 4 | 2 | No | A |
| L1772 | Delivery 4 | Delivery 4 | 2 | No | A |
| L204C-2 | Delivery 4 | Delivery 4 | 2 | No | A |
| L234E | Delivery 4 | Delivery 4 | 2 | No | A |
| L260 | Delivery 4 | Delivery 4 | 2 | Yes | A, COMB |

Table 2—Continued

| Core Name | IRAC[a] | MIPS[a] | Epochs[b] | HDR[c] | IRAC File Code[d] |
|---|---|---|---|---|---|
| L328 | Delivery 4 | Delivery 4 | 2 | No | A |
| L429-C | Delivery 4 | Delivery 4 | 2 | No | A |
| L43 | Delivery 4 | Delivery 4 | 2 | Yes | A, COMB |
| L438 | Delivery 4 | Delivery 4 | 2 | No | A |
| L462-1 | Delivery 4 | Delivery 4 | 2 | No | A |
| L483 | Delivery 4 | Delivery 4 | 2 | Yes | A |
| L492 | Delivery 4 | Delivery 4 | 2 | No | A |
| L63 | Delivery 4 | Delivery 4 | 2 | No | A |
| L673 | Delivery 4 | Delivery 4 | 2 | Yes | A, COMB |
| L673-7 | Delivery 4 | Delivery 4 | 2 | No | A |
| L675 | Delivery 4 | Delivery 4 | 2 | No | A |
| L694-2 | Delivery 4 | Delivery 4 | 2 | No | A |
| L723 | Delivery 4 | Delivery 4 | 1 | Yes | A, COMB |
| Mu8 | Delivery 4 | Delivery 4 | 1 | No | A |
| TMC1[g] | Delivery 4 | Delivery 4 | 2 | No | A |
| TMC2 | Delivery 4 | Delivery 4 | 2 | No | A |

[a]The words "Delivery 4" in the IRAC (MIPS) column indicate that the IRAC (MIPS) data is included in Delivery 4. In previous deliveries this column would sometimes contain "Embargoed" to note data not yet released due to overlap with GTO and GO programs. Since all c2d data is now publicly available, all data on the cores are being delivered.

[b]Indicates how many epochs were observed.

[c]Indicates whether or not high-dynamic range (HDR) IRAC observations were obtained.

[d]All delivered mosaics have file names of the form CoreName_FileCode_Band_mosaic.fits (also mosaic_cov.fits and mosaic_unc.fits). The file code for the IRAC bands is either "A" or "COMB", where "A" indicates that the mosaic is a combination of both epochs for cores observed in two epochs or simply the one epoch for cores observed only in one, and "COMB" indicates that the mosaic is a combination of both the "A" mosaic and the HDR frame. All cores have "A" mosaics delivered, while those observed in HDR mode also have "COMB" mosaics delivered. The file code for the MIPS 24 $\mu$m band is always "A", while the code for the MIPS 70 $\mu$m band is either "BCD" (un-filtered) and "FBCD" (filtered) - both are delivered for each core.

[e]No 70 $\mu$m data were obtained for DC267.4-7.5.

[f]1251 is a combination of the regions called L1251A, L1251C, and L1251E in previous deliveries of c2d data. All mosaics and catalogs for the individual regions have been combined

into one, large region that we refer to as L1251.

[g]TMC1 is a combination of the regions called TMC1 and TMC1-1C in previous deliveries of c2d data. All mosaics and catalogs for the two individual regions have been combined together except the MIPS 70 $\mu$m mosaics, which do not overlap and are thus delivered separately.

Table 3. Data Delivery 4: Stars

| Star Name | IRAC[a] | MIPS[a] | HDR[b] | IRAC File Code[c] | Comments |
|---|---|---|---|---|---|
| CSCha | c2d | c2d | Yes | A, COMB | None |
| DITau | GTO | c2d | Yes | A, COMB | None |
| DoAr21 | map | map | – | – | None |
| FXTau | GTO | c2d | Yes | A, COMB | 160 micron data available |
| GH-V807Tau | GTO | c2d | Yes | A, COMB | None |
| GKTau | GTO | c2d | Yes | A, COMB | None |
| GSC-04590 | c2d | c2d | Yes | A, COMB | None |
| HBC422-423 | GTO | c2d | Yes | A, COMB | None |
| HD283572 | GTO | c2d | Yes | A, COMB | None |
| HH414 | c2d | – | Yes | A, COMB | No MIPS data obtained |
| HVTau | GTO | c2d | Yes | A, COMB | None |
| ITG33 | c2d | c2d | Yes | A, COMB | None |
| IWTau | GTO | c2d | Yes | A, COMB | None |
| LkCa1 | GTO | c2d | Yes | A, COMB | None |
| LkCa14 | GTO | c2d | Yes | A, COMB | None |
| LkCa19 | GTO | c2d | No | A | None |
| LkCa21 | GTO | c2d | Yes | A, COMB | None |
| LkCa3 | GTO | c2d | Yes | A, COMB | None |
| LkCa5 | GTO | c2d | Yes | A, COMB | None |
| LkCa7 | GTO | c2d | Yes | A, COMB | None |
| NTTS032641+2420 | c2d | c2d | Yes | A, COMB | None |
| NTTS040047+2603 | GTO | c2d | Yes | A, COMB | None |
| NTTS040234+2143 | c2d | c2d | Yes | A, COMB | None |
| NTTS041559+1716 | c2d | c2d | Yes | A, COMB | None |
| NTTS042417+1744 | GTO | c2d | Yes | A, COMB | None |
| NTTS042835+1700 | GTO | c2d | Yes | A, COMB | None |
| NTTS042916+1751 | GTO | c2d | Yes | A, COMB | None |
| NTTS042950+1757 | GTO | c2d | Yes | A, COMB | None |
| NTTS043230+1746 | GTO | c2d | Yes | A, COMB | None |
| NTTS045251+3016 | GTO | c2d | No | A | None |
| NTTS162649-2145 | c2d | c2d | Yes | A, COMB | None |
| PZ99_154920 | c2d | c2d | Yes | A, COMB | None |
| PZ99_155506 | c2d | c2d | Yes | A, COMB | None |

Table 3—Continued

| Star Name | IRAC[a] | MIPS[a] | HDR[b] | IRAC File Code[c] | Comments |
|---|---|---|---|---|---|
| PZ99_155702 | c2d | c2d | Yes | A, COMB | None |
| PZ99_160151 | c2d | c2d | Yes | A, COMB | None |
| PZ99_160158 | c2d | c2d | Yes | A, COMB | None |
| PZ99_160253 | c2d | c2d | Yes | A, COMB | None |
| PZ99_160550 | c2d | c2d | Yes | A, COMB | None |
| PZ99_160843 | c2d | c2d | Yes | A, COMB | None |
| PZ99_161019 | c2d | c2d | Yes | A, COMB | None |
| ROX16 | map | map | – | – | None |
| ROX21 | map | map | – | – | None |
| ROX39 | map | map | – | – | None |
| ROX42C | map | map | – | – | None |
| ROX43B-A | map | map | – | – | None |
| ROX47A | map | map | – | – | None |
| ROXR1-23 | map | map | – | – | None |
| ROXR1-35S-N | map | map | – | – | None |
| ROXR1-51A-B | map | map | – | – | None |
| RXJ0405.3+2009 | c2d | c2d | Yes | A, COMB | None |
| RXJ0409.2+1716 | c2d | c2d | Yes | A, COMB | None |
| RXJ0409.8+2446 | c2d | c2d | Yes | A, COMB | None |
| RXJ0412.8+1937 | c2d | c2d | Yes | A, COMB | None |
| RXJ0420.3+3123 | c2d | c2d | Yes | A, COMB | None |
| RXJ0424.8+2643A | c2d | c2d | Yes | A, COMB | None |
| RXJ0432.8+1735 | c2d | c2d | Yes | A, COMB | None |
| RXJ0435.9+2352 | c2d | c2d | Yes | A, COMB | None |
| RXJ0437.4+1851A | c2d | c2d | Yes | A, COMB | None |
| RXJ0438.2+2023 | c2d | c2d | Yes | A, COMB | None |
| RXJ0438.6+1546 | c2d | c2d | Yes | A, COMB | None |
| RXJ0439.4+3332A | c2d | c2d | Yes | A, COMB | None |
| RXJ0445.8+1556 | c2d | c2d | Yes | A, COMB | None |
| RXJ0452.5+1730 | c2d | c2d | Yes | A, COMB | None |
| RXJ0452.8+1621 | c2d | c2d | Yes | A, COMB | None |
| RXJ0457.2+1524 | c2d | c2d | Yes | A, COMB | None |
| RXJ0457.5+2014 | c2d | c2d | Yes | A, COMB | None |

Table 3—Continued

| Star Name | IRAC[a] | MIPS[a] | HDR[b] | IRAC File Code[c] | Comments |
|---|---|---|---|---|---|
| RXJ0458.7+2046 | c2d | c2d | Yes | A, COMB | None |
| RXJ0459.7+1430 | c2d | c2d | Yes | A, COMB | None |
| RXJ0842.4-8345 | c2d | c2d | Yes | A, COMB | None |
| RXJ0848.0-7854 | GTO | c2d | Yes | A, COMB | None |
| RXJ0902.9-7759 | c2d | c2d | Yes | A, COMB | None |
| RXJ0915.5-7609 | c2d | c2d | Yes | A, COMB | None |
| RXJ0935.0-7804 | c2d | c2d | Yes | A, COMB | None |
| RXJ0942.7-7726 | c2d | c2d | Yes | A, COMB | None |
| RXJ1001.1-7913 | c2d | c2d | Yes | A, COMB | None |
| RXJ1005.3-7749 | c2d | c2d | Yes | A, COMB | None |
| RXJ1108.8-7519 | c2d | c2d | Yes | A, COMB | None |
| RXJ1109.4-7627 | c2d | c2d | Yes | A, COMB | None |
| RXJ1117.0-8028 | c2d | c2d | Yes | A, COMB | None |
| RXJ1123.2-7924 | c2d | c2d | Yes | A, COMB | None |
| RXJ1129.2-7546 | c2d | c2d | Yes | A, COMB | None |
| RXJ1149.8-7850 | c2d | c2d | Yes | A, COMB | None |
| RXJ1150.4-7704 | c2d | c2d | Yes | A, COMB | None |
| RXJ1158.5-7754 | c2d | GTO | Yes | A, COMB | None |
| RXJ1158.5-7913 | c2d | c2d | Yes | A, COMB | None |
| RXJ1159.7-7601 | c2d | – | Yes | A, COMB | No MIPS data obtained |
| RXJ1202.1-7853 | c2d | c2d | Yes | A, COMB | None |
| RXJ1204.6-7731 | c2d | c2d | Yes | A, COMB | None |
| RXJ1216.8-7753 | c2d | c2d | Yes | A, COMB | None |
| RXJ1219.7-7403 | c2d | c2d | Yes | A, COMB | None |
| RXJ1220.4-7407 | c2d | c2d | Yes | A, COMB | None |
| RXJ1239.4-7502 | c2d | c2d | Yes | A, COMB | None |
| RXJ1243.1-7458 | c2d | c2d | Yes | A, COMB | None |
| RXJ1301.0-7654 | c2d | c2d | Yes | A, COMB | None |
| RXJ1507.6-4603 | c2d | c2d | Yes | A, COMB | None |
| RXJ1508.6-4423 | c2d | c2d | Yes | A, COMB | None |
| RXJ1511.6-3550 | c2d | c2d | Yes | A, COMB | None |
| RXJ1514.0-4629 | c2d | c2d | Yes | A, COMB | None |
| RXJ1515.8-3331 | c2d | c2d | Yes | A, COMB | None |

Table 3—Continued

| Star Name | IRAC[a] | MIPS[a] | HDR[b] | IRAC File Code[c] | Comments |
|---|---|---|---|---|---|
| RXJ1515.9-4418 | c2d | c2d | Yes | A, COMB | None |
| RXJ1516.6-4406 | c2d | c2d | Yes | A, COMB | None |
| RXJ1518.9-4050 | c2d | c2d | Yes | A, COMB | None |
| RXJ1519.3-4056 | c2d | c2d | Yes | A, COMB | None |
| RXJ1522.2-3959 | c2d | c2d | Yes | A, COMB | None |
| RXJ1523.4-4055 | c2d | c2d | Yes | A, COMB | None |
| RXJ1523.5-3821 | c2d | c2d | Yes | A, COMB | None |
| RXJ1524.0-3209 | c2d | c2d | Yes | A, COMB | None |
| RXJ1524.5-3652 | c2d | c2d | Yes | A, COMB | None |
| RXJ1525.5-3613 | c2d | c2d | Yes | A, COMB | None |
| RXJ1525.6-3537 | c2d | c2d | Yes | A, COMB | None |
| RXJ1526.0-4501 | c2d | c2d | Yes | A, COMB | None |
| RXJ1538.0-3807 | c2d | c2d | Yes | A, COMB | None |
| RXJ1538.6-3916 | c2d | c2d | Yes | A, COMB | None |
| RXJ1538.7-4411 | c2d | c2d | Yes | A, COMB | None |
| RXJ1540.7-3756 | c2d | c2d | Yes | A, COMB | None |
| RXJ1543.1-3920 | c2d | c2d | Yes | A, COMB | None |
| RXJ1546.7-3618 | c2d | c2d | Yes | A, COMB | None |
| RXJ1547.7-4018 | c2d | c2d | Yes | A, COMB | None |
| RXJ1550.0-3629 | c2d | c2d | Yes | A, COMB | None |
| RXJ1552.3-3819 | c2d | c2d | Yes | A, COMB | None |
| RXJ1554.9-3827 | c2d | c2d | Yes | A, COMB | None |
| RXJ1555.4-3338 | c2d | c2d | Yes | A, COMB | None |
| RXJ1555.6-3709 | c2d | c2d | Yes | A, COMB | None |
| RXJ1556.1-3655 | c2d | c2d | Yes | A, COMB | None |
| RXJ1559.0-3646 | c2d | c2d | Yes | A, COMB | None |
| RXJ1559.8-3628 | c2d | GTO | Yes | A, COMB | None |
| RXJ1601.2-3320 | c2d | c2d | Yes | A, COMB | None |
| RXJ1602.0-3613 | c2d | c2d | Yes | A, COMB | None |
| RXJ1603.2-3239 | c2d | c2d | Yes | A, COMB | None |
| RXJ1603.8-3938 | c2d | c2d | Yes | A, COMB | None |
| RXJ1603.8-4355 | c2d | GTO | Yes | A, COMB | None |
| RXJ1604.5-3207 | c2d | c2d | Yes | A, COMB | None |

Table 3—Continued

| Star Name | IRAC[a] | MIPS[a] | HDR[b] | IRAC File Code[c] | Comments |
|---|---|---|---|---|---|
| RXJ1605.6-3837 | c2d | c2d | Yes | A, COMB | None |
| RXJ1607.2-3839 | c2d | c2d | Yes | A, COMB | None |
| RXJ1608.3-3843 | c2d | c2d | Yes | A, COMB | None |
| RXJ1608.5-3847 | c2d | c2d | Yes | A, COMB | None |
| RXJ1608.6-3922 | c2d | c2d | Yes | A, COMB | None |
| RXJ1609.7-3854 | map | c2d | – | – | None |
| RXJ1610.1-4016 | c2d | c2d | Yes | A, COMB | None |
| RXJ1612.0-1906a | c2d | c2d | Yes | A, COMB | None |
| RXJ1612.1-1915 | c2d | c2d | Yes | A, COMB | None |
| RXJ1612.3-1909 | c2d | c2d | Yes | A, COMB | None |
| RXJ1612.6-1924 | c2d | c2d | Yes | A, COMB | None |
| RXJ1613.0-4004 | c2d | c2d | Yes | A, COMB | None |
| RXJ1613.1-1904a | c2d | c2d | Yes | A, COMB | None |
| RXJ1613.7-1926 | c2d | c2d | Yes | A, COMB | None |
| RXJ1613.8-1835 | c2d | c2d | Yes | A, COMB | None |
| RXJ1613.9-1848 | c2d | c2d | Yes | A, COMB | None |
| RXJ1614.2-1938 | c2d | c2d | Yes | A, COMB | None |
| RXJ1614.4-1857a | c2d | c2d | Yes | A, COMB | None |
| RXJ1615.1-1851 | c2d | c2d | Yes | A, COMB | None |
| RXJ1615.3-3255 | c2d | c2d | Yes | A, COMB | None |
| RXJ1621.2-2342 | map | c2d | – | – | None |
| RXJ1621.2-2347 | map | c2d | – | – | None |
| RXJ1621.4-2312 | map | c2d | – | – | None |
| RXJ1622.6-2345 | map | c2d | – | – | None |
| RXJ1622.7-2325a | map | c2d | – | – | None |
| RXJ1622.8-2333 | map | c2d | – | – | None |
| RXJ1623.5-3958 | c2d | c2d | Yes | A, COMB | None |
| RXJ1623.8-2341 | map | c2d | – | – | None |
| RXJ1624.0-2456 | c2d | c2d | Yes | A, COMB | None |
| RXJ1624.8-2359 | map | c2d | – | – | None |
| RXJ1625.2-2455 | map | c2d | – | – | None |
| SR8 | map | c2d | – | – | None |
| SR9 | map | map | – | – | None |

Table 3—Continued

| Star Name | IRAC[a] | MIPS[a] | HDR[b] | IRAC File Code[c] | Comments |
|---|---|---|---|---|---|
| Sz117 | map | c2d | – | – | None |
| Sz129 | c2d | c2d | Yes | A, COMB | None |
| Sz30 | GTO | c2d | Yes | A, COMB | 160 micron data available |
| Sz41 | – | c2d | – | – | IRAC observations done at wrong coordinates |
| Sz65 | map | c2d | – | – | None |
| Sz76 | c2d | c2d | Yes | A, COMB | None |
| Sz77 | c2d | c2d | Yes | A, COMB | None |
| Sz81 | c2d | c2d | Yes | A, COMB | None |
| Sz82 | c2d | c2d | Yes | A, COMB | 160 micron data available |
| Sz84 | c2d | c2d | Yes | A, COMB | None |
| Sz96 | map | c2d | – | – | None |
| Sz98 | map | c2d | – | – | None |
| TCha | c2d | – | Yes | A, COMB | No MIPS data obtained |
| UXTau | GTO | c2d | Yes | A, COMB | None |
| V710Tau | – | c2d | – | – | No IRAC data obtained, 160 micron data available |
| V830Tau | GTO | c2d | Yes | A, COMB | None |
| V836Tau | c2d | c2d | Yes | A, COMB | None |
| V927Tau | GTO | c2d | Yes | A, COMB | None |
| V928Tau | GTO | c2d | Yes | A, COMB | None |
| WaOph1 | c2d | c2d | Yes | A, COMB | None |
| WaOph2 | c2d | c2d | Yes | A, COMB | None |
| WaOph6 | c2d | c2d | Yes | A, COMB | None |
| WaTau-1 | – | c2d | – | – | No IRAC data obtained |
| ZZTau | GTO | c2d | Yes | A, COMB | None |

[a]If the following appears in the "IRAC" column, it applies to the IRAC data, and if it appears in the "MIPS" column, it applies to the MIPS data:
c2d: The data were obtained in the c2d program and are included as part of the fourth data delivery.
GTO: The data were obtained in a GTO program and are included as part of the fourth data delivery.
map: The data are included in one of the c2d large cloud maps.

[b]Indicates whether or not high-dynamic range (HDR) IRAC observations were obtained.

[c]All delivered mosaics have file names of the form StarName_FileCode_Band_mosaic.fits (also mo-

saic_cov.fits and mosaic_unc.fits). The file code for the IRAC bands is either "A" or "COMB", where "A" indicates that the mosaic is a combination of both epochs for stars observed in two epochs or simply the one epoch for stars observed only in one, and "COMB" indicates that the mosaic is a combination of both the "A" mosaic and the HDR frame. All stars have "A" mosaics delivered, while those observed in HDR mode also have "COMB" mosaics delivered. The file code for the MIPS 24 $\mu$m band is always "A", while the code for the MIPS 70 and 160 $\mu$m bands is either "BCD" (un-filtered) and "FBCD" (filtered) - both are delivered for each star. All stars have 70 $\mu$m data mosaics delivered, but only 4 stars have 160 $\mu$m mosaics delivered.

Table 4. Cloud Areas for IRAC Mosaics

| Cloud[a] | Area Name | RA | Dec |
|---|---|---|---|
| ChamaeleonII | CHA_II | 194.7594 | −77.4105 |
| ChamaeleonII/IRAC/Off | CHA_II_OC1 | 204.4745 | −75.9830 |
| ChamaeleonII/IRAC/Off | CHA_II_OC2 | 204.5106 | −77.9832 |
| ChamaeleonII/IRAC/Off | CHA_II_OC3 | 204.5635 | −79.9835 |
| ChamaeleonII/IRAC/Off | CHA_II_OC4 | 179.5086 | −77.5090 |
| ChamaeleonII/IRAC/Off | CHA_II_OC5 | 179.5316 | −78.5090 |
| ChamaeleonII/IRAC/Off | CHA_II_OC6 | 179.6091 | −81.0089 |
| Lupus | LUP_I | 235.3558 | −34.1898 |
| Lupus | LUP_III | 242.6689 | −38.6252 |
| Lupus | LUP_IV | 240.4057 | −41.9442 |
| Lupus/Off | LUP_OC1 | 243.2380 | −34.0561 |
| Lupus/Off | LUP_OC2 | 249.9925 | −40.5565 |
| Lupus/IRAC/Off | LUP_OC3 | 237.4820 | −41.0553 |
| Lupus/IRAC/Off | LUP_OC4 | 241.7350 | −43.0559 |
| Ophiuchus | OPH_NORTH | 251.1640 | −21.5131 |
| Ophiuchus | OPH_L1689 | 249.2739 | −24.4823 |
| Ophiuchus | OPH_L1688 | 246.5224 | −24.0018 |
| Ophiuchus | OPH_ALL | 245.8928 | −23.8842 |
| Ophiuchus/IRAC/Off | OPH_OC1 | 247.8845 | −21.1105 |
| Ophiuchus/IRAC/Off | OPH_OC2 | 245.8845 | −22.4440 |
| Ophiuchus/IRAC/Off | OPH_OC3 | 250.3828 | −23.1937 |
| Ophiuchus/IRAC/Off | OPH_OC4 | 252.0910 | −24.9437 |
| Ophiuchus/IRAC/Off | OPH_OC5 | 250.0094 | −25.9442 |
| Ophiuchus/IRAC/Off | OPH_OC6 | 245.8865 | −25.9442 |
| Perseus | PER_E | 55.4849 | 32.0074 |
| Perseus | PER_W | 52.3931 | 30.9275 |
| Perseus | PER_ALL | 53.8944 | 31.5488 |
| Perseus/IRAC/Off | PER_OC1 | 55.8569 | 34.0548 |
| Perseus/IRAC/Off | PER_OC2 | 52.4801 | 33.0543 |
| Perseus/IRAC/Off | PER_OC3 | 48.3531 | 31.5537 |
| Perseus/IRAC/Off | PER_OC4 | 55.8588 | 29.5550 |
| Perseus/IRAC/Off | PER_OC5 | 52.4823 | 28.0546 |
| Perseus/IRAC/Off | PER_OC6 | 48.3554 | 27.0541 |

Table 4—Continued

| Cloud[a] | Area Name | RA | Dec |
|---|---|---|---|
| Serpens | SER | 277.3328 | 0.6129 |
| Serpens/Off | SER_OC1 | 279.9935 | 4.0564 |
| Serpens/IRAC/Off | SER_OC2 | 273.2431 | 3.0564 |
| Serpens/IRAC/Off | SER_OC3 | 274.9933 | 2.0564 |
| Serpens/IRAC/Off | SER_OC4 | 270.7434 | −0.9434 |
| Serpens/IRAC/Off | SER_OC5 | 279.9933 | −2.4434 |
| Serpens/IRAC/Off | SER_OC6 | 273.7440 | −5.4436 |
| Serpens/IRAC/Off | SER_OC7 | 275.4936 | −1.4434 |
| Serpens/IRAC/Off | SER_OC8 | 268.2431 | 0.5564 |

[a]CloudName/IRAC/Off indicates that the off-cloud region is only observed with IRAC, whereas CloudName/Off indicates that the off-cloud region is observed with both IRAC and MIPS.

Table 5. Cloud Areas for MIPS Mosaics

| Cloud[a] | Area Name | RA | Dec |
|---|---|---|---|
| ChamaeleonII | CHA_II | 195.2732 | −77.4225 |
| Lupus | LUP_I | 235.3765 | −34.1526 |
| Lupus | LUP_III | 242.6509 | −38.6068 |
| Lupus | LUP_IV | 240.3672 | −41.9258 |
| Lupus/Off | LUP_OC1 | 243.2254 | −34.0275 |
| Lupus/Off | LUP_OC2 | 249.9765 | −40.5293 |
| Ophiuchus | OPH_NORTH | 251.1986 | −21.6318 |
| Ophiuchus[b] | OPH_L1689 | 250.0436 | −24.3564 |
| Ophiuchus[b] | OPH_L1688E | 247.4341 | −24.1376 |
| Ophiuchus[b] | OPH_L1688W | 245.7378 | −23.7490 |
| Ophiuchus[b] | OPH_ALL | 248.2842 | −24.2464 |
| Ophiuchus/MIPS/Off | OPH_OC7 | 245.9906 | −21.9335 |
| Ophiuchus/MIPS/Off | OPH_OC8 | 245.8257 | −26.4537 |
| Perseus[c] | PER_E | 56.0454 | 32.1931 |
| Perseus[c] | PER_M | 53.8989 | 31.2434 |
| Perseus[c] | PER_W | 52.0859 | 30.5904 |
| Perseus[c] | PER_ALL | 54.3021 | 31.26634 |
| Serpens | SER | 277.2773 | 0.71380 |
| Serpens/Off | SER_OC1 | 280.0125 | 4.03160 |

[a]CloudName/MIPS/Off indicates that the off-cloud region is only observed with MIPS, whereas CloudName/Off indicates that the off-cloud region is observed with both MIPS and IRAC.

[b]These sub-regions only apply to the MIPS 24 $\mu$m band. For the 70 and 160 $\mu$m bands, the total coverage is split into two mosaics: OPH_L1688 and OPH_L1689. There is no combined mosaic of the full region at these wavelengths.

[c]These sub-regions only apply to the MIPS 24 $\mu$m band. For the 70 and 160 $\mu$m bands, there is only one mosaic covering the full region: PER_ALL.

Table 6: Mean Number of Bad Pixels in IRAC Images

| Mask | 3.6 $\mu$m | 4.5 $\mu$m | 5.8 $\mu$m | 8.0 $\mu$m |
|---|---|---|---|---|
| pmask+dmask | 396 | 439 | 628 | 691 |
| c2dmask | 408 | 451 | 635 | 695 |

[a]The pmasks account for 295, 393, 604, and 667 bad pixels in Bands 1–4, respectively.

Table 7: Typical Percentage of IRAC Short-Exposure BCD Images with Artifacts

| | IRAC Band | | | |
|---|---|---|---|---|
| Source | 3.6 $\mu$m | 4.5 $\mu$m | 5.8 $\mu$m | 8.0 $\mu$m |
| Muxbleed | 70 | 10 | - | - |
| Column Pulldown | 0 | 0 | 0 | 0 |
| Banding | - | - | 10 | 10 |

Table 8: Typical Percentage of IRAC Long-Exposure BCD Images with Artifacts

| | IRAC Band | | | |
|---|---|---|---|---|
| Source | 3.6 $\mu$m | 4.5 $\mu$m | 5.8 $\mu$m | 8.0 $\mu$m |
| Muxbleed | 100 | 90 | - | - |
| Column Pulldown | 70 | 60 | 20 | 30 |
| Banding | - | - | 20 | 50 |

Table 9: Effects of Location-Dependent Corrections on Fluxes

| Band | Relative Flux[a] |
|---|---|
| IRAC1 | $1.005 \pm 0.008$ |
| IRAC2 | $1.005 \pm 0.008$ |
| IRAC3 | $1.02 \pm 0.01$ |
| IRAC4 | $1.02 \pm 0.02$ |

[a] Corrected pixel value relative to the non-corrected value. Here, an estimate of the mode is given, along with an estimate of the 1-$\sigma$ dispersion based on the width of the distribution with values at least half that of the distribution peak.

Table 10: Effects of Location-Dependent Corrections on Colors

| Color | Relative Color[a] |
|---|---|
| IRAC1/IRAC2 | 0.995 ± 0.006 |
| IRAC3/IRAC4 | 1.04 ± 0.06 |
| IRAC1/IRAC3 | 0.99 ± 0.04 |
| IRAC2/IRAC4 | 1.00 ± 0.02 |

[a] Corrected ratio of pixel values relative to the non-corrected ratio. Here, an estimate of the mode is given, along with an estimate of the 1-$\sigma$ dispersion based on the width of the distribution with values at least half that of the distribution peak.

Table 11: Description of Image types from source extraction: IRAC and MIPS1

| Code | Meaning |
|---|---|
| −2 | Source for which a flux has been band-filled at a fixed position |
| −1 | Source extracted from the high dynamic range data |
| 0 | Source located too close to the edge to have a reliable fit in even one bcd/icd frame |
| 1 | Source that was well fitted by a point source profile |
| 2 | Source that was found to be extended and was fitted by a 2-axis ellipsoid |
| 3 | Source that was found to be better fit as a component of a close double than as an extended source |
| 4 | Source failed to converge in four-parameter fitting (flux, background, and x/y position) |
| 5 | Due to nearby bad pixels, there were too few points available to attempt a shape/size fit; source was assumed to be a point source. |
| 6 | Too few points to attempt a four-parameter fit; object not subtracted from image |
| 7 | Source that had too low S/N to be tested for shape; parameters represent results from assuming it was a point source |
| 8 | Object that was best fitted by single high pixel; possibly a cosmic ray hit (no photometry) |
| 9 | Object that was found to be narrower than a point source; possibly a cosmic ray hit |

Table 12: Description of Image types from source extraction for MIPS2 Only

| Code | Meaning |
|---|---|
| 0 | Nominal |
| 1 | Saturated, but a fitted value was inserted using the wings of the PSF. |
| 2 | Extended source. The flux may be unreliable since PSF fitting was used. |
| 3 | Bad saturation. The fluxes are unreliable, but the source is listed for completeness. |

Table 13: Object types

| Object type | Description |
|---|---|
| Sources detected in 0-2 bands or in 2MASS only | |
| Zero | detected in one epoch only |
| 2mass | 2MASS source without Spitzer detections |
| one | detected in only one band between IRAC1-IRAC3 |
| two | detected in two bands, but not in IRAC4 and MIPS1 |
| red1 | detected in IRAC4 or MIPS1 only |
| red2 | detected in only IRAC4 and MIPS1 |
| Stars | |
| star | main sequence or giant stars |
| Source fits specific templates | |
| PAH-em | [3.6]-[4.5]<0.6, 1.5<[5.8]-[8.0] |
| star+dust(BAND) | star plus dust component longward of BAND |
| red | MIPS1 flux > 3 times the nearest IRAC band flux |
| Sources associated with clouds | |
| YSOc | YSO candidate |
| YSOc_PAH-em | YSO candidate and PAH-em |
| YSOc_star+dust(BAND) | YSO candidate and star+dust(BAND) |
| YSOc_red | YSO candidate and red |
| Background galaxy sources | |
| Galc | Galaxy candidate |
| Galc_PAH-em | Galaxy candidate and PAH-em |
| Galc_star+dust(BAND) | Galaxy candidate and star+dust(BAND) |
| Galc_red | Galaxy candidate and red |
| Sources classified according to SED morphology | |
| rising | none of the above, but with rising SED |
| falling | none of the above, but with falling SED |
| flat | none of the above, but with flat SED |
| cup-up | none of the above, but with concave SED |
| cup-down | none of the above, but with convex SED |

Table 14: Description of source-dependent columns in the catalog table

| Column Name | Definition | Data Type |
|---|---|---|
| c2d_ID | SSTc2d Object Identifier | Char |
| RA | Weighted average J2000 Right Ascension for source in degrees | Real |
| D_RA | Uncertainty in RA source position | Real |
| DEC | Weighted average J2000 Declination for source in degrees | Real |
| D_DEC | Uncertainty in Dec source position | Real |
| Q_pos | Flag which indicates the quality of the position agreement between bands. Grades A,B,C,D,or Q are assigned as described in §2.4.5 | Char |
| Q_merge | Flag which indicates the overall quality of the source, combining position and flux information in the form of grades A,B,C,D, or Q as described in §2.4.5 | Char |
| Log(Prob_Galc) | Probability that object is a galaxy (§2.5.4) | Real |
| alpha | Power-law index from a fit to IRAC fluxes where possible | Real |
| D_alpha | Uncertainty in the power-law index | Real |
| alpha_chi2 | Value of $\chi^2$ from power-law fit to IRAC detections | Real |
| alpha_nfit | Number of IRAC detections used in computing the power-law index | Real |
| object_type | Classifications of the source nature (§2.5) | Char |
| Av | Magnitudes of visual extinction (§2.5.2) | Real |
| D_Av | Uncertainty in the extinction (§2.5.2) | Real |
| mag_IR1 | Unextincted IRAC1 apparent magnitude (§2.5.2) | Real |
| D_mag_IR1 | Uncertainty in the Unextincted IRAC1 mag. (§2.5.2) | Real |
| Av_chi2 | $\chi^2$ from computing $A_V$ (§2.5.2) | Real |
| Av_nfit | Number of bands used to fit alpha (§2.5.2) | Real |

Note. — Details of quality assessment flag values and their derivation are given in Section 2.4

Table 15: Band-dependent column names

| Column Name | Definition | Data Type |
|---|---|---|
| <Band>_flux_<#> | Flux in a single Spitzer <Band> derived from one or more epochs | Real |
| <Band>_D_flux_<#> | Uncertainty in the single-band flux value | Real |
| <Band>_date_<#> | Mean date of observation | Real |
| <Band>_Q_det_<#> | Quality of detection based on signal to noise and given letter grades A,B,C,D,E,K,Y,U, or N as defined in §2.4.5 | Char |
| <Band>_Q_flux_m | A measure of the agreement between fluxes observed at two separate epochs. Grades A-E or Q are defined as in §2.4.5 | Char |
| <Band>_imtype | Numerical code from the original point source extraction. Takes on values −2 to 9 as defined in Table 11 | Int |
| <Band>_src_area | Area of source determined by original point source extraction as described in §refextract | Real |
| <Band>_amajor | Major axis of the source shape as determined by original point source extraction (§2.3.2) | Real |
| <Band>_aminor | Minor axis of the source shape as determined by original point source extraction (§2.3.2) | Real |
| <Band>_tilt | Angle of orientation for point source ellipse as described in §2.3.2 | Real |

Note. — "<Band>" can take on character values, "J, H, Ks, IR1, IR2, IR3, IR4, MP1, or MP2. " "<#>" can take on character values "1,2, or c". Details of quality assessment flags and code designations are given in Section 2.4.

Table 16. Description of Columns in Catalog

| Column Number | Column Name | Description | Null Value | Reference |
|---|---|---|---|---|
| 1 | c2d_ID | Source name | null[a] | ... |
| 2 | RA | Right Ascension [deg; J2000] | −999[a] | §2.4.1,2.4.2 |
| 3 | D_RA | Uncertainty in RA [deg] | −999[a] | §2.4.1,2.4.2 |
| 4 | DEC | Declination [deg; J2000] | −999[a] | §2.4.1,2.4.2 |
| 5 | D_DEC | Uncertainty in DEC [deg] | − 999[a] | §2.4.1,2.4.2 |
| 6 | Q_pos | Quality of position | Q | §2.4.5 |
| 7 | Q_merge | Quality of merge (Overall source quality) | null[a] | §2.4.5 |
| 8 | 2MASS_name | Source identification in 2MASS PSC | null | §2.3.2 |
| 9 | Log(Prob_Galc) | Probability that source is a galaxy | 999 | §2.5.4 |
| 10 | alpha | Source spectral index | −999 | §2.4.6 |
| 11 | D_alpha | Uncertainty in alpha | −999 | §2.4.6 |
| 12 | alpha_chi2 | $\chi^2$ from computing alpha | −999 | §2.4.6 |
| 13 | alpha_nfit | Number of bands used to fit alpha | 0 | §2.4.6 |
| 14 | object_type | Source classification | null[a] | §2.5 |
| 15 | Av | Visual extinction [mag] | −999 | §2.5.2 |
| 16 | D_Av | Uncertainty in Av [mag] | −999 | §2.5.2 |
| 17 | mag_IR1 | Unextincted IRAC1 magnitude [mag] | −999 | §2.5.2 |
| 18 | D_mag_IR1 | Uncertainty in mag_IR1 [mag] | −999 | §2.5.2 |
| 19 | Av_chi2 | $\chi^2$ from computing Av | −999 | §2.5.2 |
| 20 | Av_nfit | Number of bands used to fit Av | 0 | §2.5.2 |
| 21 | J_flux_c | 2MASS $J$ flux [mJy] | −999 | §2.3.2 |
| 22 | J_D_flux_c | Uncertainty in 2MASS $J$ flux [mJy] | −999 | §2.3.2 |
| 23 | J_date_c | Date of 2MASS $J$ observation | null | §2.3.2 |
| 24 | J_Q_det_c | Quality of 2MASS $J$ detection | null | §2.4.5 |
| 25 | H_flux_c | 2MASS $H$ flux [mJy] | −999 | §2.3.2 |
| 26 | H_D_flux_c | Uncertainty in 2MASS $H$ flux [mJy] | −999 | §2.3.2 |
| 27 | H_date_c | Date of 2MASS $H$ observation | null | §2.3.2 |
| 28 | H_Q_det_c | Quality of 2MASS $H$ detection | null | §2.4.5 |
| 29 | Ks_flux_c | 2MASS $K_s$ flux [mJy] | −999 | §2.3.2 |
| 30 | Ks_D_flux_c | Uncertainty in 2MASS $K_s$ flux [mJy] | −999 | §2.3.2 |
| 31 | Ks_date_c | Date of 2MASS $K_s$ observation | null | §2.3.2 |
| 32 | Ks_Q_det_c | Quality of 2MASS $K_s$ detection | null | §2.4.5 |

Table 16—Continued

| Column Number | Column Name | Description | Null Value | Reference |
|---|---|---|---|---|
| 33 | IR1_flux_1 | IRAC1 flux, Epoch 1 [mJy] | −999 | §2.3.2 |
| 34 | IR1_D_flux_1 | Uncertainty in IRAC1 flux, Epoch 1 [mJy] | −999 | §2.3.2 |
| 35 | IR1_date_1 | Date of IRAC1 observation, Epoch 1 | null | §2.3.2 |
| 36 | IR1_Q_det_1 | Quality of IRAC1 detection, Epoch 1 | null | §2.4.5 |
| 37 | IR1_flux_2 | IRAC1 flux, Epoch 2 [mJy] | −999 | §2.3.2 |
| 38 | IR1_D_flux_2 | Uncertainty in IRAC1 flux, Epoch 2 [mJy] | −999 | §2.3.2 |
| 39 | IR1_date_2 | Date of IRAC1 observation, Epoch 2 | null | §2.3.2 |
| 40 | IR1_Q_det_2 | Quality of IRAC1 detection, Epoch 2 | null | §2.4.5 |
| 41 | IR1_flux_c | IRAC1 flux, combined epochs [mJy] | −999 | §2.3.2 |
| 42 | IR1_D_flux_c | Uncertainty in IRAC1 flux, combined epochs [mJy] | −999 | §2.3.2 |
| 43 | IR1_date_c | Date of IRAC1 observation, combined epochs | null | §2.3.2 |
| 44 | IR1_Q_det_c | Quality of IRAC1 detection, combined epochs | null | §2.4.5 |
| 45 | IR1_Q_flux_m | Quality of IRAC1 flux match | Q | §2.4.5 |
| 46 | IR1_imtype | Image type from IRAC1 source extraction | null | Table 11 |
| 47 | IR1_src_area | Area of IRAC1 source [pixel$^2$] | −999 | §2.3.2 |
| 48 | IR1_amajor | Length of IRAC1 source major axis [pixel] | −999 | §2.3.2 |
| 49 | IR1_aminor | Length of IRAC1 source minor axis [pixel] | −999 | §2.3.2 |
| 50 | IR1_tilt | Tilt angle for IRAC1 [deg] | −999 | §2.3.2 |
| 51 | IR2_flux_1 | IRAC2 flux, Epoch 1 [mJy] | −999 | §2.3.2 |
| 52 | IR2_D_flux_1 | Uncertainty in IRAC2 flux, Epoch 1 [mJy] | −999 | §2.3.2 |
| 53 | IR2_date_1 | Date of IRAC2 observation, Epoch 1 | null | §2.3.2 |
| 54 | IR2_Q_det_1 | Quality of IRAC2 detection, Epoch 1 | null | §2.4.5 |
| 55 | IR2_flux_2 | IRAC2 flux, Epoch 2 [mJy] | −999 | §2.3.2 |
| 56 | IR2_D_flux_2 | Uncertainty in IRAC2 flux, Epoch 2 [mJy] | −999 | §2.3.2 |
| 57 | IR2_date_2 | Date of IRAC2 observation, Epoch 2 | null | §2.3.2 |
| 58 | IR2_Q_det_2 | Quality of IRAC2 detection, Epoch 2 | null | §2.4.5 |
| 59 | IR2_flux_c | IRAC2 flux, combined epochs [mJy] | −999 | §2.3.2 |
| 60 | IR2_D_flux_c | Uncertainty in IRAC2 flux, combined epochs [mJy] | −999 | §2.3.2 |
| 61 | IR2_date_c | Date of IRAC2 observation, combined epochs | null | §2.3.2 |
| 62 | IR2_Q_det_c | Quality of IRAC2 detection, combined epochs | null | §2.4.5 |
| 63 | IR2_Q_flux_m | Quality of IRAC2 flux match | Q | §2.4.5 |
| 64 | IR2_imtype | Image type from IRAC2 source extraction | null | Table 11 |

Table 16—Continued

| Column Number | Column Name | Description | Null Value | Reference |
|---|---|---|---|---|
| 65 | IR2_src_area | Area of IRAC2 source [pixel$^2$] | −999 | §2.3.2 |
| 66 | IR2_amajor | Length of IRAC2 source major axis [pixel] | −999 | §2.3.2 |
| 67 | IR2_aminor | Length of IRAC2 source minor axis [pixel] | −999 | §2.3.2 |
| 68 | IR2_tilt | Tilt angle for IRAC2 [deg] | −999 | §2.3.2 |
| 69 | IR3_flux_1 | IRAC3 flux, Epoch 1 [mJy] | −999 | §2.3.2 |
| 70 | IR3_D_flux_1 | Uncertainty in IRAC3 flux, Epoch 1 [mJy] | −999 | §2.3.2 |
| 71 | IR3_date_1 | Date of IRAC3 observation, Epoch 1 | null | §2.3.2 |
| 72 | IR3_Q_det_1 | Quality of IRAC3 detection, Epoch 1 | null | §2.4.5 |
| 73 | IR3_flux_2 | IRAC3 flux, Epoch 2 [mJy] | −999 | §2.3.2 |
| 74 | IR3_D_flux_2 | Uncertainty in IRAC3 flux, Epoch 2 [mJy] | −999 | §2.3.2 |
| 75 | IR3_date_2 | Date of IRAC3 observation, Epoch 2 | null | §2.3.2 |
| 76 | IR3_Q_det_2 | Quality of IRAC3 detection, Epoch 2 | null | §2.4.5 |
| 77 | IR3_flux_c | IRAC3 flux, combined epochs [mJy] | −999 | §2.3.2 |
| 78 | IR3_D_flux_c | Uncertainty in IRAC3 flux, combined epochs [mJy] | −999 | §2.3.2 |
| 79 | IR3_date_c | Date of IRAC3 observation, combined epochs | null | §2.3.2 |
| 80 | IR3_Q_det_c | Quality of IRAC3 detection, combined epochs | null | §2.4.5 |
| 81 | IR3_Q_flux_m | Quality of IRAC3 flux match | Q | §2.4.5 |
| 82 | IR3_imtype | Image type from IRAC3 source extraction | null | Table 11 |
| 83 | IR3_src_area | Area of IRAC3 source [pixel$^2$] | −999 | §2.3.2 |
| 84 | IR3_amajor | Length of IRAC3 source major axis [pixel] | −999 | §2.3.2 |
| 85 | IR3_aminor | Length of IRAC3 source minor axis [pixel] | −999 | §2.3.2 |
| 86 | IR3_tilt | Tilt angle for IRAC3 [deg] | −999 | §2.3.2 |
| 87 | IR4_flux_1 | IRAC4 flux, Epoch 1 [mJy] | −999 | §2.3.2 |
| 88 | IR4_D_flux_1 | Uncertainty in IRAC4 flux, Epoch 1 [mJy] | −999 | §2.3.2 |
| 89 | IR4_date_1 | Date of IRAC4 observation, Epoch 1 | null | §2.3.2 |
| 90 | IR4_Q_det_1 | Quality of IRAC4 detection, Epoch 1 | null | §2.4.5 |
| 91 | IR4_flux_2 | IRAC4 flux, Epoch 2 [mJy] | −999 | §2.3.2 |
| 92 | IR4_D_flux_2 | Uncertainty in IRAC4 flux, Epoch 2 [mJy] | −999 | §2.3.2 |
| 93 | IR4_date_2 | Date of IRAC4 observation, Epoch 2 | null | §2.3.2 |
| 94 | IR4_Q_det_2 | Quality of IRAC4 detection, Epoch 2 | null | §2.4.5 |
| 95 | IR4_flux_c | IRAC4 flux, combined epochs [mJy] | −999 | §2.3.2 |
| 96 | IR4_D_flux_c | Uncertainty in IRAC4 flux, combined epochs [mJy] | −999 | §2.3.2 |

Table 16—Continued

| Column Number | Column Name | Description | Null Value | Reference |
|---|---|---|---|---|
| 97 | IR4_date_c | Date of IRAC4 observation, combined epochs | null | §2.3.2 |
| 98 | IR4_Q_det_c | Quality of IRAC4 detection, combined epochs | null | §2.4.5 |
| 99 | IR4_Q_flux_m | Quality of IRAC4 flux match | Q | §2.4.5 |
| 100 | IR4_imtype | Image type from IRAC4 source extraction | null | Table 11 |
| 101 | IR4_src_area | Area of IRAC4 source [pixel$^2$] | −999 | §2.3.2 |
| 102 | IR4_amajor | Length of IRAC4 source major axis [pixel] | −999 | §2.3.2 |
| 103 | IR4_aminor | Length of IRAC4 source minor axis [pixel] | −999 | §2.3.2 |
| 104 | IR4_tilt | Tilt angle for IRAC4 [deg] | −999 | §2.3.2 |
| 105 | MP1_flux_1 | MIPS1 flux, Epoch 1 [mJy] | −999 | §2.3.2 |
| 106 | MP1_D_flux_1 | Uncertainty in MIPS1 flux, Epoch 1 [mJy] | −999 | §2.3.2 |
| 107 | MP1_date_1 | Date of MIPS1 observation, Epoch 1 | null | §2.3.2 |
| 108 | MP1_Q_det_1 | Quality of MIPS1 detection, Epoch 1 | null | §2.4.5 |
| 109 | MP1_flux_2 | MIPS1 flux, Epoch 2 [mJy] | −999 | §2.3.2 |
| 110 | MP1_D_flux_2 | Uncertainty in MIPS1 flux, Epoch 2 [mJy] | −999 | §2.3.2 |
| 111 | MP1_date_2 | Date of MIPS1 observation, Epoch 2 | null | §2.3.2 |
| 112 | MP1_Q_det_2 | Quality of MIPS1 detection, Epoch 2 | null | §2.4.5 |
| 113 | MP1_flux_c | MIPS1 flux, combined epochs [mJy] | −999 | §2.3.2 |
| 114 | MP1_D_flux_c | Uncertainty in MIPS1 flux, combined epochs [mJy] | −999 | §2.3.2 |
| 115 | MP1_date_c | Date of MIPS1 observation, combined epochs | null | §2.3.2 |
| 116 | MP1_Q_det_c | Quality of MIPS1 detection, combined epochs | null | §2.4.5 |
| 117 | MP1_Q_flux_m | Quality of MIPS1 flux match | Q | §2.4.5 |
| 118 | MP1_imtype | Image type from MIPS1 source extraction | null | Table 11 |
| 119 | MP1_src_area | Area of MIPS1 source [pixel$^2$] | −999 | §2.3.2 |
| 120 | MP1_amajor | Length of MIPS1 source major axis [pixel] | −999 | §2.3.2 |
| 121 | MP1_aminor | Length of MIPS1 source minor axis [pixel] | −999 | §2.3.2 |
| 122 | MP1_tilt | Tilt angle for MIPS1 [deg] | −999 | §2.3.2 |
| 123 | MP2_flux_1 | MIPS2 flux, Epoch 1 [mJy] | −999 | Not used |
| 124 | MP2_D_flux_1 | Uncertainty in MIPS2 flux, Epoch 1 [mJy] | −999 | Not used |
| 125 | MP2_date_1 | Date of MIPS2 observation, Epoch 1 | null | Not used |
| 126 | MP2_Q_det_1 | Quality of MIPS2 detection, Epoch 1 | null | Not used |
| 127 | MP2_flux_2 | MIPS2 flux, Epoch 2 [mJy] | −999 | Not used |
| 128 | MP2_D_flux_2 | Uncertainty in MIPS2 flux, Epoch 2 [mJy] | −999 | Not used |

Table 16—Continued

| Column Number | Column Name | Description | Null Value | Reference |
|---|---|---|---|---|
| 129 | MP2_date_2 | Date of MIPS2 observation, Epoch 2 | null | Not used |
| 130 | MP2_Q_det_2 | Quality of MIPS2 detection, Epoch 2 | null | Not used |
| 131 | MP2_flux_c | MIPS2 flux, combined epochs [mJy] | −999 | §2.3.2 |
| 132 | MP2_D_flux_c | Uncertainty in MIPS2 flux, combined epochs [mJy] | −999 | §2.3.2 |
| 133 | MP2_date_c | Date of MIPS2 observation, combined epochs | null | §2.3.2 |
| 134 | MP2_Q_det_c | Quality of MIPS2 detection, combined epochs | null | §2.4.5 |
| 135 | MP2_Q_flux_m | Quality of MIPS2 flux match | Q | Not used |
| 136 | MP2_imtype | Image type from MIPS2 source extraction | null | Table 12 |
| 137 | MP2_src_area | Area of MIPS2 source [pixel$^2$] | −999 | Not used |
| 138 | MP2_amajor | Length of MIPS2 source major axis [pixel] | −999 | Not used |
| 139 | MP2_aminor | Length of MIPS2 source minor axis [pixel] | −999 | Not used |
| 140 | MP2_tilt | Tilt angle for MIPS2 [deg] | −999 | Not used |

[a] Null value for this column should never occur in the catalogs.

Table 17. Description of Columns in Millimeter Catalogs

| Col. No. | Column Name | Description | Null Value | Reference |
|---|---|---|---|---|
| 1 | Bolo_ID | Bolocam source name | null[a] | ··· |
| 2 | RA | Right Ascension [deg; J2000] | null[a] | ··· |
| 3 | Dec | Declination [deg; J2000] | null[a] | ··· |
| 4 | Peak_flux | Peak flux density per beam [Jy beam$^{-1}$] | null[a] | §3.2.3 |
| 5 | D_Peak_flux | Uncertainty in Peak_flux [Jy beam$^{-1}$] | null[a] | §3.2.3 |
| 6 | S/N | Signal to noise ratio of peak flux | null[a] | ··· |
| 7 | Flux_40asec | Integrated flux density in 40 arcsec diameter aperture [Jy] | null | §3.2.3 |
| 8 | D_Flux_40asec | Uncertainty in Flux_40asec [Jy] | null | §3.2.3 |
| 9 | Flux_80asec | Integrated flux density in 80 arcsec diameter aperture [Jy] | null | §3.2.3 |
| 10 | D_Flux_80asec | Uncertainty in Flux_80asec [Jy] | null | §3.2.3 |
| 11 | Flux_120asec | Integrated flux density in 120 arcsec diameter aperture [Jy] | null | §3.2.3 |
| 12 | D_Flux_120asec | Uncertainty in Flux_120asec [Jy] | null | §3.2.3 |
| 13 | Total_flux | Total integrated flux density [Jy] | null[a] | §3.2.3 |
| 14 | D_Total_flux | Uncertainty in total flux [Jy] | null[a] | §3.2.3 |
| 15 | FWHM_minor | FWHM along source minor axis [arcsec] | null[a] | §3.2.3 |
| 16 | D_FWHM_minor | Uncertainty in FWHM_minor [arcsec] | null[a] | §3.2.3 |
| 17 | FWHM_major | FWHM along source major axis [arcsec] | null[a] | §3.2.3 |
| 18 | D_FWHM_major | Uncertainty in FWHM_major [arcsec] | null[a] | §3.2.3 |
| 19 | PA | Position angle [deg] | null[a] | §3.2.3 |
| 20 | D_PA | Uncertainty in position angle [deg] | null[a] | §3.2.3 |
| 21 | Mass_10K | Total isothermal mass for T= 10K [$M_\odot$] | null[a] | §3.2.3 |
| 22 | D_Mass_10K | Uncertainty in total mass [$M_\odot$] | null[a] | §3.2.3 |
| 23 | Peak_Av | Visual extinction calculated from the peak flux [mag] | null | §3.2.3 |
| 24 | mean_density | Mean particle density (assuming spherical source) [cm$^{-3}$] | null | §3.2.3 |
| 25 | Morphology | Description of source shape and environment | null | §3.2.3 |
| 26 | Spitzer_YSO | Association with one (yes) or more (multiple) c2d YSO(s) | null | §3.2.3 |
| 27 | SSTc2d_ID | c2d source name of nearest YSO [SSTc2d....] | null | ··· |

[a] Null value for this column should never occur in the catalogs.

Table 18: Magnitude Ranges For Artificial Stars Used For Completeness Tests

| Band | Faint Magnitude | Min Flux (mJy) | Bright Magnitude | Max Flux (mJy) |
|---|---|---|---|---|
| IRAC 1 | 17.42 | 0.03 | 11.42 | 7.54 |
| IRAC 2 | 16.94 | 0.03 | 10.94 | 7.54 |
| IRAC 3 | 15.41 | 0.08 | 9.41 | 20.1 |
| IRAC 4 | 14.50 | 0.10 | 8.50 | 25.1 |
| MIPS 24 | 10.05 | 0.70 | 4.05 | 175.8 |

Table 19. Estimates of 90% Completeness Limits from Luminosity Functions[a]

| Region | Magnitude Limits [3.6] | [4.5] | [5.8] | [8.0] | [24] | [70] | Flux Limits [mJy] $F_{3.6}$ | $F_{4.5}$ | $F_{5.8}$ | $F_{8.0}$ | $F_{24}$ | $F_{70}$ |
|---|---|---|---|---|---|---|---|---|---|---|---|---|
| Chamaeleon | 17.4 | 17.6 | 16.0 | 14.8 | 10.4 | 3.5 | 0.031 | 0.016 | 0.046 | 0.077 | 0.49 | 31 |
| Perseus | 18.8 | 18.2 | 15.8 | 14.8 | 10.0 | 2.5 | 0.0085 | 0.0094 | 0.055 | 0.077 | 0.71 | 80 |
| Serpens | 17.4 | 17.0 | 15.4 | 14.2 | 10.2 | 1.0 | 0.031 | 0.028 | 0.080 | 0.13 | 0.59 | 310 |
| Lupus I | 17.4 | 17.4 | 15.6 | 14.6 | 9.8 | 2.5[b] | 0.031 | 0.020 | 0.066 | 0.093 | 0.86 | 80[b] |
| Lupus III | 17.8 | 17.2 | 15.6 | 14.4 | 9.8 | 2.5[b] | 0.021 | 0.014 | 0.066 | 0.11 | 0.86 | 80[b] |
| Lupus IV | 17.8 | 17.2 | 15.6 | 14.6 | 10.0 | 2.5[b] | 0.021 | 0.014 | 0.066 | 0.093 | 0.71 | 80[b] |
| Ophiuchus North | 18.0 | 17.4 | 15.8 | 14.6 | 10.0 | 0.0[c] | 0.018 | 0.020 | 0.055 | 0.093 | 0.71 | 775[c] |
| Ophiuchus[d] | 18.0 | 17.4 | 15.6 | 14.2 | 10.0 | 0.0[c] | 0.018 | 0.020 | 0.066 | 0.11 | 0.71 | 775[c] |

[a] Neglecting systematic errors, uncertainties are ∼10% (IRAC, MIPS1) and ∼30% (MIPS2) in flux (see §3.4.1).
[b] The Lupus regions were combined for these 70 $\mu$m source statistics.
[c] The Ophiuchus regions were combined for these 70 $\mu$m source statistics.
[d] L1688 and L1689 regions of Ophiuchus

Table 20: Deep Observations of Cores

| Core | Program | Exposure Times[a] [minutes] IRAC | MIPS1 |
|---|---|---|---|
| BHR16 | Cores2Deeper | 8 (0.8) | 0.5 (0.05) |
| CB130−3 | Cores2Deeper | 8 (0.8) | 0.5 (0.10) |
| CG30 | Cores2Deeper | 8 (0.8) | 0.5 (0.05) |
| DC2573−25 | Cores2Deeper | 8 (0.8) | 0.5 (0.05) |
| IRAM04191+1522 | Cores2Deeper | 8 (0.8) | 1 (0.10) |
| L204C−2 | DeepCores | 42 (0.8) | 2 (0.10) |
| L328 | Cores2Deeper | 8 (0.8) | 0.5 (0.10) |
| L429−C | Cores2Deeper | 8 (0.8) | 0.5 (0.10) |
| L492 | Cores2Deeper | 8 (0.8) | 0.5 (0.10) |
| L673−7 | Cores2Deeper | 8 (0.8) | 0.5 (0.10) |
| L694−2 | Cores2Deeper | 8 (0.8) | 0.5 (0.10) |
| L1148 | Cores2Deeper | 8 (0.8) | 0.5 (0.05) |
| L1152 | DeepCores | 36 (0.8) | 2 (0.05) |
| L1155C−2 | DeepCores | 36 (0.8) | 2 (0.05) |
| L1221 | Cores2Deeper | 8 (0.8) | 0.5 (0.05) |
| L1228 | DeepCores | 36 (0.8) | 2 (0.05) |
| L1521B−2 | Cores2Deeper | 8 (0.8) | 0.5 (0.10) |

[a]These are approximate exposure times for a majority of the pixels. For comparison, the exposure times for the c2d observations are listed in parenthesis.

Table 21: Adopted Fluxes for Zero Magnitude[a]

| System | Band | $\lambda$ | Zero Point [Jy] | Uncertainty |
|---|---|---|---|---|
| 2MASS | J | 1.235 | 1594.0 | 10% |
| 2MASS | H | 1.662 | 1024.0 | 10% |
| 2MASS | $K_s$ | 2.159 | 666.7 | 10% |
| IRAC | 1 | 3.550 | 280.9 | 1.5% |
| IRAC | 2 | 4.493 | 179.7 | 1.5% |
| IRAC | 3 | 5.731 | 115.0 | 1.5% |
| IRAC | 4 | 7.872 | 64.13 | 1.5% |
| MIPS | 1 | 24.0 | 7.14 | 4% |
| MIPS | 2 | 70.0 | 0.775 | 20% |
| MIPS | 3 | 160.0 | 0.159 | 20% |

[a]Discussion and references given in §3.5.3.

Table 22: Standard Stars

| Star | Coordinates [J2000] | | Standard Magnitudes | | | | Standard |
|---|---|---|---|---|---|---|---|
| | R.A. | Dec. | $[3.6]_0$ | $[4.5]_0$ | $[5.8]_0$ | $[8.0]_0$ | Type[a] |
| NPM1.60.0581 | $17^h\ 24^m\ 52.27^s$ | $+60°\ 25'\ 50.8''$ | 9.666 | 9.653 | 9.659 | 9.669 | Primary |
| 1732526+7104 | $17^h\ 32^m\ 52.62^s$ | $+71°\ 04'\ 43.1''$ | 12.240 | 12.237 | 12.233 | 12.236 | Faint |
| 1740138+6942 | $17^h\ 40^m\ 13.80^s$ | $+69°\ 42'\ 13.4''$ | 12.000 | 11.999 | 11.996 | 11.998 | Faint |
| 1743045+6655 | $17^h\ 43^m\ 04.50^s$ | $+66°\ 55'\ 01.7''$ | 12.798 | 12.789 | 12.782 | 12.788 | Faint |
| KF08T3 | $17^h\ 55^m\ 16.22^s$ | $+66°\ 10'\ 11.6''$ | 10.944 | 10.986 | 10.985 | 10.943 | Primary |
| KF06T1 | $17^h\ 57^m\ 58.49^s$ | $+66°\ 52'\ 29.3''$ | 10.762 | 10.906 | 10.833 | 10.793 | Primary |
| KF06T2 | $17^h\ 58^m\ 37.98^s$ | $+66°\ 46'\ 52.2''$ | 11.065 | 11.193 | 11.133 | 11.095 | Primary |
| NPM1.67.0536 | $17^h\ 58^m\ 54.66^s$ | $+67°\ 47'\ 36.8''$ | 6.306 | 6.428 | 6.389 | 6.348 | Primary |
| KF09T1 | $17^h\ 59^m\ 23.04^s$ | $+66°\ 02'\ 56.1''$ | 8.046 | 8.087 | 8.086 | 8.047 | Primary |
| 1800086+6127 | $18^h\ 00^m\ 08.62^s$ | $+61°\ 27'\ 05.2''$ | 12.156 | 12.155 | 12.152 | 12.154 | Faint |
| HD165459 | $18^h\ 02^m\ 30.73^s$ | $+58°\ 37'\ 38.1''$ | 6.593 | 6.575 | 6.579 | 6.591 | Primary |
| 1808013+6439 | $18^h\ 08^m\ 01.32^s$ | $+64°\ 39'\ 06.8''$ | 12.480 | 12.480 | 12.479 | 12.482 | Faint |
| 1812095 | $18^h\ 12^m\ 09.56^s$ | $+63°\ 29'\ 42.3''$ | 11.275 | 11.254 | 11.255 | 11.265 | Primary |
| HD195061 | $20^h\ 29^m\ 33.20^s$ | $-18°\ 13'\ 12.0''$ | 9.330 | 9.318 | 9.310 | 9.319 | Secondary |

[a]The primary and secondary standards are described in Reach et al. (2005).

Table 23. Observations of Standard Stars

| Star | AOR | Exposure Times (sec) | | Observed Magnitudes and Uncertainties | | | |
|---|---|---|---|---|---|---|---|
| | | IRAC 1,2 | IRAC 3,4 | [3.6] | [4.5] | [5.8] | [8.0] |
| NPM1.60.0581 | 20602368 | 2.0 | 12.0 | 9.66 ± 0.05 | 9.62 ± 0.05 | 9.65 ± 0.05 | 9.57 ± 0.05 |
| NPM1.60.0581 | 20602624 | 2.0 | 12.0 | 9.68 ± 0.05 | 9.63 ± 0.05 | 9.64 ± 0.05 | 9.60 ± 0.05 |
| 1732526+7104 | 7658240,7658496 | 30.0 | 30.0 | 12.29 ± 0.07 | 12.30 ± 0.07 | 12.12 ± 0.07 | 12.22 ± 0.06 |
| 1740138+6942 | 7657216,7657472 | 30.0 | 30.0 | 12.00 ± 0.06 | 12.00 ± 0.06 | 12.08 ± 0.06 | 11.89 ± 0.06 |
| 1743045+6655 | 7659520,7659776 | 30.0 | 30.0 | 12.91 ± 0.07 | 12.88 ± 0.07 | 12.91 ± 0.07 | 12.6 ± 0.1 |
| 1743045+6655 | 8058624,8058880 | 12.0 | 12.0 | 12.82 ± 0.05 | 12.81 ± 0.06 | 12.75 ± 0.07 | 12.70 ± 0.08 |
| 1743045+6655 | 8059136,8059392 | 30.0 | 30.0 | 12.80 ± 0.06 | 12.85 ± 0.06 | 12.79 ± 0.06 | 12.73 ± 0.06 |
| 1743045+6655 | 8060672,8060928 | 12.0 | 12.0 | 12.84 ± 0.12 | ... | 13.1 ± 0.2 | 13.0 ± 0.2 |
| 1743045+6655 | 8061184,8061440 | 30.0 | 30.0 | 12.76 ± 0.08 | 12.7 ± 0.1 | 12.9 ± 0.2 | 13.0 ± 0.2 |
| KF08T3 | 20601344 | 12.0 | 30.0 | 10.93 ± 0.05 | 11.01 ± 0.05 | 11.00 ± 0.05 | 10.86 ± 0.05 |
| KF08T3 | 20601600 | 12.0 | 30.0 | 10.97 ± 0.05 | 11.00 ± 0.05 | 10.98 ± 0.05 | 10.85 ± 0.05 |
| KF06T1 | 20600320 | 12.0 | 30.0 | 10.88 ± 0.05 | 10.88 ± 0.05 | 10.90 ± 0.05 | 10.76 ± 0.05 |
| KF06T1 | 20600576 | 12.0 | 30.0 | 10.82 ± 0.05 | 10.89 ± 0.05 | 10.87 ± 0.05 | 10.80 ± 0.05 |
| KF06T2 | 20600832 | 12.0 | 30.0 | 11.08 ± 0.05 | 11.17 ± 0.05 | 11.12 ± 0.05 | 10.98 ± 0.05 |
| KF06T2 | 20601088 | 12.0 | 30.0 | 11.10 ± 0.05 | 11.15 ± 0.05 | 11.13 ± 0.05 | 11.02 ± 0.05 |
| NPM1.67.0536 | 20602880 | 0.4 | 2.0 | 6.47 ± 0.06 | 6.62 ± 0.07 | 6.32 ± 0.05 | 6.42 ± 0.06 |
| KF09T1 | 20601856 | 12.0 | 30.0 | 8.18 ± 0.05 | 8.16 ± 0.05 | 8.09 ± 0.05 | 8.03 ± 0.05 |
| KF09T1 | 20602112 | 12.0 | 30.0 | 8.17 ± 0.05 | 8.16 ± 0.05 | 8.07 ± 0.06 | 7.98 ± 0.05 |
| 1800086+6127 | 7657728,7657984 | 30.0 | 30.0 | 12.24 ± 0.07 | 12.41 ± 0.09 | 12.17 ± 0.06 | 11.98 ± 0.06 |
| HD165459 | 20596224 | 0.4 | 2.0 | 6.64 ± 0.06 | 6.61 ± 0.06 | 6.63 ± 0.06 | 6.55 ± 0.05 |
| HD165459 | 20596480 | 0.4 | 2.0 | 6.76 ± 0.06 | 6.66 ± 0.07 | 6.67 ± 0.06 | 6.72 ± 0.06 |
| 1808013+6439 | 7658752,7659264 | 30.0 | 30.0 | 12.54 ± 0.06 | 12.53 ± 0.07 | 12.47 ± 0.06 | 12.30 ± 0.06 |
| 1812095 | 20595712 | 12.0 | 30.0 | 11.32 ± 0.06 | 11.25 ± 0.05 | 11.26 ± 0.05 | 11.17 ± 0.05 |
| 1812095 | 20595968 | 12.0 | 30.0 | 11.30 ± 0.05 | 11.25 ± 0.05 | 11.31 ± 0.06 | 11.12 ± 0.05 |
| HD195061 | 20596736 | 2.0 | 12.0 | 9.39 ± 0.05 | 9.37 ± 0.05 | 9.34 ± 0.05 | 9.28 ± 0.05 |
| HD195061 | 20596992 | 2.0 | 12.0 | 9.40 ± 0.05 | 9.36 ± 0.06 | 9.34 ± 0.05 | 9.28 ± 0.05 |
| HD195061 | 20597248 | 2.0 | 12.0 | 9.39 ± 0.05 | 9.35 ± 0.05 | 9.36 ± 0.05 | 9.35 ± 0.05 |
| HD195061 | 20597504 | 2.0 | 12.0 | 9.38 ± 0.05 | 9.38 ± 0.06 | 9.31 ± 0.05 | 9.24 ± 0.06 |
| HD195061 | 20597760 | 2.0 | 12.0 | 9.37 ± 0.05 | 9.34 ± 0.05 | 9.38 ± 0.05 | 9.29 ± 0.05 |
| HD195061 | 20598016 | 2.0 | 12.0 | 9.39 ± 0.05 | 9.37 ± 0.05 | 9.41 ± 0.05 | 9.25 ± 0.05 |
| HD195061 | 20598272 | 2.0 | 12.0 | 9.40 ± 0.05 | 9.33 ± 0.05 | 9.39 ± 0.05 | 9.29 ± 0.05 |
| HD195061 | 20598528 | 2.0 | 12.0 | 9.42 ± 0.05 | 9.34 ± 0.05 | 9.31 ± 0.05 | 9.32 ± 0.05 |
| HD195061 | 20598784 | 2.0 | 12.0 | 9.44 ± 0.06 | 9.36 ± 0.05 | 9.29 ± 0.06 | 9.31 ± 0.06 |
| HD195061 | 20599040 | 2.0 | 12.0 | 9.41 ± 0.05 | 9.33 ± 0.05 | 9.36 ± 0.05 | 9.27 ± 0.05 |
| HD195061 | 20599296 | 2.0 | 12.0 | 9.38 ± 0.05 | 9.32 ± 0.05 | 9.36 ± 0.05 | 9.27 ± 0.05 |
| HD195061 | 20599552 | 2.0 | 12.0 | 9.40 ± 0.05 | 9.36 ± 0.05 | 9.38 ± 0.05 | 9.28 ± 0.05 |

Table 24: Comparison of c2d and Standard IRAC Photometry

| Band | Relative Photometric Offset |
|---|---|
| IRAC 1 | −5.4% |
| IRAC 2 | −2.3% |
| IRAC 3 | −2.5% |
| IRAC 4 | +4.5% |

Table 25: Resolutions Available for Extinction Maps

| Cloud | Beam FWHM[a] |
|---|---|
| Chamaeleon | 120 – 300″ |
| Perseus | 180 – 300″ |
| Serpens | 90 – 300″ |
| Lupus-I | 120 – 300″ |
| Lupus-III | 90 – 300″ |
| Lupus-IV | 90 – 300″ |
| Ophiuchus-North | 90 – 300″ |
| Ophiuchus | 270 – 300″ |

[a] Maps are available for the given range, in FWHM increments of 30″.

Table 26: Stars in Off-Cloud Fields

| Field | Mode $A_V$ | Mode H−K |
|---|---|---|
| Chamaeleon OC1–6 | 1.07 ± 0.02 | 0.127 ± 0.008 |
| Perseus OC1–6 | 1.4 ± 0.1 | 0.145 ± 0.009 |
| Serpens OC1[a] | 3.51 ± 0.04 | 0.244 ± 0.004 |
| Lupus OC1 | 1.37 ± 0.05 | 0.124 ± 0.004 |
| Lupus OC2[a] | 2.91 ± 0.02 | 0.209 ± 0.005 |
| Ophiuchus OC1–6 | 1.96 ± 0.03 | 0.159 ± 0.004 |

[a] Based on the mode values, this field appears not to be sufficiently free of extinction.

Table 27: Adopted $A_V$ Offsets

| Cloud | $A_V$ Offset |
|---|---|
| Chamaeleon | 1.07 ± 0.02 |
| Perseus | 1.4 ± 0.1 |
| Serpens | 1.5 ± 0.4 |
| Lupus | 1.37 ± 0.05 |
| Ophiuchus | 1.96 ± 0.03 |

Table 28: Extinctions[a] Applied to SWIRE Sources

| Band | $A_\lambda/A_V$ |
|---|---|
| J | 0.2741 |
| H | 0.1622 |
| $K_s$ | 0.1119 |
| IRAC1 | 0.0671 |
| IRAC2 | 0.0543 |
| IRAC3 | 0.0444 |
| IRAC4 | 0.0463 |
| MIPS1 | 0.0259 |
| MIPS2 | 0.0000[b] |

[a] From the $R_V$ extinction law of Weingartner & Draine (2001).
[b] This value was assumed for the extinctions applied to SWIRE sources.

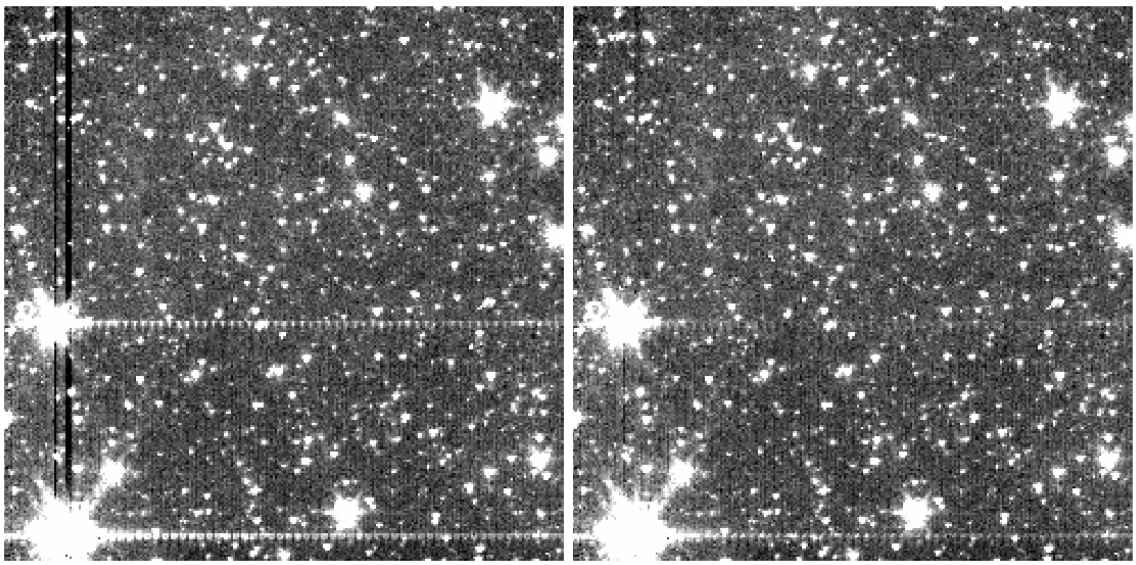

Fig. 1.— (Left) An IRAC Band-1 BCD image in this data delivery showing the effects of column pulldown and muxbleed originating from the moderately bright sources. (Right) The same image, displayed with the same greyscale, after applying the column pulldown and muxbleed corrections. The columns affected by column pulldown have been well corrected and much of muxbleed has been diminished, though not perfectly, in this image.

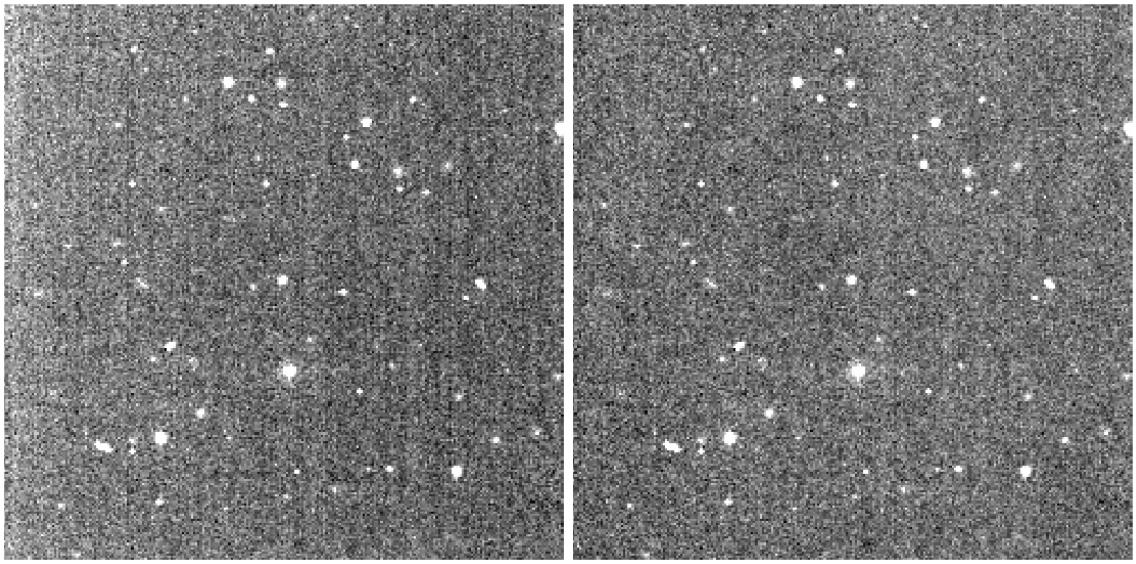

Fig. 2.— (Left) An IRAC Band-3 BCD image in this data delivery exhibiting the first-frame effect, seen by the overall horizontal gradient in the background intensity in the image, especially near the left edge of the image. (Right) The same image, displayed with the same greyscale, after correcting for the first-frame effect.

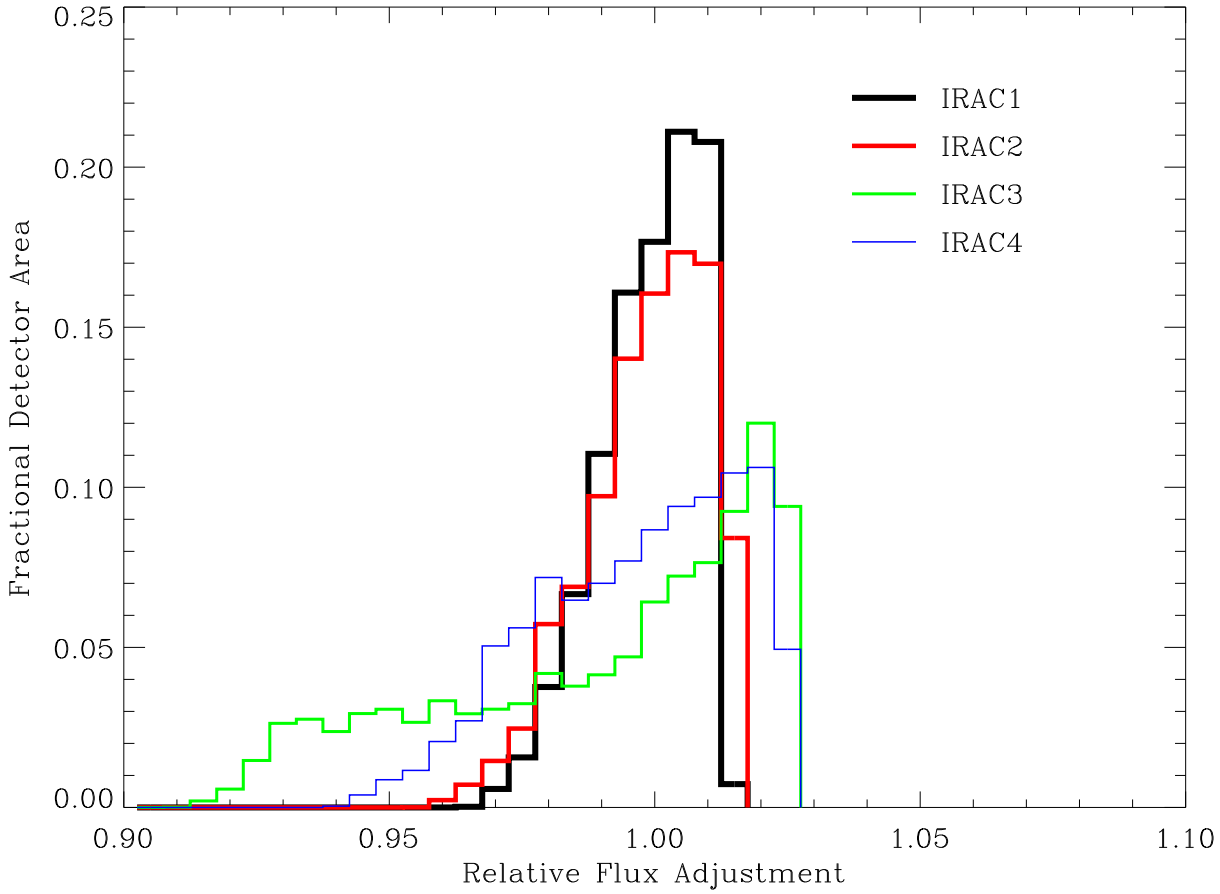


Fig. 3.— Distributions of the ratio of corrected pixel values to non-corrected pixel values, where the corrections refer to the location-dependent photometric corrections discussed in §2.1.5. Assuming that sources are uniformly distribution on the detector, these distributions should reflect changes in the source fluxes.

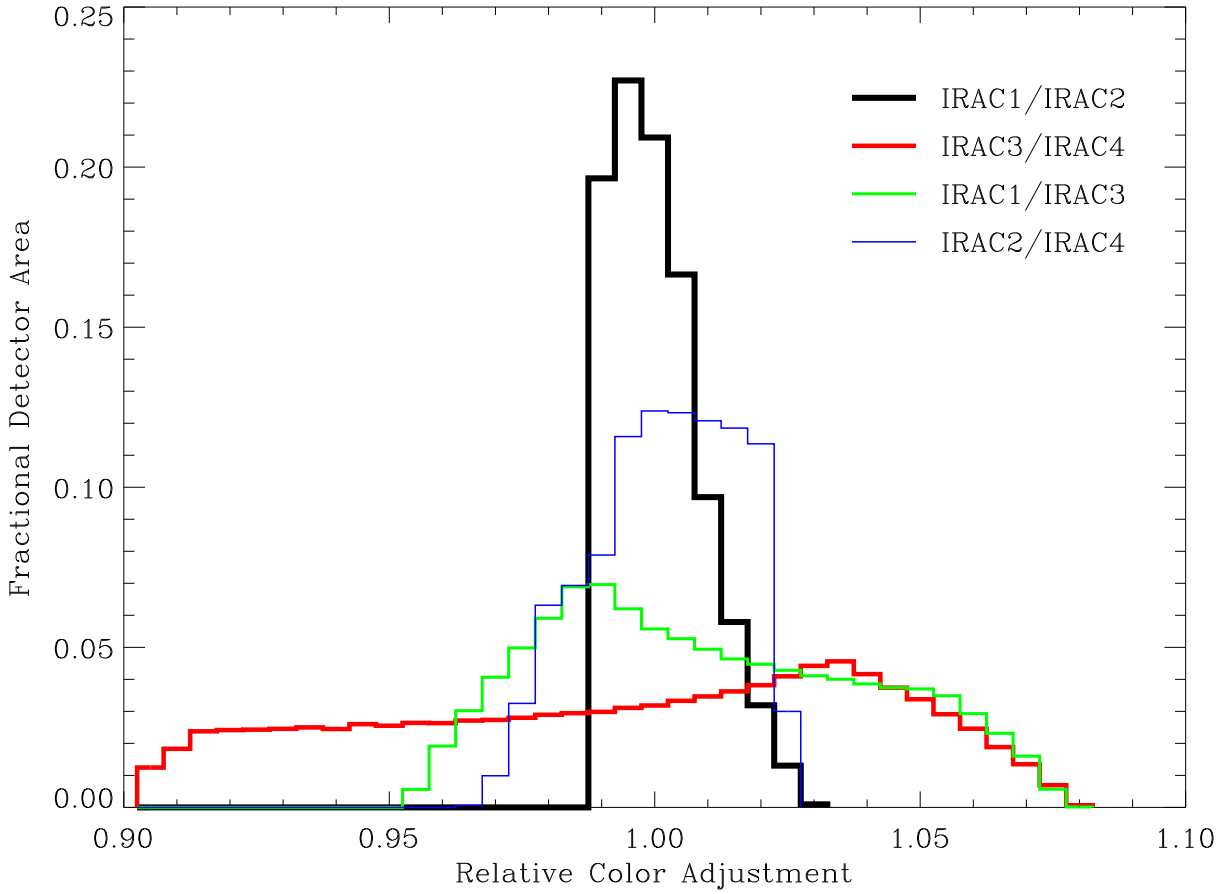


Fig. 4.— Same as Figure 3, except for some commonly used IRAC colors.

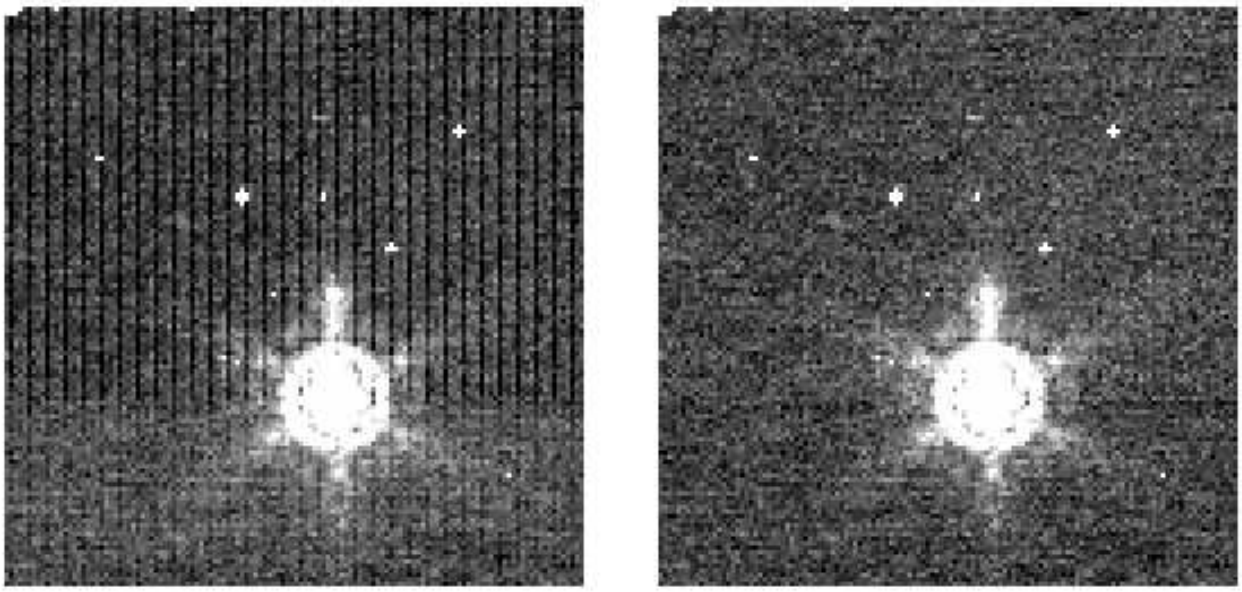

Fig. 5.— MIPS 24 $\mu$m BCD image of the star AX Cha before and after correction for "jailbars" above and below the star. The maximum peak-to-peak amplitude of the jailbar pattern before correction was 10 %. The 24 $\mu$m flux of the star is of order 3 Jy. The image is AOR=5745152, EXP=3, DCE=1.

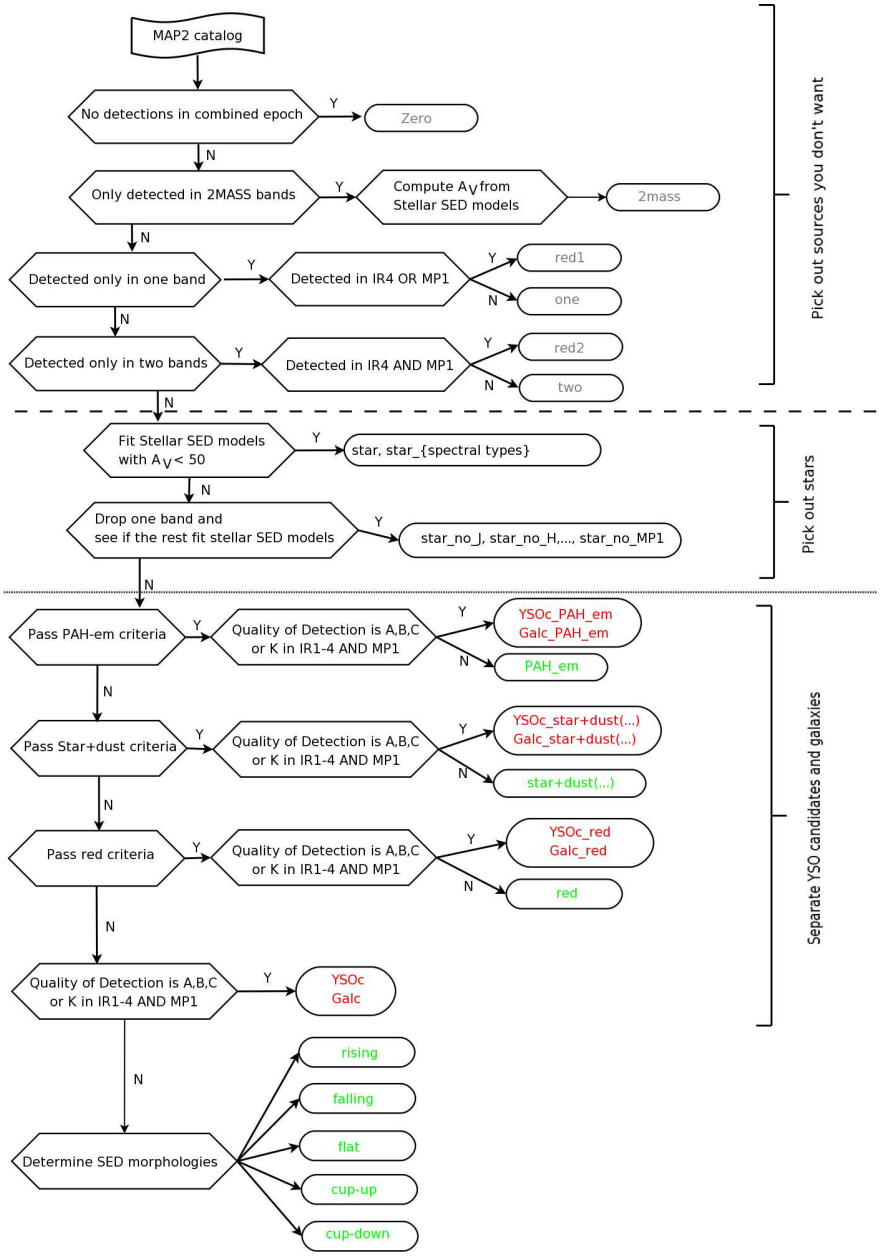


Fig. 6.— Procedure for source classification. This illustrates the flow diagram followed in sequentially assigning source class. For many sources, more than one classification is possible within the S/N of the observations. In those cases the sequence of selection is relevant. Our criteria for this delivery generously assign objects to the "star" class.

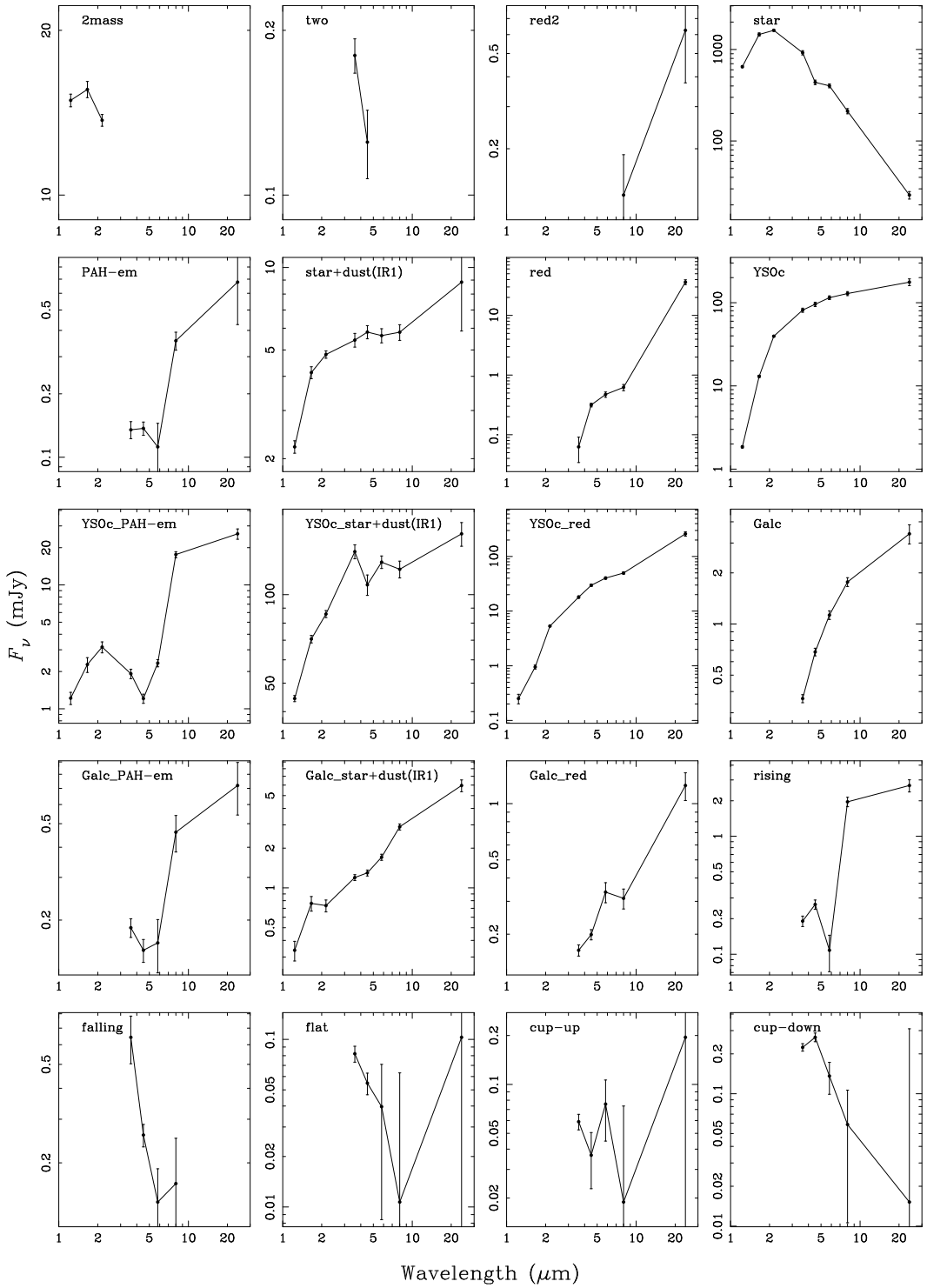


Fig. 7.— Typical SEDs for each object type

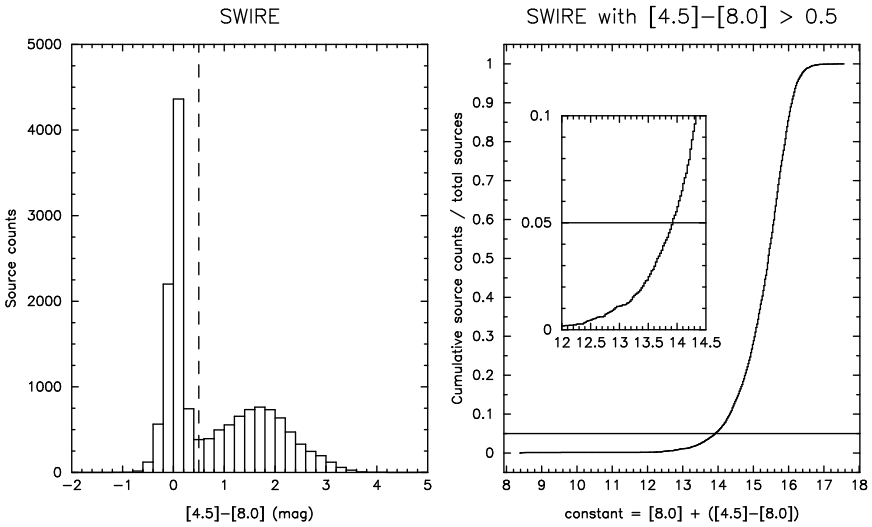


Fig. 8.— Left: [4.5]–[8.0] histogram for SWIRE sources with flux quality A or B in all IRAC bands. Right: The x axis, constant=[8.0]+([4.5]–[8.0]), is a family of diagonal lines in [8.0] vs. [4.5]–[8.0] color-magnitude diagram. The y axis is the percentage of the SWIRE source under a particular diagonal line.

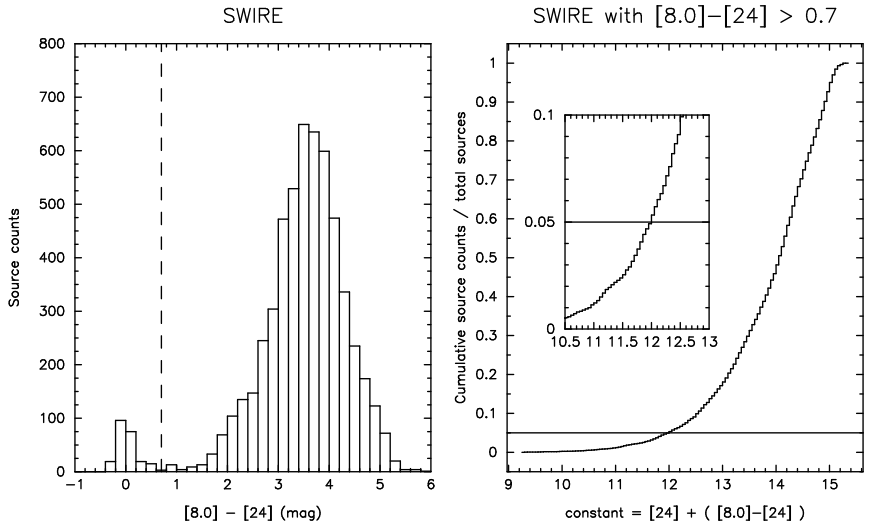


Fig. 9.— Left: [8.0]–[24] histogram for SWIRE sources with flux quality A or B in all IRAC bands and MIPS1. Right: The x axis, constant=[24]+([8.0]–[24]), is a family of diagonal lines in [24] vs. [8.0]–[24] color-magnitude diagram. The y axis is the percentage of the SWIRE source under a particular diagonal line.

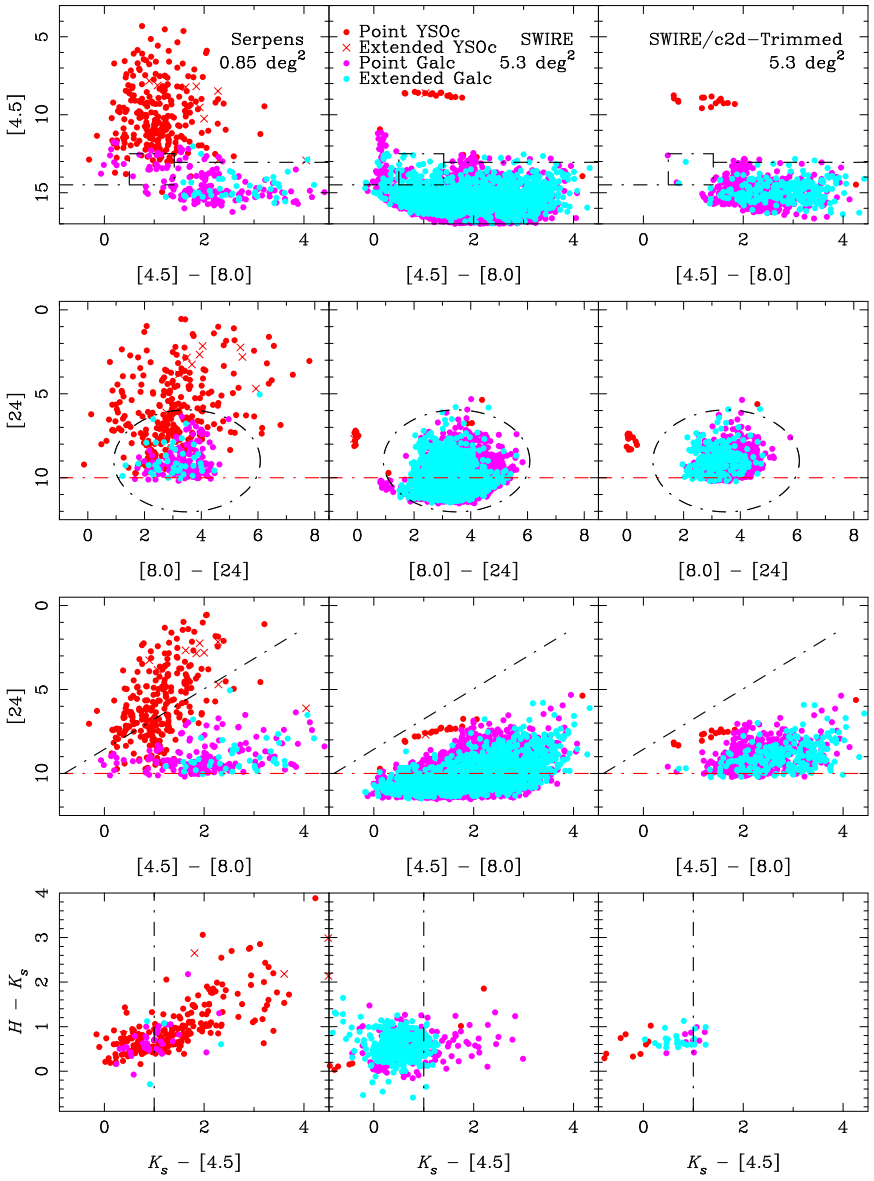


Fig. 10.— Comparison between the c2d Serpens data (left), the SWIRE data (center) and the trimmed (extincted and resampled) SWIRE data (right). The black dashed lines show the "fuzzy" color-magnitude cuts that define the YSO candidate criterion in the different color-magnitude spaces. The red dashed lines show hard limits; objects fainter than these limits are excluded from the YSOc catagory. The top panels are [4.5] vs. [4.5]−[8.0] color-magnitude diagrams. The second row show [24.0] vs. [8.0]−[24.0]. The third row show [24.0] vs. [4.5]−[8.0]. The bottom row show [H]−[K] vs. [K]−[4.5]. Objects classified as stars are excluded from this plot, which attempts to distinguish YSOc from likely background galaxies (GALc). The objects classified as YSOc in the SWIRE panels are bright stars, with saturated photometry. They appear in the YSOc catalogs, but they can usually be identified.

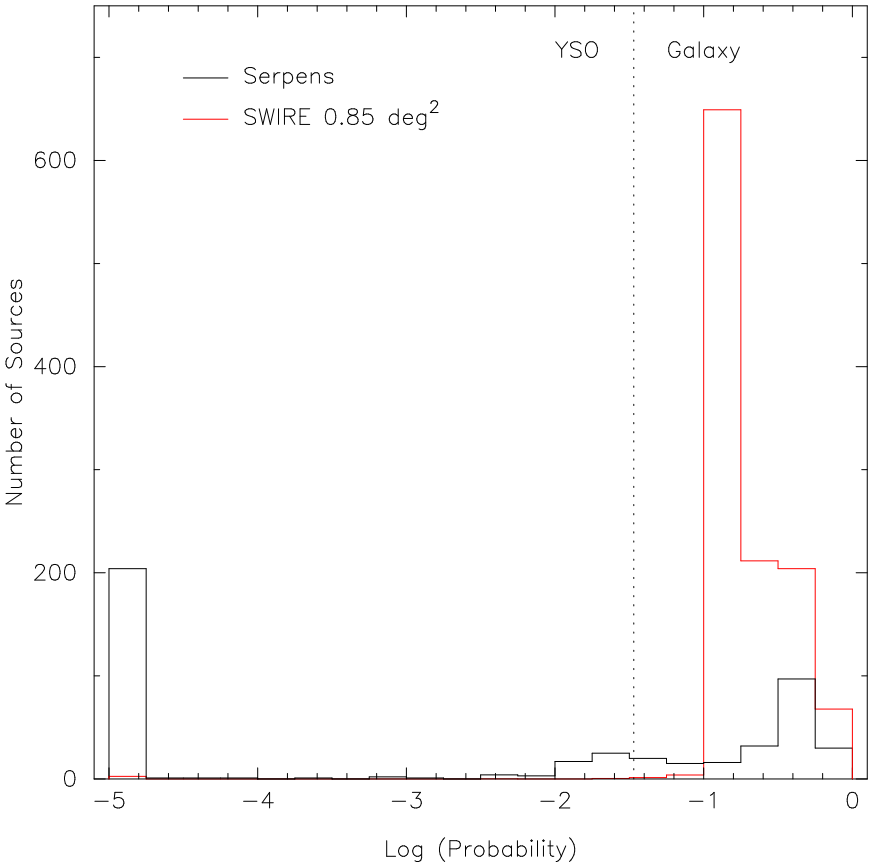


Fig. 11.— The number of sources is plotted versus the log of the probability that the source is a galaxy for both the Serpens data (black) and the SWIRE data, normalized to the same area (red). The calculation of the probability is described in §2.5.4. The vertical dashed line indicates the cutoff chosen to reject galaxies.

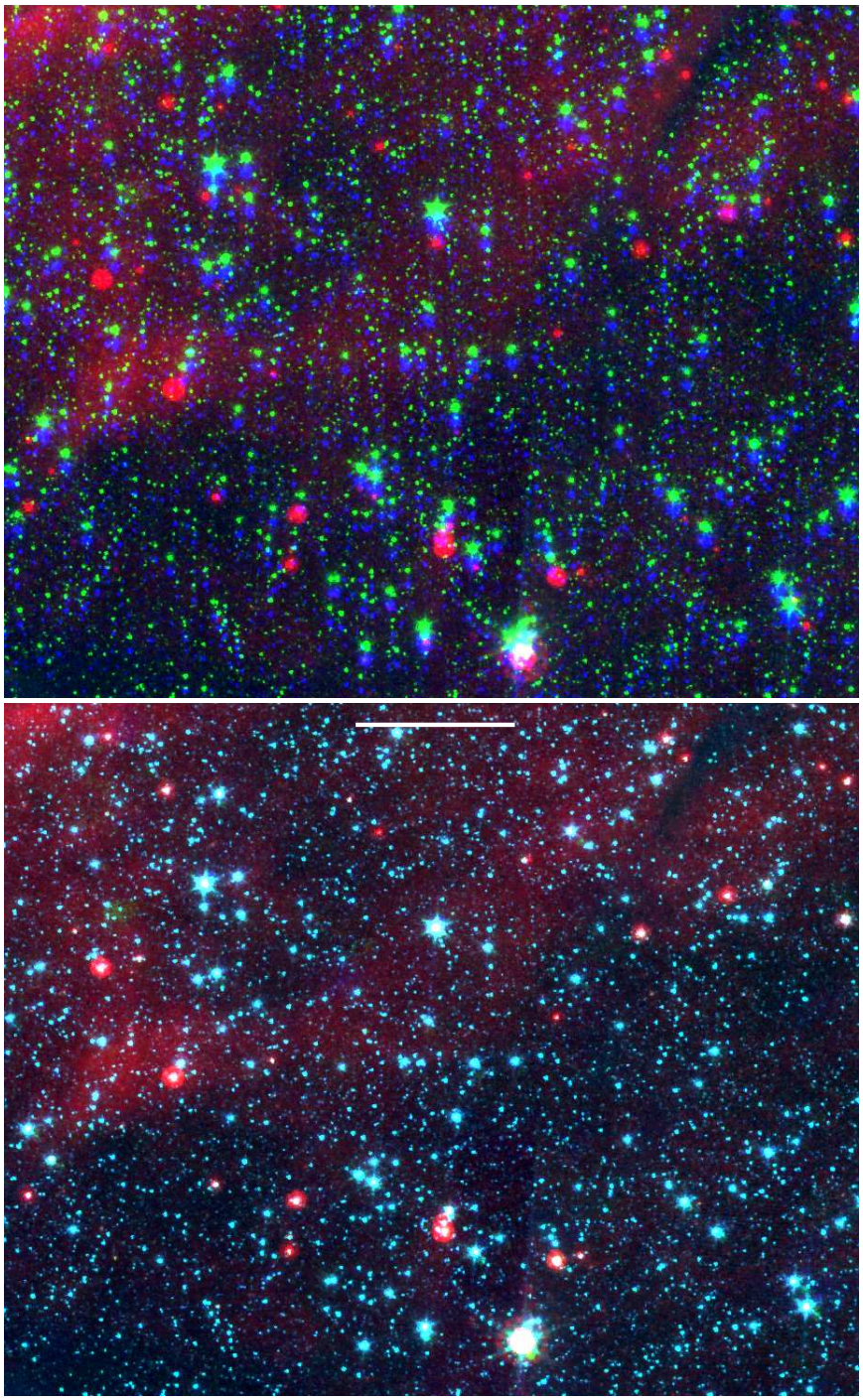

Fig. 12.— Composite images of a Serpens region created using DS9 to illustrate a "problem" with the display (see §3.1.1). [Top] This composite image was constructed from the delivered IRAC1 (blue), IRAC2 (green), and MIPS1 (red) mosaics. DS9 does not properly align the mosaics. The images of a source in different bands are offset and appear as pure blue, green, and red sources rather than appearing as one multi-colored source. [Bottom] This composite image was constructed from the same Spitzer bands as in the top panel, and for the same Serpens field, after remapping the IRAC2 and MIPS1 mosaics. The remapping procedure allows DS9 to properly display the composite. For reference, the white bar near the top of this panel represents $3'$.

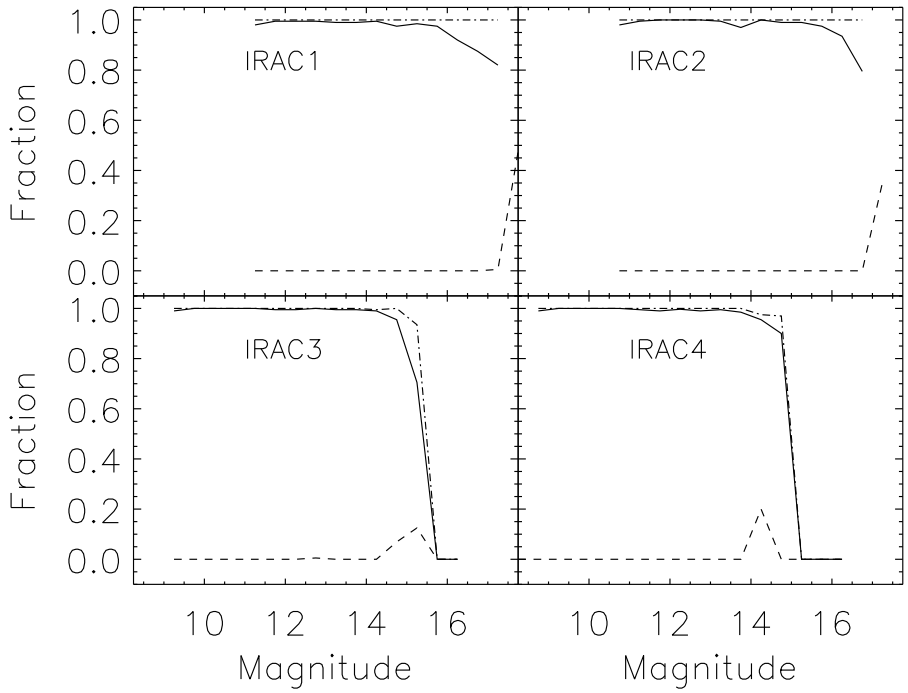


Fig. 13.— Completeness/Reliability plots for extractions of artificial stars from the IRAC mosaics of the Chamaeleon cloud. The upper solid curve shows the completeness level for extractions of artificial sources from the real+artificial mosaics, while the dash-dot curve shows the completeness level for extractions from the artificial-only mosaics (see §3.4.1). The difference between thesse curves illustrates the effect of source confusion on the completeness levels. The lower solid curve (mostly equal to zero) shows the fraction of sources extracted from the artificial-only mosaic that were false detections (i.e., noise spikes extracted as sources).

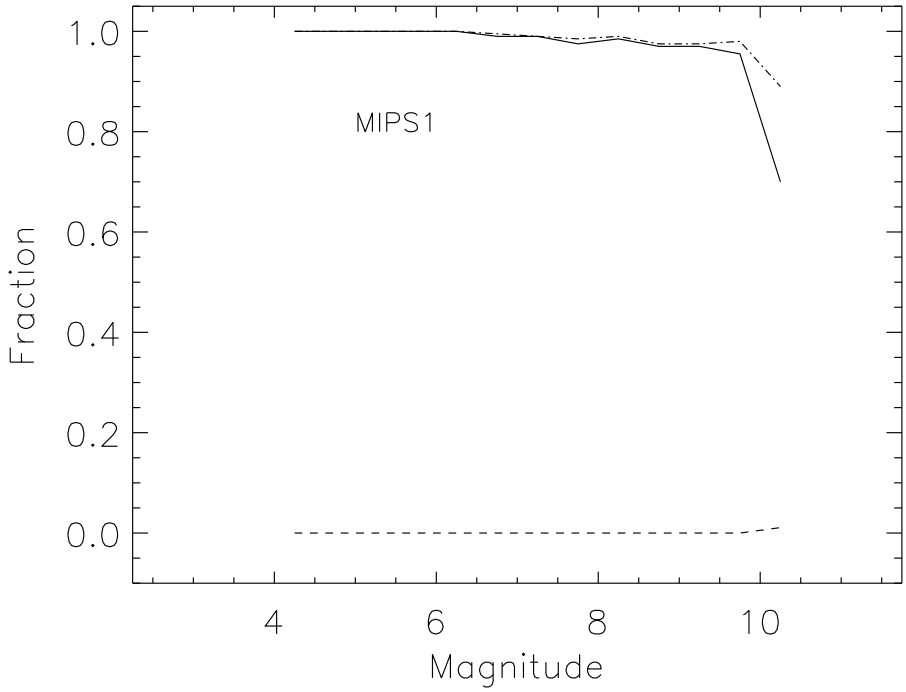


Fig. 14.— Completeness/Reliability plots for extractions of artificial stars from the MIPS mosaics of the Chamaeleon cloud, as in Figure 13.

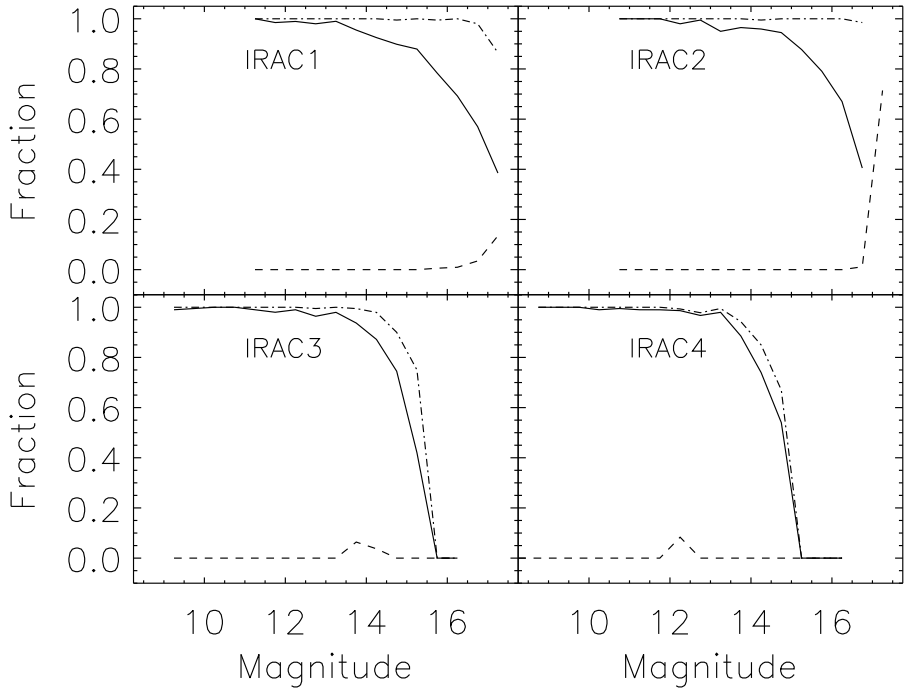


Fig. 15.— Completeness/Reliability plots for extractions of artificial stars from the IRAC mosaics of the Serpens cloud, as in Figure 13.

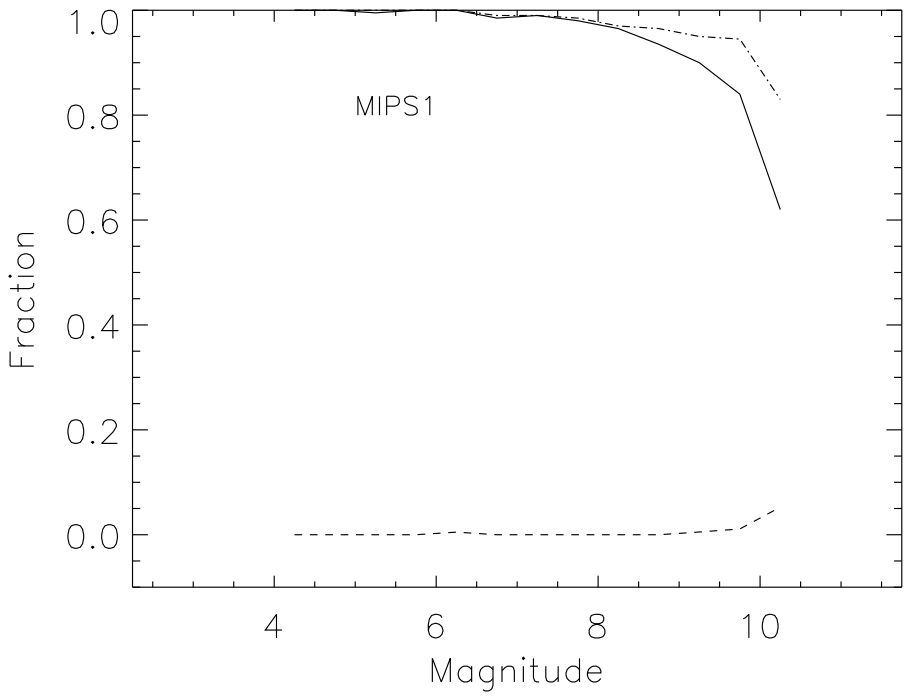


Fig. 16.— Completeness/Reliability plots for extractions of artificial stars from the MIPS mosaics of the Serpens cloud, as in Figure 13.

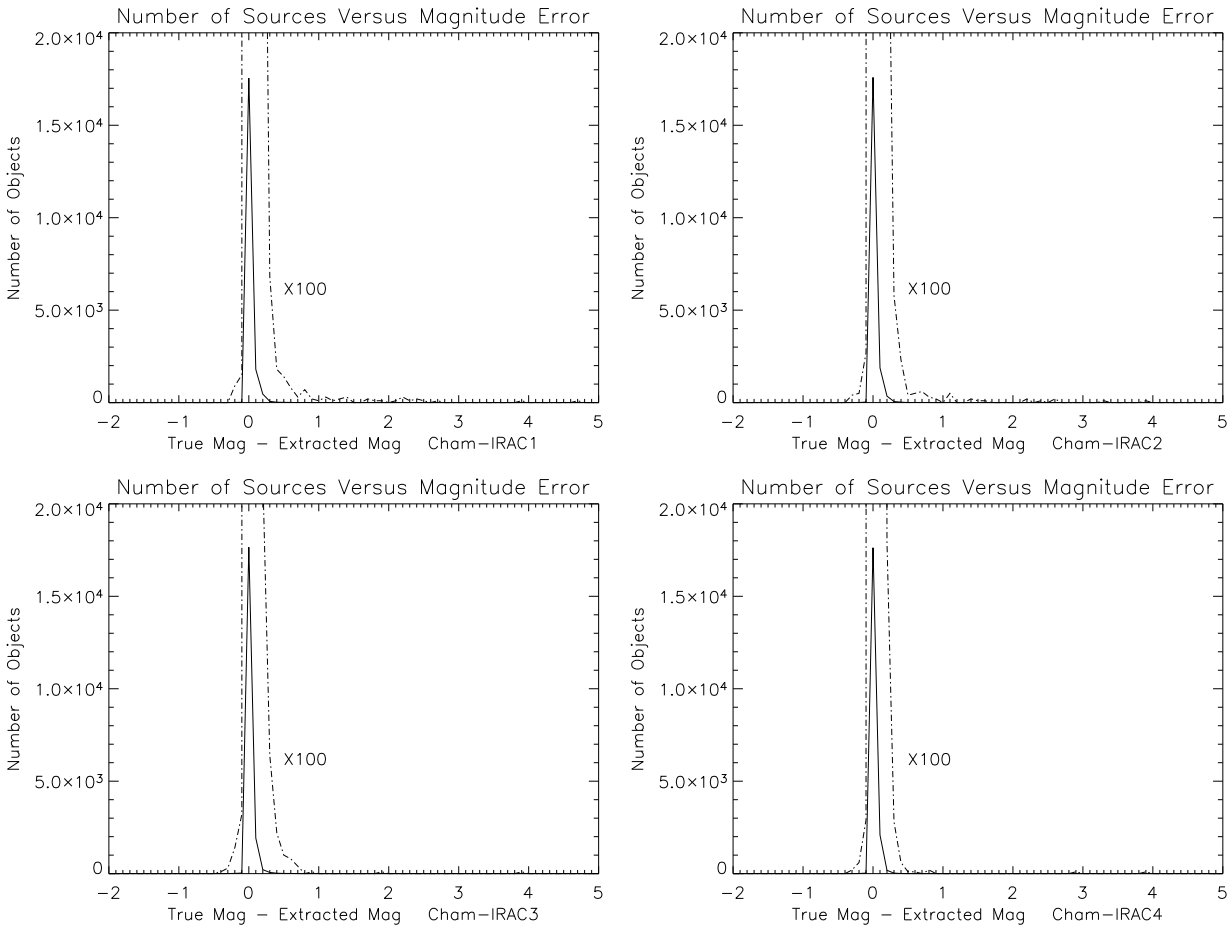


Fig. 17.— Histogram of differences between true and extracted magnitudes for the extractions of artificial stars inserted into the IRAC real+artificial mosaics of the Chamaeleon cloud. The dash-dot line shows the data multiplied by 100 to show the distribution of rare events.

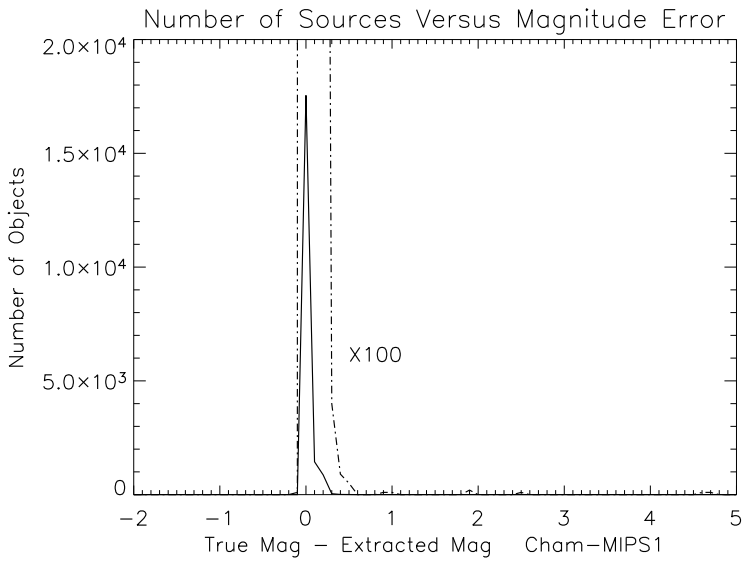


Fig. 18.— Histogram of differences between true and extracted magnitudes for the extractions of artificial stars inserted into the MIPS real+artificial mosaic of the Chameleon cloud. The dash-dot line shows the data multiplied by 100 to show the distribution of rare events.

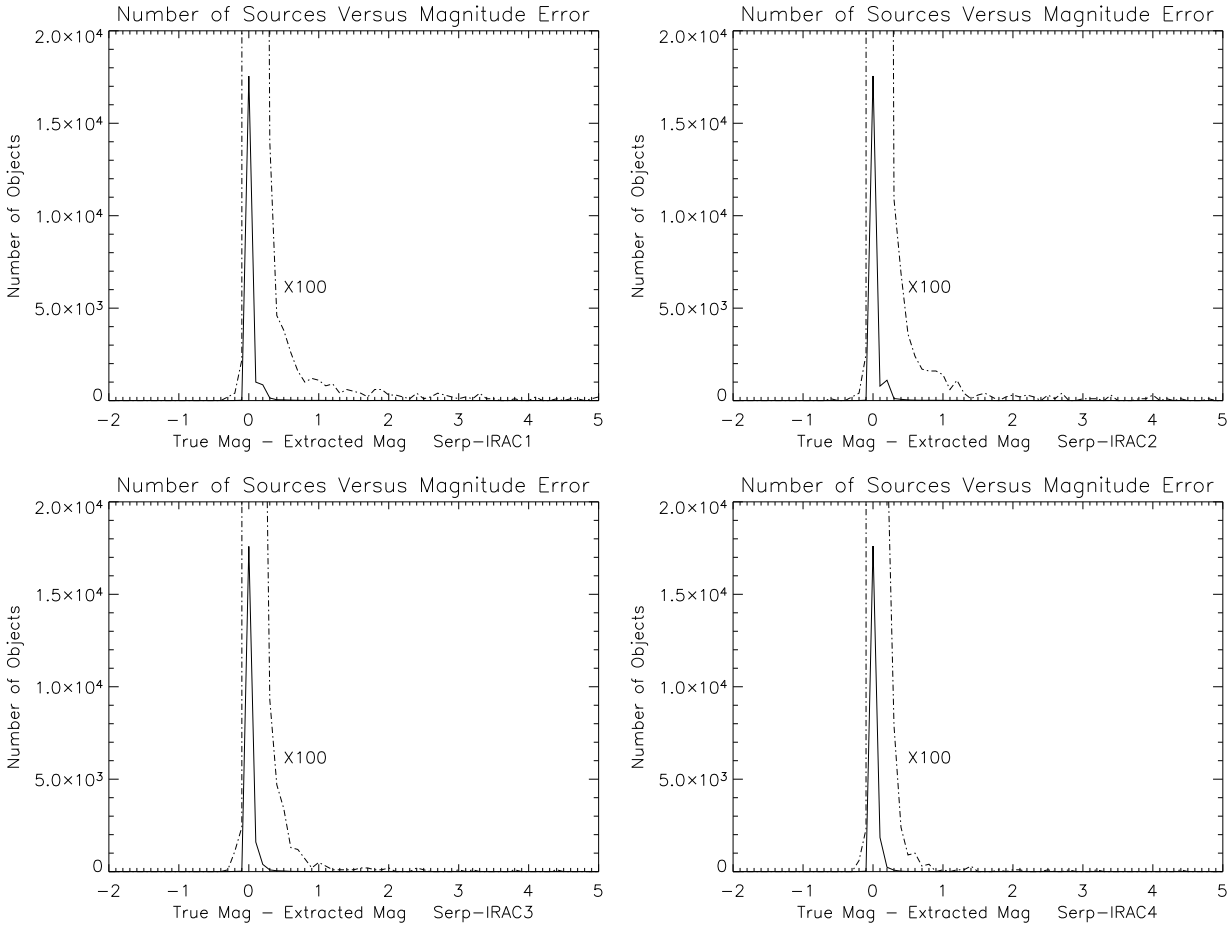


Fig. 19.— Histogram of differences between true versus extracted magnitude for the extractions of artificial stars inserted into the IRAC real+artificial mosaics of the Serpens cloud. The dash-dot line shows the data multiplied by 100 to show the distribution of rare events.

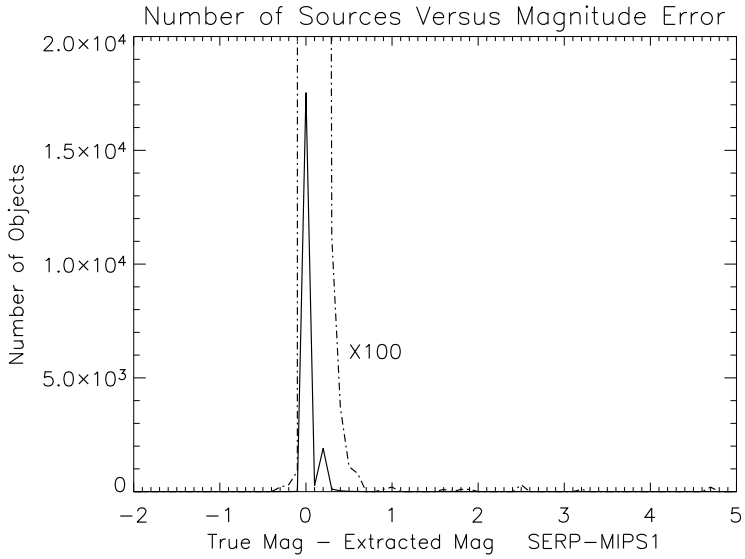


Fig. 20.— Histogram of differences between true versus extracted magnitude for the extractions of artificial stars inserted into the MIPS real+artificial mosaic of the Serpens cloud. The dash-dot line shows the data multiplied by 100 to show the distribution of rare events.

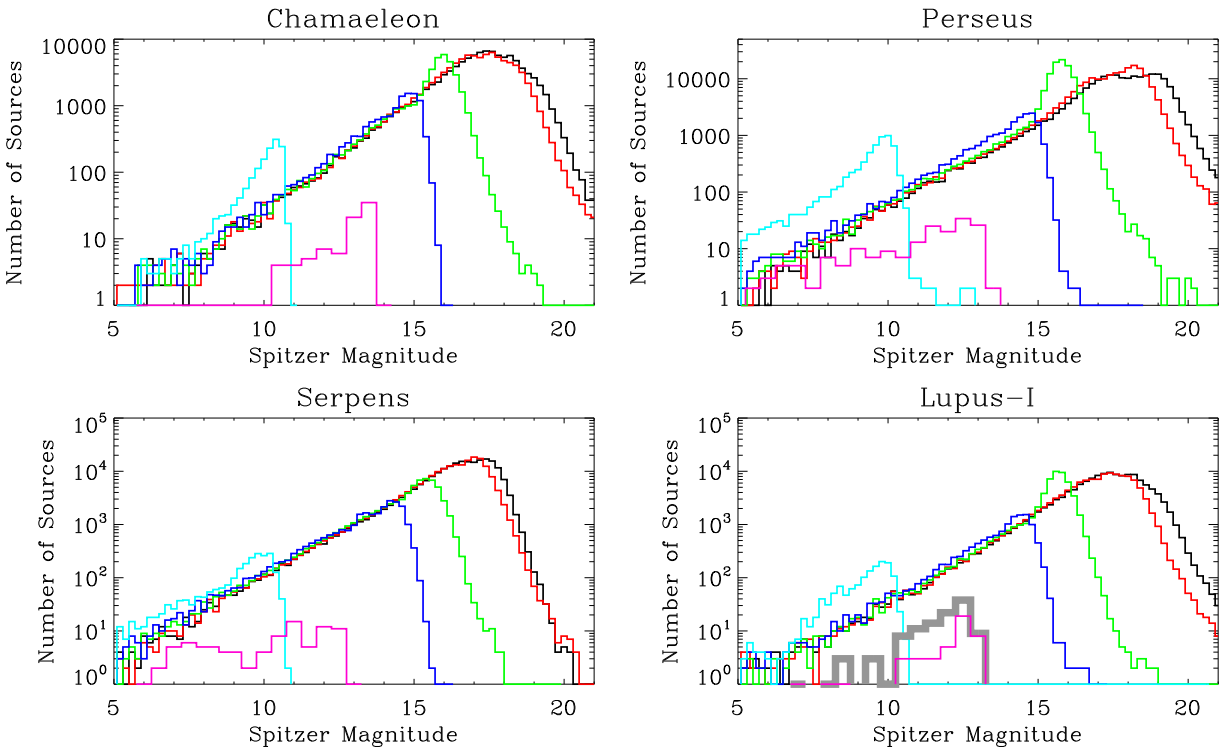


Fig. 21.— Luminosity functions for Chamaeleon, Perseus, Serpens, and Lupus I. The numbers of detected sources at 3.6, 4.5, 5.8, 8.0, 24, and 70 $\mu$m are plotted as black, red, green, blue, cyan, and magenta histograms, respectively. In order to plot the luminosity function for 70 $\mu$m on the same figure as the others, it has been shifted by +10 mag toward fainter magnitudes. The bin widths were chosen to be 0.2 mag for all bands, except for MIPS2, which was chosen to be 0.5 mag because of the relatively small number of 70 $\mu$m sources. For the Lupus I plot, the thick grey histogram shows the luminosity function using all 70 $\mu$m sources in Lupus I, III, and IV combined.

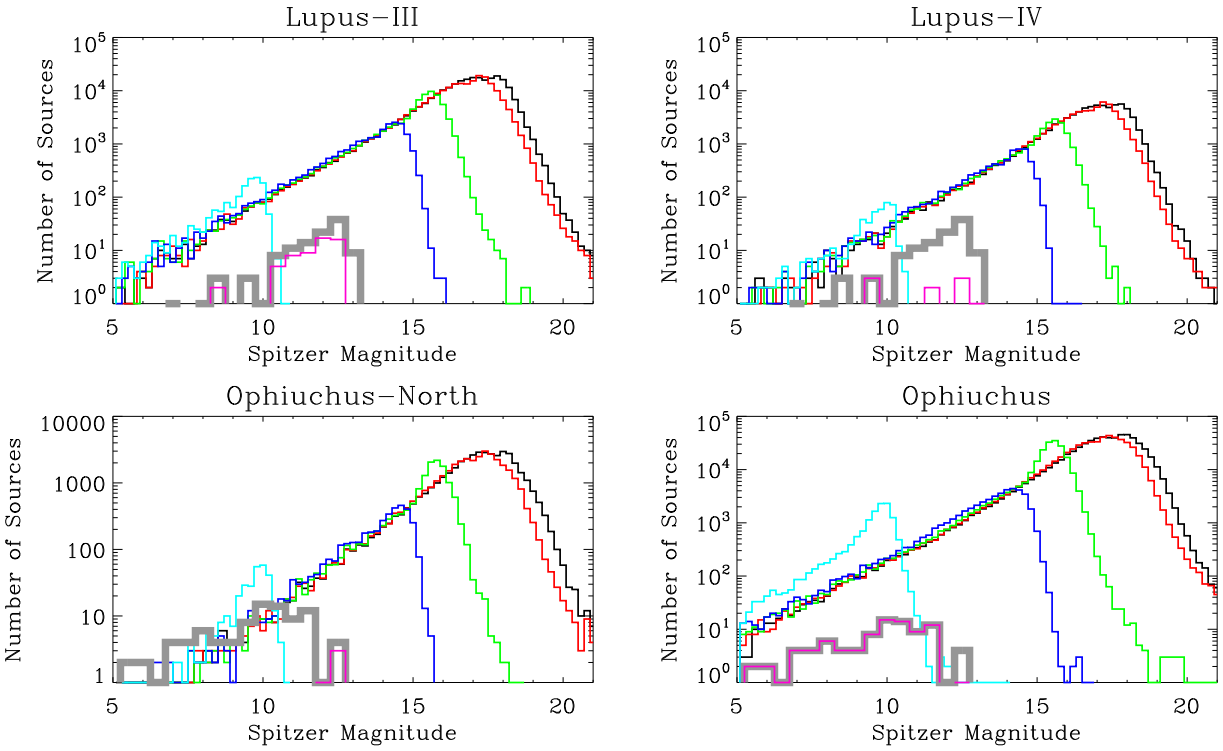


Fig. 22.— Luminosity functions for Lupus III, Lupus IV, Ophiuchus-North, and Ophiuchus (L1688 and L1689), plotted as in Figure 21. In order to plot the luminosity function for 70 $\mu$m (magenta line) on the same figure as the others, it has been shifted by +10 mag toward fainter magnitudes. For the Lupus III and IV plots, the thick grey histogram shows the luminosity function using all 70 $\mu$m sources in Lupus I, III, and IV combined. For the Ophiuchus-North and Ophiuchus plots, the thick grey histogram shows the luminosity function using all 70 $\mu$m sources in both regions. Since the Ophiuchus-North cloud has almost no 70 $\mu$m sources, the magenta line (representing sources in the main Ophiuchus cloud) is nearly identical to the thick grey line in the lower right plot.

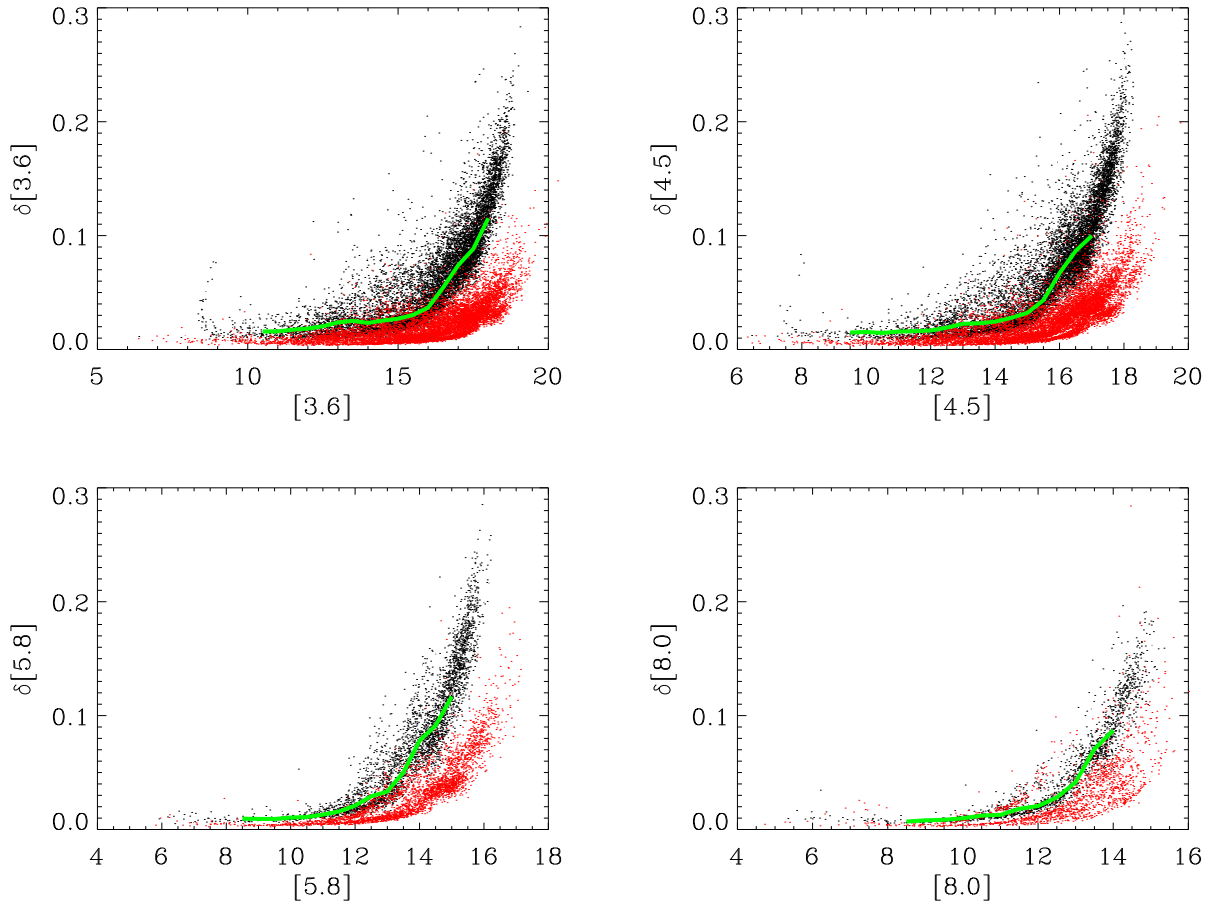


Fig. 23.— Photometric uncertainties as a function of magnitude for each of the four IRAC bands. Black symbols represent photometry from c2d observations, while the red symbols represent photometry from the deeper observations. Based on these photometric uncertainties, the green curve represents the typical repeatability dispersion expected between the c2d and deeper observations, which is dominated by the c2d photometric uncertainties and therefore lies near the distribution of c2d data on these plots.

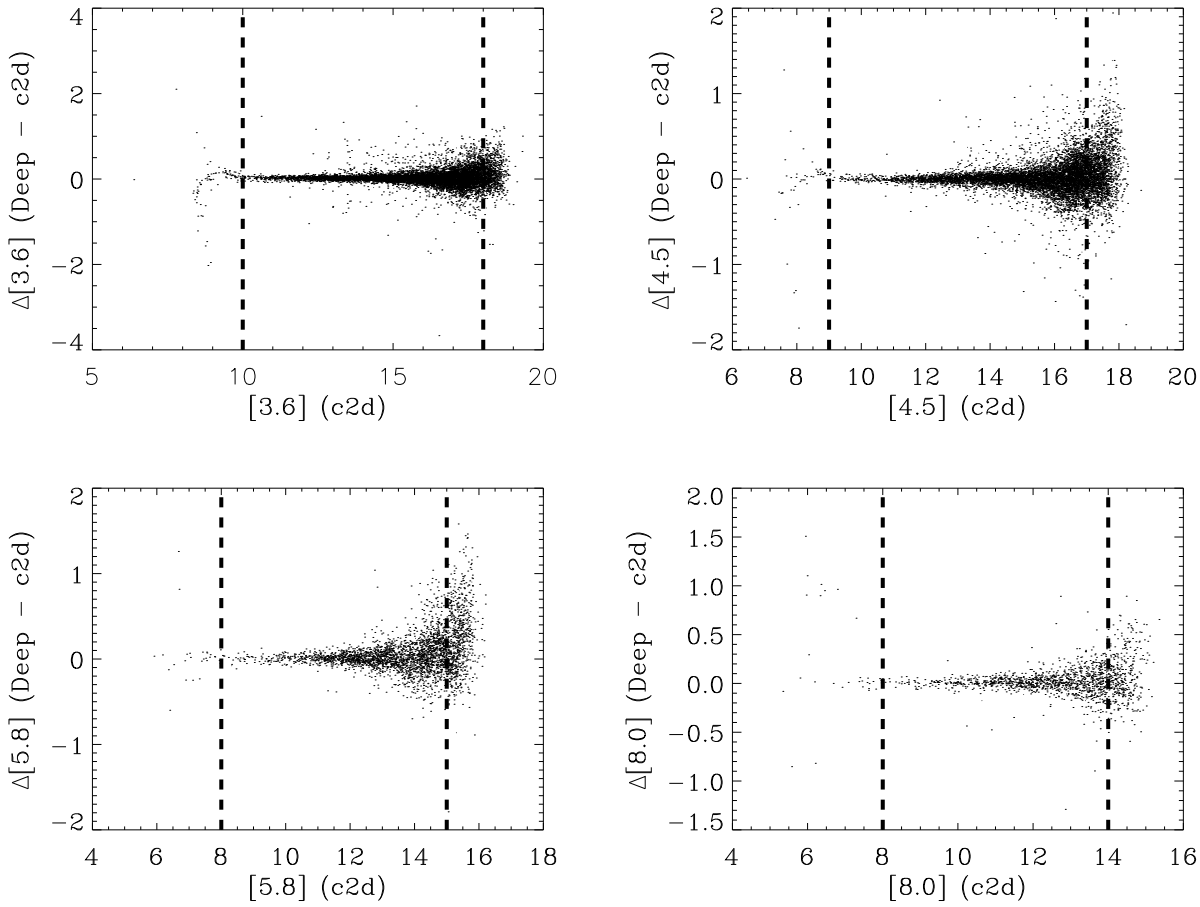


Fig. 24.— Repeatability as a function of magnitude for each of the four IRAC bands. The dashed vertical lines define the boundaries within which data are used for this analysis. For example, bright sources with [3.6] < 10 are not considered in this analysis since their photometry appears to vary to an uncharacteristically greater extent than would be expected, presumably due to saturation in at least the deeper observations. Faint sources with [3.6] > 18 are also not used in the analysis to avoid skewing results due to an observational bias near the limiting magnitudes of the c2d observations. Similar boundaries are shown for the other IRAC bands.

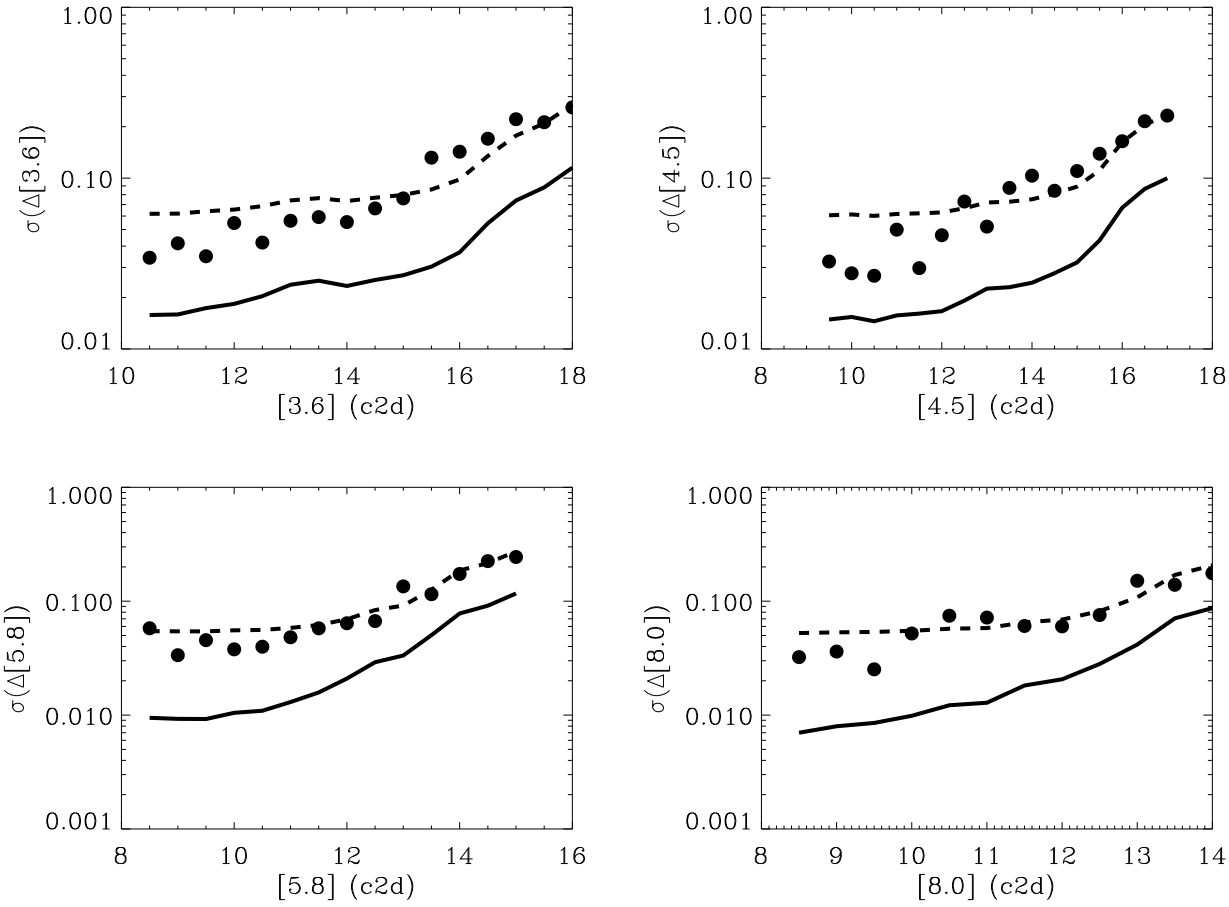


Fig. 25.— The observed repeatability dispersions, computed in bins of width 0.5 mag, are plotted as circles for each of the four IRAC bands. The theoretical repeatability dispersions, based on the photometric uncertainties (see Figure 23), are plotted as solid curves and are always less than the observed dispersions. The dashed curves represent the revised theoretical repeatability dispersions after increasing the photometric uncertainties by the adopted floor and multiplicative factor.

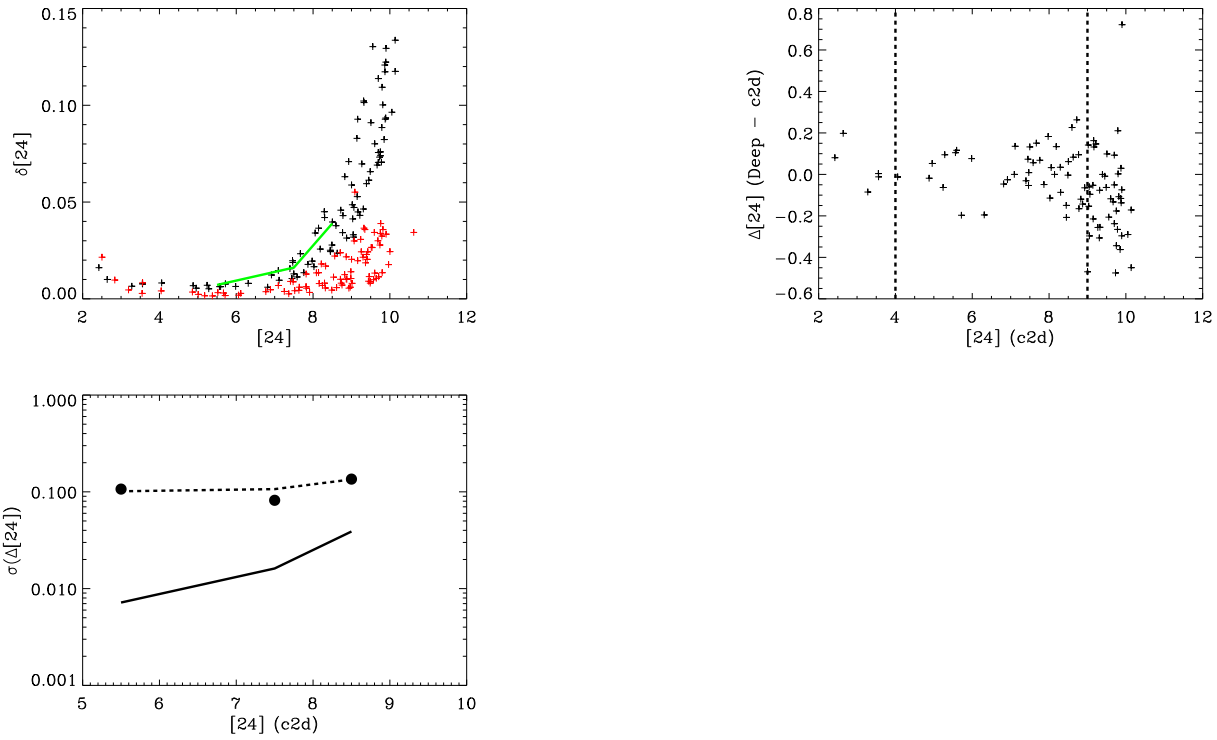


Fig. 26.— Same as Figures 23–25, but for the MIPS1 band.

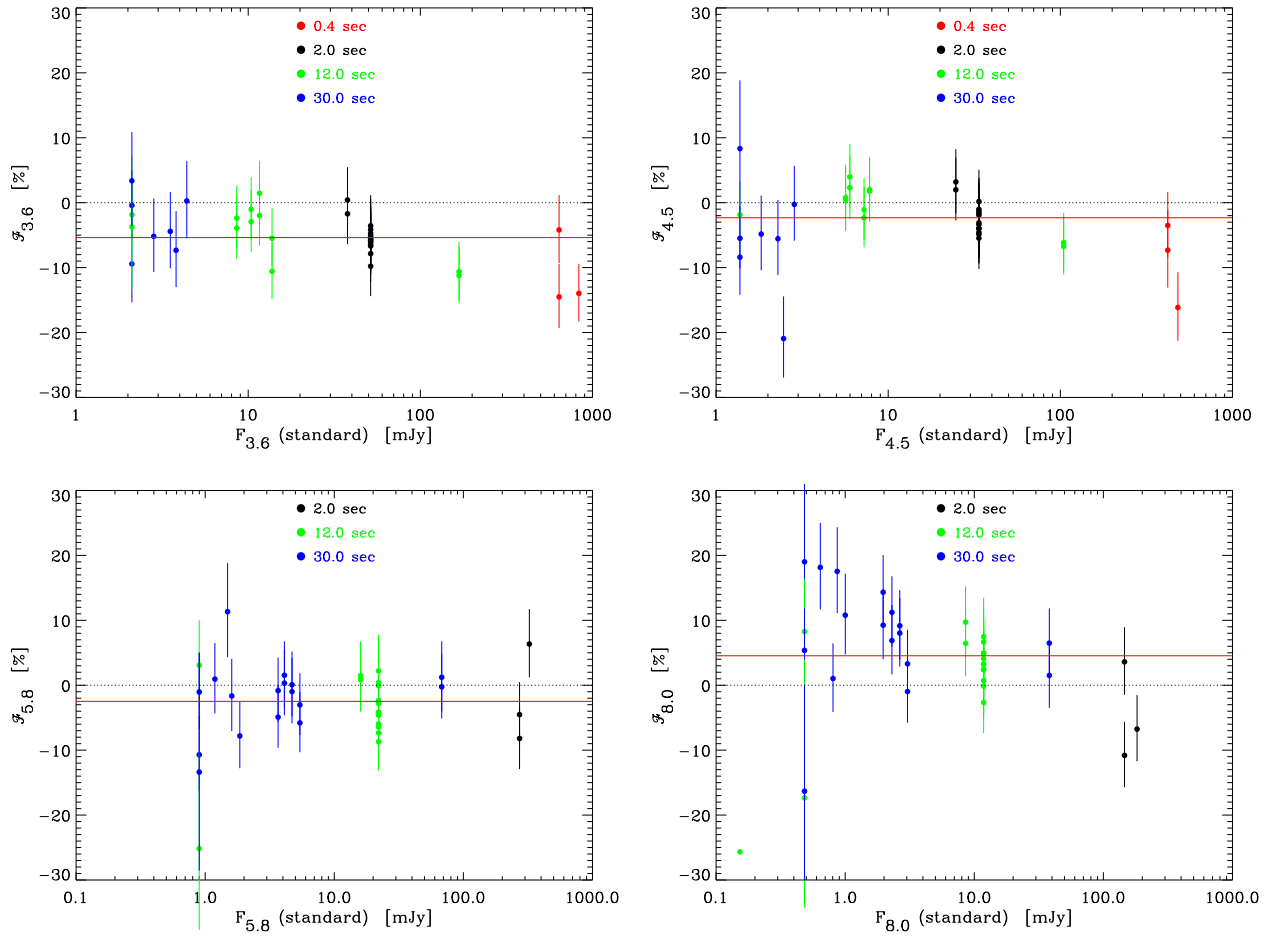


Fig. 27.— Comparison of c2d IRAC photometry of standard stars with their standard magnitudes. The relative offsets between our observed photometry and standard photometry are plotted as a function of standard fluxes for each IRAC band. The error bars represent the effective uncertainty in these offsets, computed by adding in quadrature the observed flux uncertainties (scaled-up c2dphot flux uncertainties; see §3.5.1) to the uncertainties in the standard fluxes. The dotted lines at $\mathcal{F}_\lambda = 0$ correspond to perfect agreement of our photometry with the accepted fluxes. The red solid lines represent the fitted offsets. The color of the symbols correspond to the exposure times of the images, helpful in confirming that none of the observed fluxes are expected to be affected by saturation.

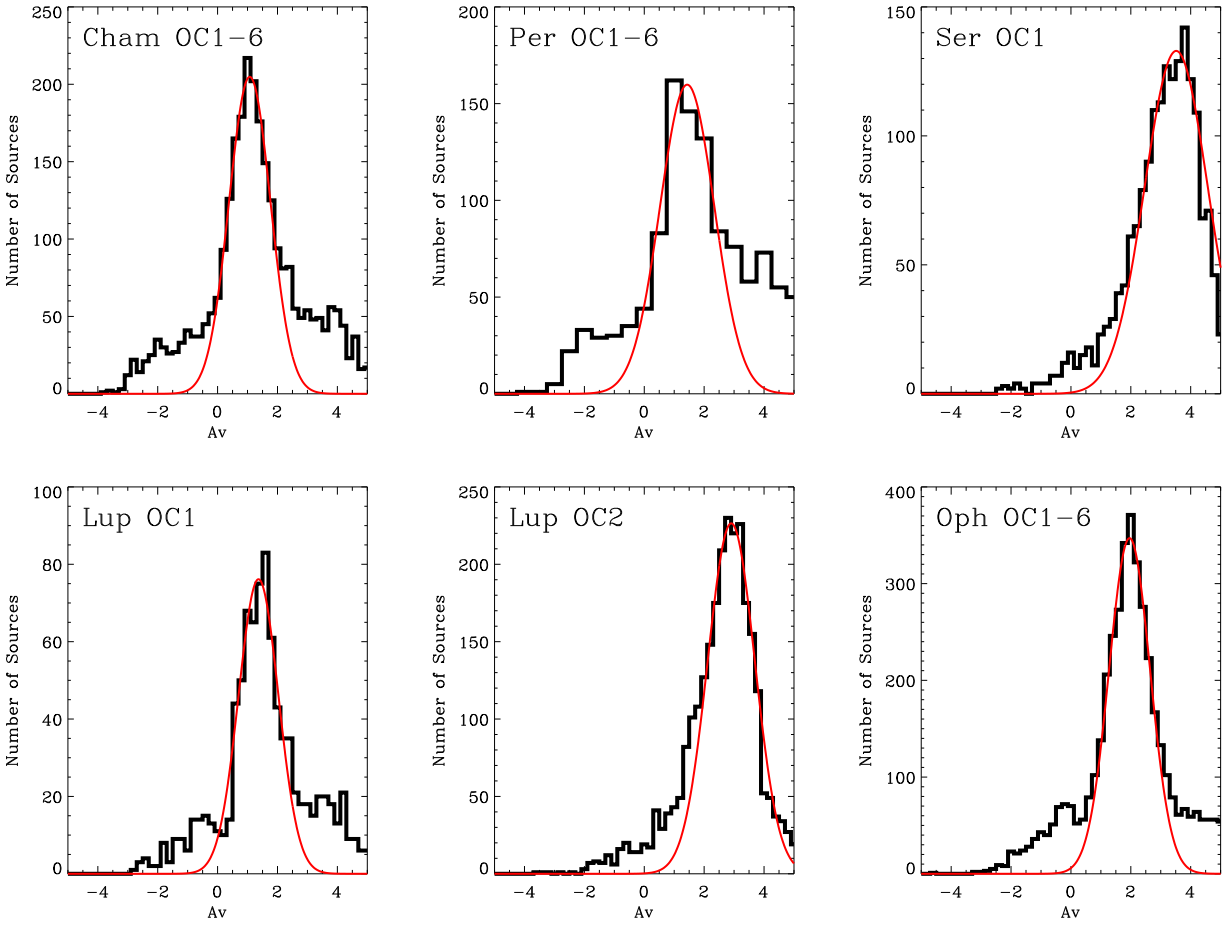


Fig. 28.— Distribution of fitted line-of-sight extinctions for stars in the different off-cloud fields. The observed distributions are shown by the histograms, while the Gaussian fits used to estimate the mode values are shown by the thin red curves.

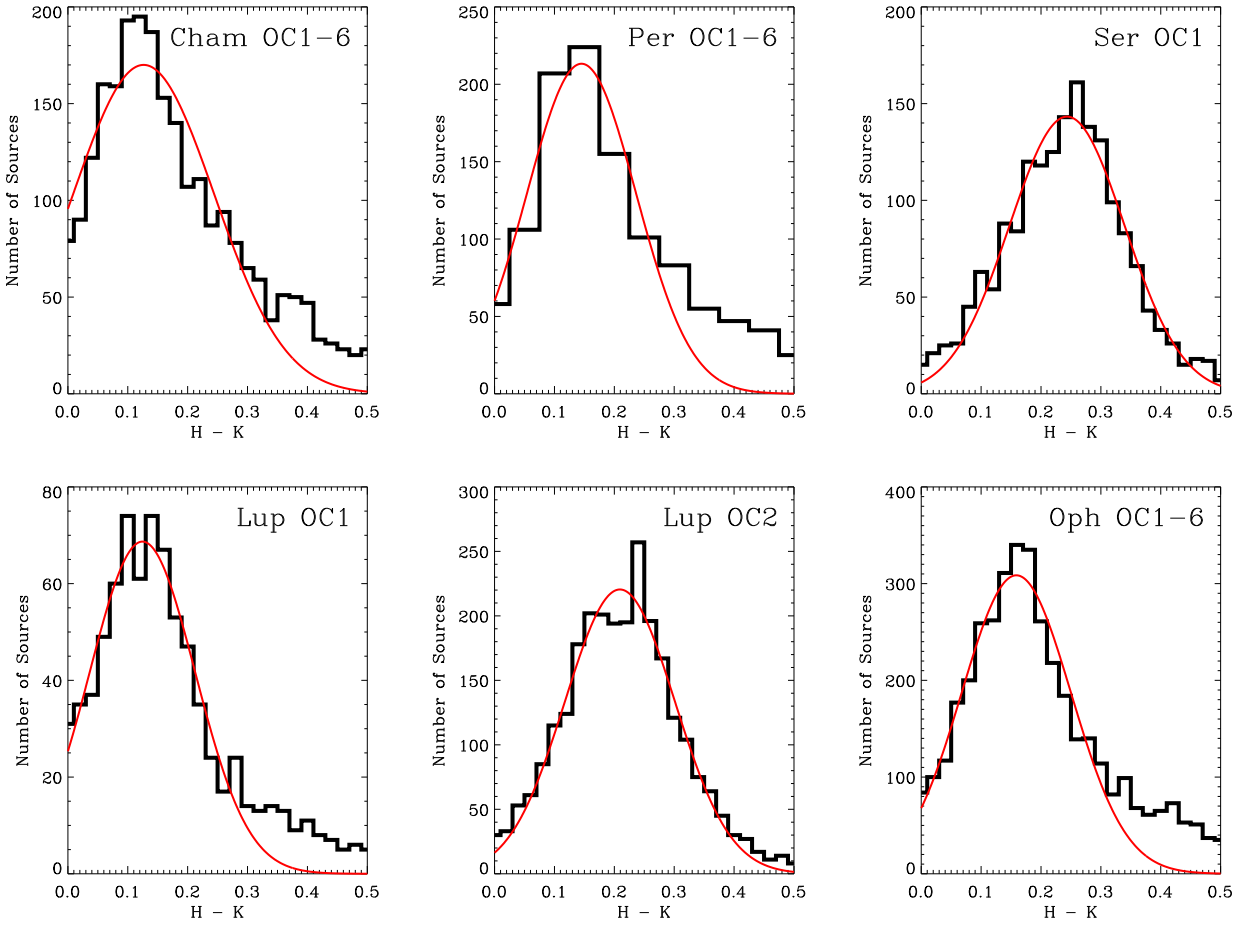


Fig. 29.— Distribution of H−K colors for stars in the different off-cloud fields. The observed distributions are shown by the histograms, while the Gaussian fits used to estimate the mode values are shown by the thin red curves.

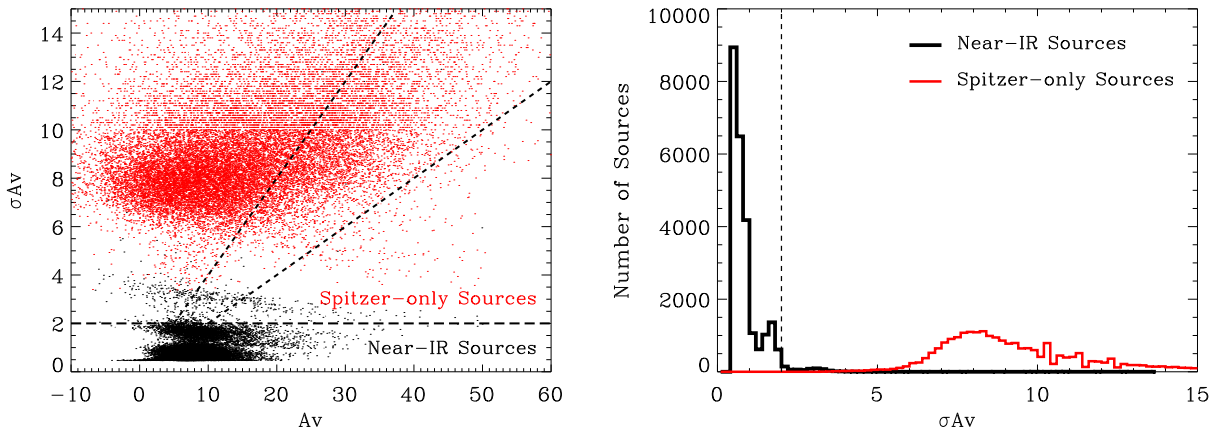


Fig. 30.— Comparison of uncertainty in extinction for near-infrared stars and Spitzer-only stars. [Left] For all sources classified as a star in Serpens, the uncertainty in the fitted line-of-sight extinction is plotted as a function of this line-of-sight extinction. Black points represent stars with at least one 2MASS near-infrared detection, while red points represent stars with detections only at the Spitzer bands. Nearly all stars with uncertainties of $\sigma_{A_V} \leq 2$ are those with 2MASS detections, while most stars with greater uncertainties are those with only Spitzer detections. Two different selection criteria for Spitzer-only stars are shown by the dashed lines. Spitzer-only stars with $(\sigma_{A_V}/A_V)_{crit} \leq 0.2$ are those above the horizontal dashed line and below the rightmost inclined dashed line, while those with $(\sigma_{A_V}/A_V)_{crit} \leq 0.4$ are above the horizontal dashed line and below the leftmost inclined dashed line. [Right] The distributions in line-of-sight extinction uncertainty for near-infrared stars and Spitzer-only stars are shown by the black and red histograms, respectively. The dashed line at $\sigma_{A_V} = 2$ illustrates the boundary: near-infrared stars dominate the sources found to the left, while Spitzer-only sources dominate the sources found to the right.

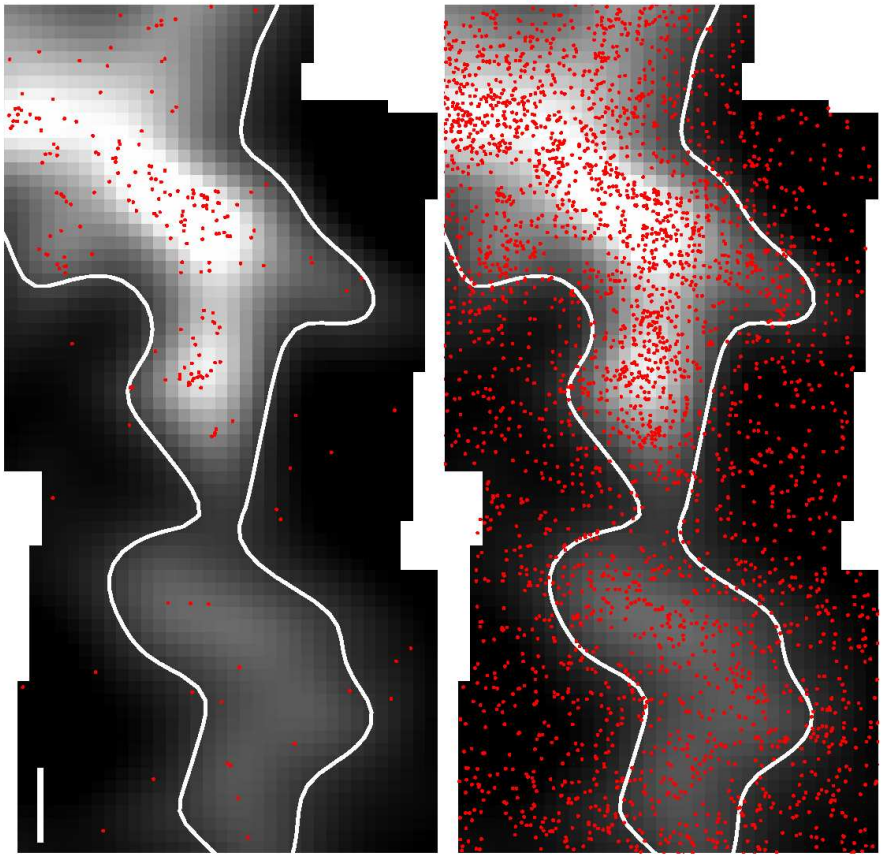

Fig. 31.— The distribution of Spitzer-only stars, represented by red points, with line-of-sight extinction uncertainties of $\sigma_{A_V}/A_V \leq 0.2$ [left] and $\sigma_{A_V}/A_V \leq 0.4$ [right], overlayed on the preliminary extinction map for part of the Serpens region imaged by *c2d*. The extinction map was constructed from well constrained line-of-sight extinctions toward near-infrared stars and a 300″ Gaussian beam. The greyscale is stretched linearly from $A_{V,map} = 5$ (black) to $A_{V,map} = 15$ (white).The $A_{V,map} = 7$ contour is shown. The white bar in the lower right of the left panel represents 5′.

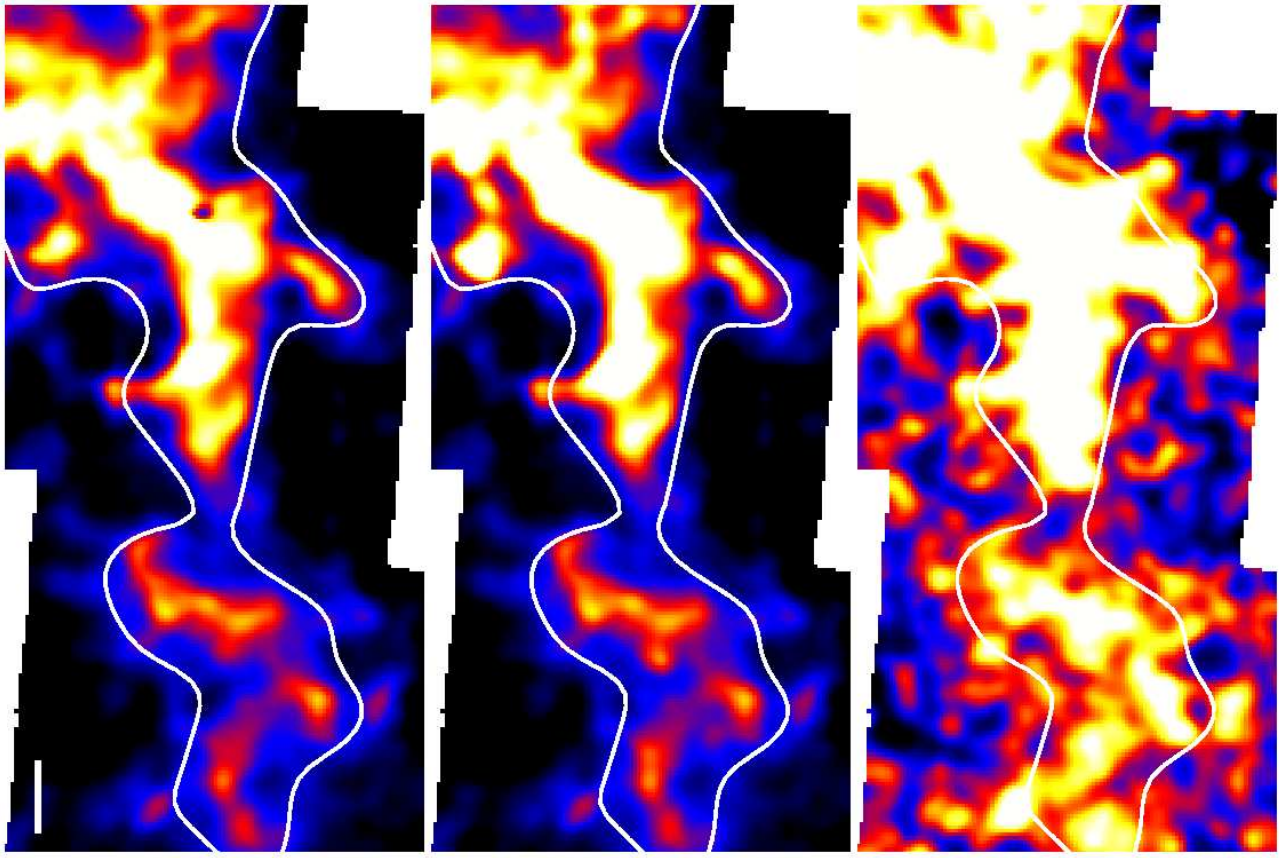

Fig. 32.— Extinction maps, scaled from $A_V = 5$ (black) to $A_V = 15$ (white), for the same portion of Serpens shown in Figure 31, except that these maps were constructed with a 90″ beam and varying criteria for including Spitzer-only sources to illustrate the effect of these sources on the maps. [Left] The preliminary extinction map, constructed with only near-infrared sources, is shown with the $A_{V,beam} = 7$ contour from the map constructed with the 300″ beam (relevant for the criteria that we chose for including Spitzer-only sources, as discussed later). This contour is similar to the $A_{V,beam} = 7$ contour from the 90″ map. The white bar in the lower right of the panel represents 5′. [Middle] The map constructed with near-infrared sources as well as Spitzer-only sources with well constrained extinctions ($\sigma_{A_V}/A_V \leq 0.2$) and positioned within the $A_{V,beam} = 7$ contour shown. These criteria match those that we used to construct the delivered maps. [Right] The map constructed with near-infrared sources as well as Spitzer-only sources with weakly constrained extinctions ($\sigma_{A_V}/A_V \leq 0.4$). In this map, it is evident that the overall extinction level increases, but many more structures, most of which are presumably artificial, appear in the low and high extinction regions compared to the previous two maps shown. In particular, the low extinction regions ($A_{V,beam} < 7$) are well probed by near-infrared sources, but relatively isolated Spitzer-only sources are seen to produce small artificial clumps (most of these clumps would not appear in the map in the middle panel even if the $A_{V,beam} > 7$ criteria were relaxed).

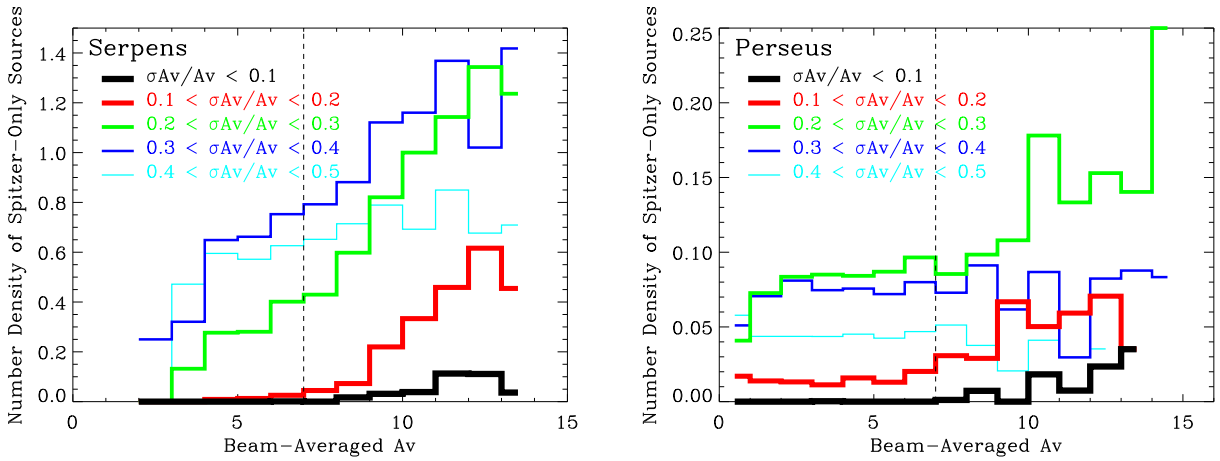


Fig. 33.— The number density of Spitzer-only sources in Serpens (left) and Perseus (right) as a function of the (300″) beam-averaged extinction, for populations with increasingly less constrained line-of-sight extinctions.

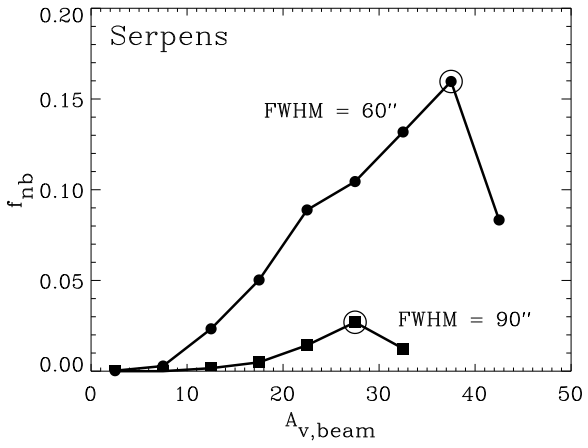


Fig. 34.— The fraction of pixels with undersampled beams, as defined in §3.7.2, as a function of $A_{V,beam}$ for extinction maps constructed with beams of FWHM of 60″ (filled circles) and 90″ (filled squares). In each case, the maximum fraction is explicitly identified by an open circle.

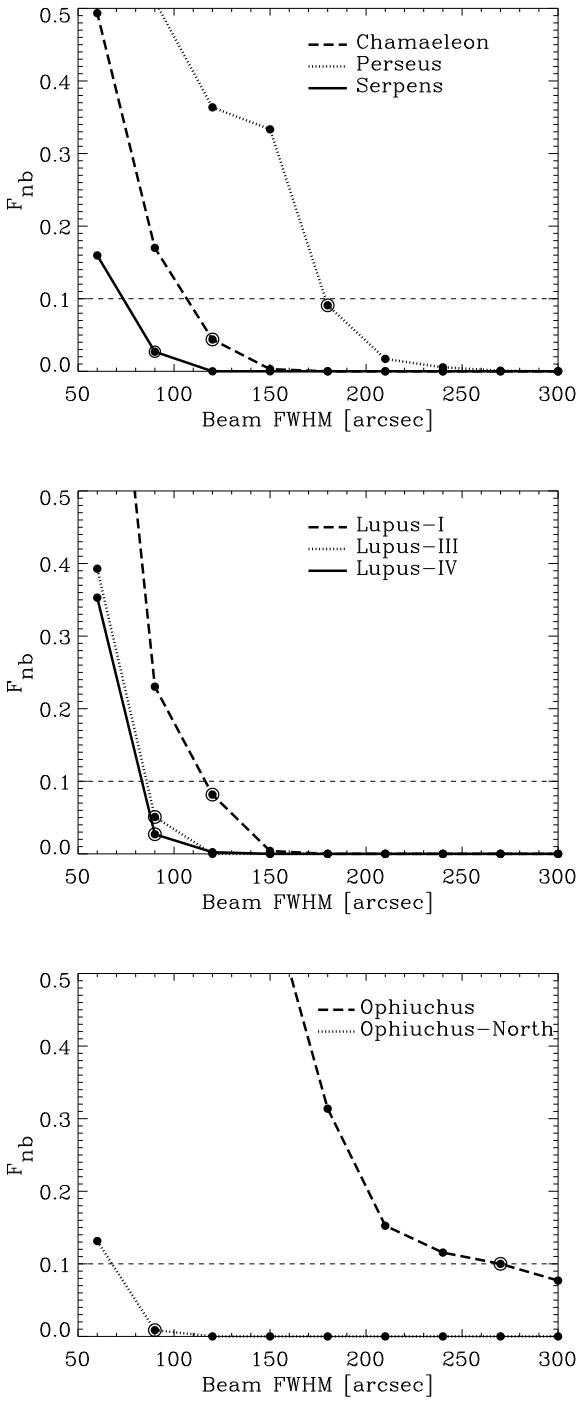


Fig. 35.— The maximum fraction of pixels with undersampled beams as a function of the beam FWHM for extinction maps of the clouds observed by c2d. Only those maps with a maximum fraction less than 0.1, shown by the horizontal dashed line, were delivered. This criteria effectively determined the maximum resolution of the map for each cloud, identified by an open circle.

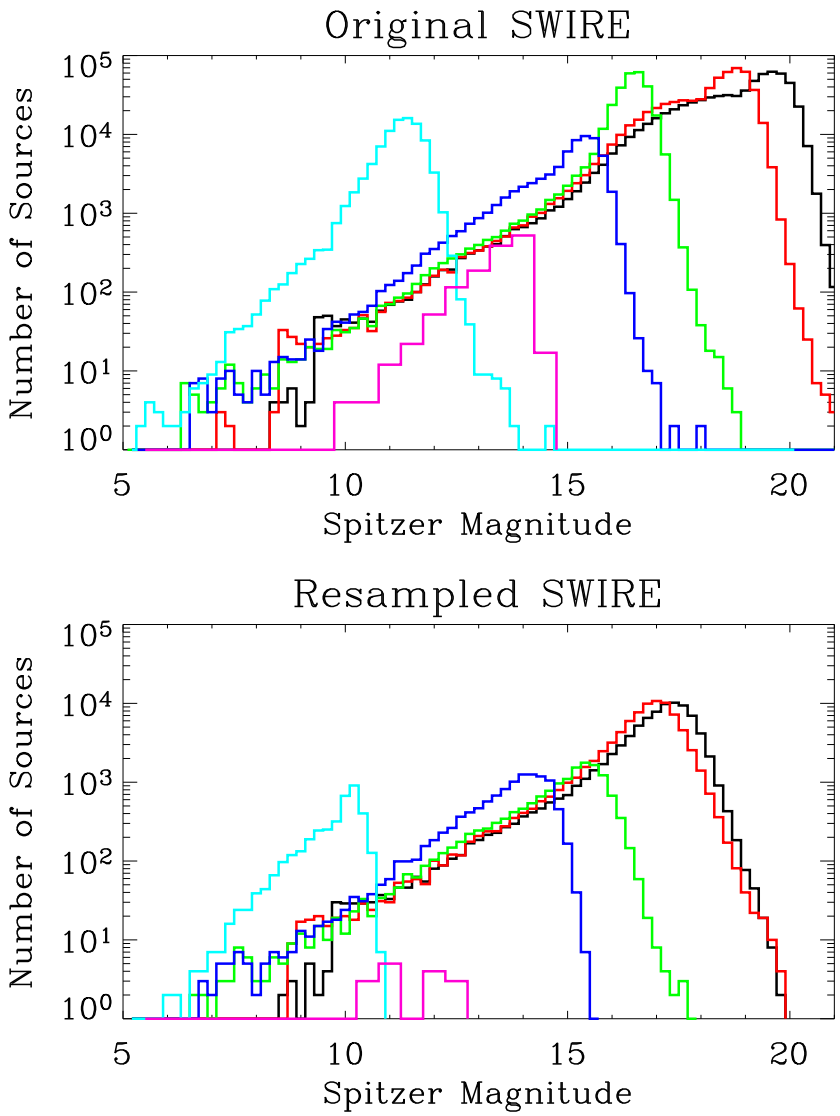


Fig. 36.— [Top] Luminosity functions, plotted in a similar way as those in Figures 21 and 22, for the original (before resampling) SWIRE catalog of sources. Comparison of the maxima of these distributions with those in Figures 21 and 22 demonstrate that the SWIRE Spitzer observations were somewhat deeper than our Serpens observations. Recall that the luminosity function for 70$\mu$m has been shifted by +10 mag toward fainter magnitudes in order to plot it on the same figure as the others. [Bottom] Same as top panel, except for a resampled SWIRE catalog (specifically, "resampled-SWIRE-SER_v1-FULL.tbl") constructed to simulate the effects of Serpens-like extinction profile and c2d sensitivities.

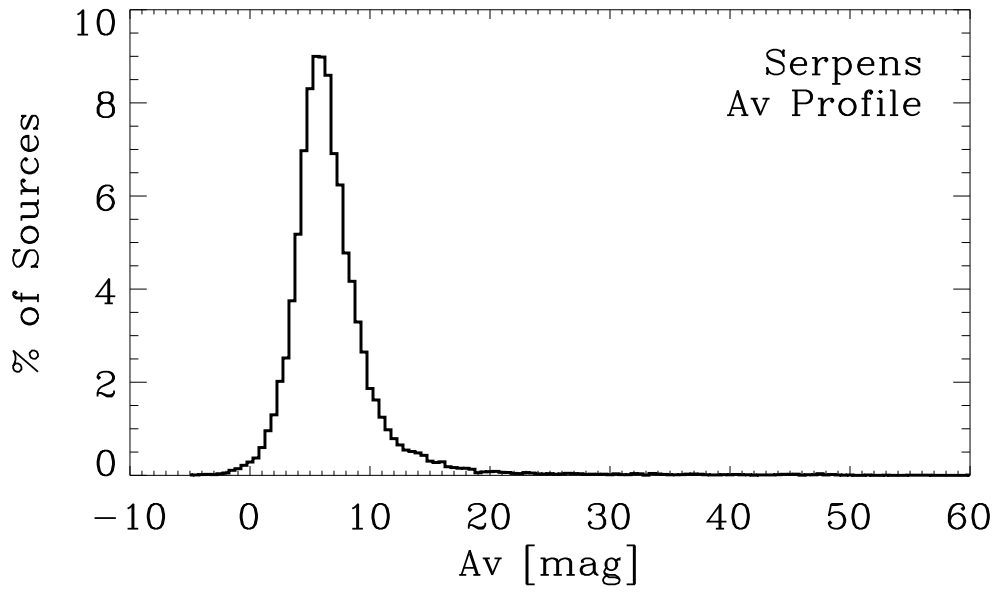


Fig. 37.— The profile of reliable line-of-sight extinctions (after accounting for the extinction offset; see §3.7.1) for stars used to construct the delivered Serpens extinction map in the Serpens field is shown. This profile represents the distribution of extinctions applied to the original SWIRE sources in order to construct a resampled SWIRE catalog.

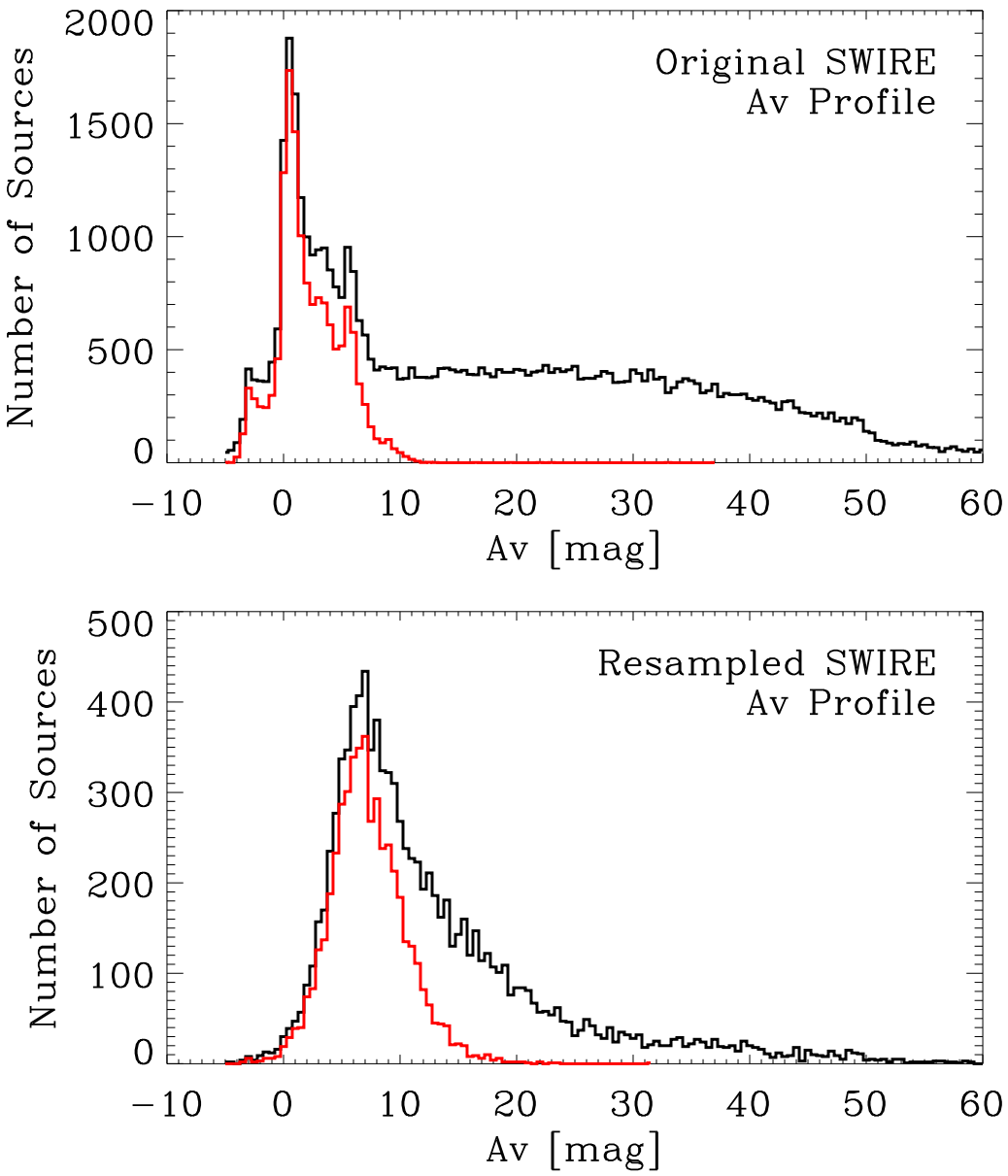


Fig. 38.— Extinction profiles of the fitted line-of-sight extinctions in the SWIRE ELAIS N1 field. [Top] The black histogram shows the profile for all sources classified as stars (see §2.5.2) in the original catalog, prior to simulating the effects of Serpens-like extinction and sensitivities of c2d observations. This field is expected to be free of significant extinction, and the extended profile toward greater extinctions represent the discrepant extinction measures resulting from fitting SEDs with only Spitzer detections (see §3.7.2). The red histogram shows the extinction profile for stars with at least one 2MASS near-IR detection, similar to the criteria for selecting reliable line-of-sight extinction measures in constructing our preliminary extinction maps. [Bottom] Same as the top panel, except for the resampled SWIRE catalog that accounts for the Serpens extinction profile and sensitivities of c2d observations.